Ph.D Thesis

Sarah Diane Lang

Cycle XXXIV

Kinetic aspects of major and trace element partitioning between olivine and melt during solidification of terrestrial basaltic materials

Thesis defence in March 2022

Department of Earth Sciences

Ph.D School "Vito Volterra" - Earth Sciences Curriculum

SSD
GEO/07 & GEO/08

Supervisor
Prof. Silvio Mollo (Sapienza)

Co-supervisor
Prof. Lydéric France (CRPG)

External reviewers
Dr. Alessio Pontesilli (INGV – Roma)
Dr. Federico Casetta (University of Vienna)

Laboratory Partners

CRPG – Nancy, France
(Centre de Recherches Pétrographiques et Géochimiques)

INGV – Roma, Italy
(Istituto di Geofisica e Vulcanologia)

"I am among those who think that science has great beauty. A scientist in his laboratory is not only a technician, he is also a child confronting natural phenomena which impress him like a fairy tale."

- *Marie Curie*

Acknowledgments

First of all, I wish to thank Alessio Pontesilli and Federico Casetta for the work done as reviewers of my thesis.

I wish to thank my supervisors, Silvio Mollo (Sapienza - University of Rome) and Lydéric France (CRPG - Nancy) for their guidance and advices through my doctoral studies. Although this thesis has been achieved to a large extend in social distancing and then under strong restrictive rules, I always felt supported. I can only imagine how difficult it can be to follow a student under such circumstances, but I never felt aside, a thousand of thanks for that. I want to thank in particular Silvio for his feedback, his availability, his patience and especially his unfailing positivity all along my thesis. Thank you for the time you dedicated correcting my papers with me, I really learned a lot from you.

I would like to thank Manuela Nazzari (INGV - Rome) for her assistance with the scanning electron microscope and the electron microprobe. Thanks to Andrey Gurenko (CRPG - Nancy) for the time he spent with me doing test and analyses with the SIMS. A big thanks to Jean-Luc Devidal (LMV – Clermont-Ferrand), through your help I obtained the laser analyses, and you were always available to reply to my questions.

I wish to thank the INGV to have hosting me, especially the HP-HT laboratory and its head Piergiorgio Scarlato. Thank you to Flavio and Alessio to have teaching me how to use the experimental apparatus in INGV. Thank you also to the CRPG to have hosting me for several months.

A big thank you to my colleagues and friends Stefano, Chris, and Giacomo for the wonderful time in but also outside the lab. Waking up the morning to work with you was always a pure pleasure. Because of your presence, the lab was always full of good vibe, laughs, and music (not always the best selection though!). I also would like to thank Fanny, my French colleague. And thank you to my colleagues of Sapienza.

I wish to thank “Chou”, without you this thesis would not exist at all. But more importantly, you are my greatest supports and you always believe in me when I cannot. Every time that I am feeling down, you are present for me and you find the perfect words to cheer me up and to motivate me. There are no words strong enough, but I hope you know how much gratitude I have for you.

Thank you to Lisa, with who I am sharing everything, good and bad moments of my life since we met the first day at the university, eight years ago. We grew together and you were the first person to encourage me to go ahead with the thesis. Today we are both finishing our thesis, and we can be proud of us. Merci de tout mon cœur ma Lisa.

I would like to take this opportunity to thank my parents, and my sister Camille. You were the first persons to believe in me. You always supported my choices and I hope to make you feel proud. Thank you also to my grandparents, my uncle and aunt, and my cousins. For them I will switch to French : *Maman et papa, je n'ai pas les mots pour vous remercier d'avoir toujours cru en moi, d'avoir supporté chacune de mes décisions et de m'avoir laisser étudier les* « cailloux ». *Si aujourd'hui j'ai eu la possibilité de faire cette thèse c'est grâce à vous et j'espère de tout cœur vous rendre fière. Ma petite Camille, merci pour tout le soutient dont tu as fait preuve. Je sais que je suis sensé faire mes remerciements ici, mais je voulais en profiter pour te dire à quel point moi je suis fière de toi. Merci aussi à ma mamie et mon papy, à mon parrain et ma marraine, et à tous mes cousins !*

To conclude, thank you to all the persons that I could have forget, I hope you will forgive me.

Thanks to all of you,

Sarah

Table of contents - General

Abbreviations and symbols 9

Abstract of the thesis 11

Introduction and project presentation 12

First part: Background and methodology 15

Chapter 1: State of Art 16

1. Olivine crystallisation and morphology 18
2. Olivine structure 25
3. Partition coefficient 28

References – Chapter 1 34

Chapter 2: Experimental and analytical methods 43

1. Introduction 46
2. Starting material preparation 46
3. Experimental strategy 48
4. Sample preparation 50
5. Analytical techniques 51

References – Chapter 2 58

Second part: Results 61

Introduction 63

Chapter 3: Kinetic partitioning of major-minor cations between olivine and Hawaiian tholeiitic basalt under variable undercooling and cooling rate conditions 65

Abstract 69
1. Introduction 70
2. Methods 72
3. Results 75
4. Discussion 85
5. Concluding remarks 95

References – Chapter 3 100

Chapter 4: Partitioning of Ti, Al, P, and Cr between olivine and a tholeiitic basaltic melt: Insights on olivine zoning patterns and cation substitution reactions under cooling rate conditions 109

Abstract 113
1. Introduction 114
2. Experimental and analytical techniques 116
3. Results 118
4. Discussion 128
5. Conclusions 138

References – Chapter 4 144

Third part: General conclusions & perspectives 153

Abbreviations and symbols

Å	Ångstrom units (10-8 cm)
a_i	activity of the element or phase i
atm	atmosphere (pressure unit) 1 atm = 1.0133 bar
BL	boundary layer
BSE	back-scattered electron
CFSE	crystal field stabilization energy
C_i	concentration of the element i
CR	cooling rate
D_i	diffusion coefficient of i
δ	depletion factor
ΔH	enthalpy
ΔG	difference in Gibbs free energy
$-\Delta T$	degree of undercooling
EMPA	electron microprobe analysis
ε	enrichment factor
Fa	fayalite
Fe^T	iron total
FFM	far-field melt
Fo	forsterite
fO_2	oxygen fugacity
G	Gibbs free energy
h_i	Henry's law
IM	interface melt
Kd_i	partition coefficient of i
λ	activity coefficient
Λ	optical basicity
M	octahedral site
μ_i	chemical potential
NBO/T	non-bridging oxygen per tetrahedra
NF	network former
NM	network modifier
OIB	oceanic island basalt
OSPE	octahedral site preference energy (kJ)
P	pressure
QFM	quartz-fayalite-magnetite buffer
R	gas constant (8.3 J/mol/K)
r	radius
SEI	secondary electron image
SEM	scanning electron microscopy
T	temperature and tetrahedral site
V	volume
W	Margules mixing parameter
WDS	wavelenght dispersive spectroscopy
wt. %	percentage on a weight basis
X_i	molar fraction
Z	atomic number

Abstract of the thesis

Olivine is an important mineral phase in naturally cooled basaltic rocks. The morphology and composition of olivine are controlled by the cooling kinetics, and the mechanisms controlling the crystal growth directly impact the partitioning of elements. Cations partitioning between two phases may document on the crystallization conditions of rocks. Indeed, the major elements composing a mineral usually affect the chemical equilibrium of a system, while trace elements are sensitive to thermodynamic conditions and record the chemical reactions occurring in the system without modifying the bulk reactions. Therefore, major and trace elements partitioning between olivine and melt is greatly considered by petrologists investigating terrestrial rocks through the use of phases exchange reactions.

In this study I explore the partitioning of major and trace elements between olivine and basaltic melt under conditions encountered by magmas during natural solidification path, and the cation substitution and charge balance mechanisms controlling the cations entrance in the lattice site of olivine crystals. In this context, I have performed undercooling ($-\Delta T$) and cooling rate (CR) experiments under relatively reduced environment (QFM-2) and atmospheric conditions using a tholeiitic basalt from Hawaii. Experiments started from the same superliquidus temperature of 1250 °C and was cooled at the rates of 4, 20, and 60 °C/h to the final temperature of 1175 and 1125 °C ($-\Delta T$ = 35 and 85 °C, respectively).

The olivine textural results indicate equilibrium at $-\Delta T$ = 35 °C, whereas strong disequilibrium occur at $-\Delta T$ = 85 °C. It is verified by the determination of the Fe-Mg exchange between olivine and melt. Indeed, low $-\Delta T$ experiments show bulk chemical equilibrium, while local equilibrium occurs at higher $-\Delta T$. The forsterite content decreases as CR increases and a diffusive boundary layer develops in the melt next to the crystal interface. However, the principal cations (Mg, Fe, Mn, and Ca) enter the crystal lattice (M-site) at near-equilibrium, which is compatible with the establishment of a local equilibrium. Ti, Al, and P cations are incorporated in olivine lattice by substituting Si in the T-site. Ti incorporation is controlled by a homovalent substitution $[{}^{T}Si^{4+}] \leftrightarrow [{}^{T}Ti^{4+}]$, while heterovalent substitutions occur for Al and P, following $[{}^{M}Mg^{2+}, {}^{T}Si^{4+}] \leftrightarrow [{}^{M}Al^{3+}, {}^{T}Al^{3+}]$, and $[2\ {}^{T}Si^{4+}] \leftrightarrow [{}^{T}P^{5+}, {}^{T}Al^{3+}]$. Although Cr is an octahedrally coordinated cation, it shows the same behaviour as cations entering in the T-site. Indeed, Cr is incorporated in the olivine lattice by forming a coupled substitution with a tetrahedrally coordinated cation $[{}^{M}Mg^{2+}, {}^{T}Si^{4+}] \leftrightarrow [{}^{M}Cr^{3+}, {}^{T}Al^{3+}]$, in order to maintain the charge balance. To preserve the charge balance, disequilibrium incorporation of minor elements is governed by the same mechanisms that occur under equilibrium crystallization, which is consistent with interface local equilibrium.

Olivine is an important rock-forming mineral at magmatic conditions, which makes it one of the first species to crystallize in mafic igneous rocks along with pyroxene and plagioclase (Cressey and Howie, 2005). Olivine is considered as the most abundant constituent of the Earth's upper mantle, but also occurs in high-temperature metamorphic rocks, lunar basalts, and some meteorites. Most commonly, olivine is found in mafic igneous rocks, such as gabbro, and basalt but also in ultramafic rocks, as peridotites. Olivine is also common in the Moon and meteorites such as stony meteorites (chondrite and achondrite) and stony-iron meteorites (pallasite) coming mainly from the asteroid belt between Mars and Jupiter. The study of physical, chemical, and mechanical properties of olivine represents therefore an outstanding source of information about the origin, crystallization, and differentiation of the solidifying terrestrial and extra-terrestrial systems, allowing us to understand the physical state of the Earth's interior (Cordier et al., 2014), the origin of meteorites, and the history and processes on planetary bodies (Cressey and Howie, 2005).

The partitioning of major and trace elements between olivine and melt is taken in great consideration by petrologists investigating terrestrial rocks through the use of mineral-mineral or mineral-melt element exchange reactions. Indeed, major elements generally affect the thermodynamic environment (chemical equilibrium), while trace elements are sensitive to thermodynamic conditions and therefore, behave as passive tracers of chemical reactions without influencing the bulk reactions themselves (Mahan, 2021). The attainment of a full equilibrium state is not the rule in naturally solidifying environments. Rather, cooling kinetics influence the crystal growth and mineral assemblage, thereby determining the final rock texture (Hammer, 2006; Iezzi et al., 2011; Mollo et al., 2010; 2011). When the crystal growth mechanism shifts from interface-controlled to diffusion-controlled, the competition between growth rate and element diffusion rate in the melt will directly impact the partitioning of elements between olivine and melt. In an equilibrium system (interface-controlled growth), the partition coefficient corresponds to a "true" Kd_i (reaction constant). In contrast, in a disequilibrium system (diffusion-controlled growth), the partition coefficient corresponds to an "apparent" Kd_i and the chemistry of the advancing crystal surface reflects the composition of the interface melt (diffusive melt) rather than the far field melt unaffected by concentration gradients. Thus, by development of diffusion–controlled reactions, the partition coefficient Kd_i calculated at the crystal–melt interface may document the conditions in which the advancing crystal surface is in near local equilibrium with the adjacent melt. However, depending on the ability of chemical species to diffuse more or less rapidly in the melt phase, the difference between the "apparent" and "true" Kd_i can be smaller or larger (Mollo and Hammer, 2017). It has already been observed that olivine does not re-equilibrate with the melt over rapid cooling rate, such that incompatible elements are incorporated in the crystal lattice at non-equilibrium proportions. The development of local equilibrium interface reactions also supports the hypothesis that incorporation of trace elements into rapidly growing olivine is controlled by local charge–balanced configurations (Mollo et al., 2013b).

Keeping the above considerations in mind, I have based this project on experimental petrology and microchemical analyses. Two main questions guided this study: how does the undercooling and cooling rate affect the partitioning of major and trace elements between olivine and terrestrial basaltic liquids? And how do trace cations substitute in the olivine crystal lattice? To answer these questions, I performed cooling rate experiments at different degrees of undercooling and executed quantitative analyses on the resulting samples.

Chapter 1 is a literature review. First, it defines the degree of undercooling and cooling rate, and how these parameters affect the crystallization of olivine and its composition. It also reviews the different olivine morphologies obtained under (dis)equilibrium crystallization conditions. Second, it gives a general overview on the olivine structure and the occupancy of the atomic sites. The last part of this chapter presents the thermodynamic basis on elements partitioning and the parameters governing this partitioning.

Chapter 2 presents the synthesis of the starting material, details on the experimental procedures, and sample preparation for analyses. It also introduces the principles of the different experimental and analytical apparatus used in the context of this study.

Chapter 3 focuses on the partitioning of Fe, Mg, Ca, Mn, and Cr cations between olivine and melt from two experimental sets obtained under three cooling rates and two undercooling conditions.

Chapter 4 focuses on the kinetic partitioning of Ti, Al, P, and Cr cations to investigate the charge balance mechanisms and cation substitution reactions controlling the incorporation of these cations in the lattice site of rapidly growing olivine crystals.

This PhD thesis ends with a general conclusion, and the presentation of future perspectives.

First Part

Background and methodology

Chapter 1

State of art

Table of content - Chapter 1

1. Olivine crystallization and morphology 18
   - 1.1. Crystal nucleation theory 18
   - 1.2. Concept of undercooling 19
   - 1.3. Effect of undercooling and cooling rate on olivine texture and composition 20
   - 1.4. Description of olivine morphology 21
2. Olivine structure 25
   - 2.1. Temperature and pressure effects on M-O and Si-O bond distance 26
   - 2.2. Octahedral site occupancy 27
3. Partition coefficient 28
   - 3.1. Thermodynamic basis of element partitioning 29
   - 3.2. Parameters governing the partitioning of elements 30

References - Chapter 1 34

Chapter 1

State of art

“Chrysolite” was the earliest name given to an olivine group species in 1747 by Johan Gottschalk Wallerius. In 1789, the mineral was renamed “olivine” by Abraham Gottlieb Werner, because of the typical olive-green colour of its magnesian component. Olivine is the common name to call mineral with the general composition M_2SiO_4 (M define the cations entering in the octahedral site). The classical solid solution of olivine ranges from the forsterite end-member (magnesian olivine, Mg_2SiO_4) to the fayalite one (Fe-rich olivine, Fe_2SiO_4), but the olivine group also extends to the tephroite (Mn_2SiO_4), and larnite (Ca-olivine; Ca_2SiO_4) end-members and can incorporate in its composition some minor elements. Olivine is a common mineral phase in basaltic rocks from terrestrial and extra-terrestrial magmas, and its texture and chemical characteristics represent an outstanding source of information about the origin, crystallization, and differentiation of the solidifying system.

1. Olivine crystallization and morphology

1.1. Crystal nucleation theory

According to Bowen’s reaction series, olivine is the first mineral to crystallize from magmatic melt during its cooling history (in reduced environments, while spinel will crystalize first in oxidizing environments). With respect to the superliquidus state of magma, a certain amount of undercooling is always necessary to induce crystal nucleation and growth in natural and experimental sample (Mollo and Hammer, 2017). Crystallization begins when the liquids become significantly oversaturated in some species (White, 2020). In a liquid in which atoms are subject to thermal vibrations, atoms might approach each other to distances proportional to solid interatomic spacing, leading to the formation of solid-like cluster. However, this cluster will decay spontaneously as the temperature is over the melting point. At the liquidus temperature (T_{liq}), the Gibbs free energy of the liquid (G_l) and solid (G_S) phases are equal, implying thermodynamic equilibrium. When liquid temperature is below T_{liq} by a certain amount of undercooling, the Gibbs free energy of the solid decreases by ΔG (difference in Gibbs free energy). Thus, we expect a spontaneous growth of clusters leading to the formation of crystal. In other words, crystallization needs a negative ΔG (Herlach and Feuerbacher, 1986).

The interface between liquid and solid phase, described by an interface energy, occurs during the formation of a cluster, and must be considered in the free energy balance (Herlach and Feuerbacher, 1986). Indeed, since the interface energy is always positive, it acts as a barrier against crystallization. ΔG requires the formation of a spherical cluster of radius r, and ΔG reach a positive maximum value at a critical radius r^+ forming an activation barrier against crystallization. If the size of the cluster is below r^+, the surface contribution predominates, and the cluster will decay. On the other hand, if the size of the cluster is above r^+ (it is therefore called nucleus), it can lower its free energy by growing (Herlach and Feuerbacher, 1986). These authors enounced that the radius of a critical nucleus decreases continuously with undercooling. Therefore, according to this theoretical approach, an increasing degree of undercooling will favour crystallization.

1.2. Concept of undercooling

We must distinguish between the “nominal undercooling” (-ΔT; used in this study) and the “actual undercooling”. The nominal undercooling is defined as the difference between liquidus temperature ($T_{liquidus}$) and quench temperature (T_{quench}) by Kirkpatrick et al. (1981). The “actual degree of undercooling” is the difference between the actual temperature of a liquid or a liquid-crystal system and the temperature at which a phase saturates ($T_{liquidus}$) in the given liquid (Hammer, 2008). However, it is difficult to determine accurately, as during crystallization the liquid composition changes resulting in a change of the liquidus temperature (Faure et al., 2003). When the cooling rate is rapid, the growth is controlled by diffusion and the chemical composition of the liquid is affected by crystal growth only in a narrow melt zone around the crystal and the liquidus temperature do not change far from the crystal (Faure et al., 2003). Therefore, the “nominal undercooling” (defined as liquidus temperature minus quench temperature) determined by Kirkpatrick et al. (1981) can be a good approximation of the degree of undercooling in the case of my experiments.

1.3. Effect of undercooling and cooling rate on olivine texture and composition

The textural evolution and compositional change of minerals are not necessarily related to the attainment of equilibrium, but rather to the development of kinetic effects along the crystallization path of magma (Hammer, 2006, 2008; Iezzi et al., 2011; Del Gaudio et al., 2010; Mollo et al., 2010, 2011). Small degree of undercooling promotes interface-controlled crystal growth mechanisms where the diffusion of chemical elements in the melt prevails over the crystal growth rate. Minerals develop euhedral textures (Figure 1.1a), and generally, they do not present core-to-rim zonation, and the composition of the melt next to the crystal surface is homogeneous (Figure 1.1b; Mollo et Hammer, 2017). In contrast, large undercooling promotes diffusion-controlled crystal growth, where the crystal growth rate exceeds the diffusion rate. The crystal texture is anhedral, with a wide spectrum of disequilibrium features (Figure 1.1a). Crystals present internal zonation and compositional gradients develop in the melt next to the crystal surfaces (Figure 1.1b; Mollo et Hammer, 2017). This compositional gradient in the melt, also called boundary layer (BL), is affected by accumulation of incompatible elements (rejected by the crystal) and/or depletion in compatible elements (preferentially incorporated in the crystal lattice) in the melt next to the crystal interface. BL results from the slow diffusion of cations away from the growing crystal surface or by the supply of fresh cations from the far field melt towards the crystal surface to maintain a uniform concentration in the melt (e.g., Tiller et al., 1953; Smith et al., 1955; Lasaga, 1982; Watson and Müller, 2009, 2015; Baziotis et al., 2017). In other words, the extent of BL is dependent of the capacity of the element to diffuse in the melt. However, the diffusion rate is different for each element. For the same cooling conditions (same CR and -ΔT), some elements might present large BL, while others exhibit very short to absent BL. This means that BL for diffusion-controlled growth conditions might potentially not be located at the same place for each element. Thus, development of a BL in the melt could be uncorrelated with the mechanism by which the crystal-melt interface advances over time. Fast-diffusing elements could be in equilibrium between the fast-growing crystal and the FFM, whereas the slow-diffusing ones could not.

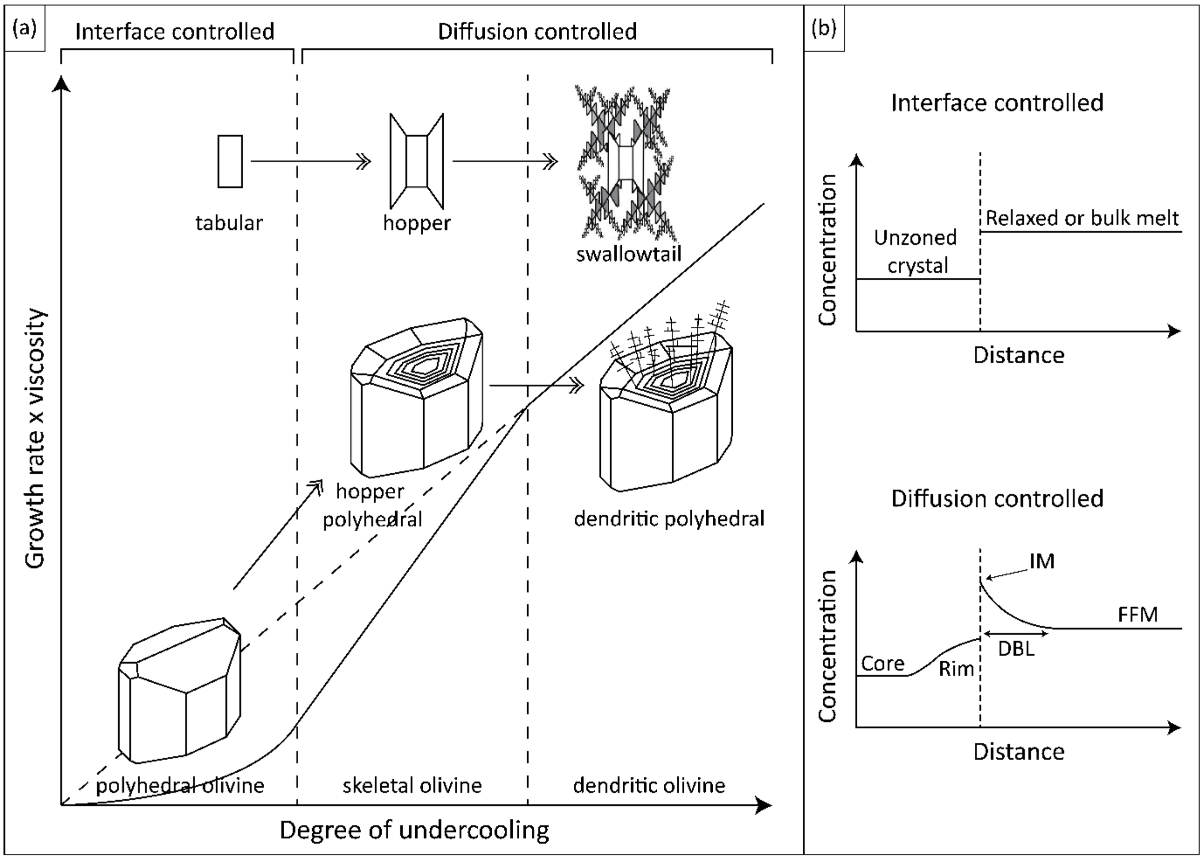
(a)
Interface controlled
Diffusion controlled
tabular
hopper
swallowtail
hopper polyhedral
dendritic polyhedral
Growth rate x viscosity
polyhedral olivine
skeletal olivine
dendritic olivine
Degree of undercooling
(b)
Interface controlled
Concentration
Unzoned crystal
Relaxed or bulk melt
Distance
Diffusion controlled
Concentration
IM
FFM
DBL
Core
Rim
Distance

Figure 1.1. *(a) Diagram showing the evolution of olivine morphology as a function of growth mechanisms governed by the degree of undercooling. Redrawn and modified after Faure et al. (2007). (b) Diagram showing the effect of interface- and diffusion-controlled crystal growth leading to equilibrium crystallization surrounded by homogeneous melt and disequilibrium crystallization due to melt compositional gradient, respectively. Redrawn and modified after Mollo and Hammer (2017).*

1.4. Description of olivine morphology

Ten types of olivine morphologies have been defined by Donaldson (1976) as a function of cooling rate and degree of undercooling: polyhedral olivine, granular olivine, hopper olivine (or "porphyritic olivine" of Donaldson, 1974), chain olivine, lattice olivine, plate olivine, branching olivine, radiate olivine, feather olivine, and swallowtail olivine. A model for describing olivine morphological changes as function of undercooling and cooling rate has been proposed by Faure et al. (2003). In their numerous experiments (with undercooling and cooling rate ranging between 20-356 °C and 1-1890 °C/h, respectively), the authors distinguished five different types of morphologies: polyhedral, tabular, skeletal, dendritic, and feather shape (Figure 1.2).

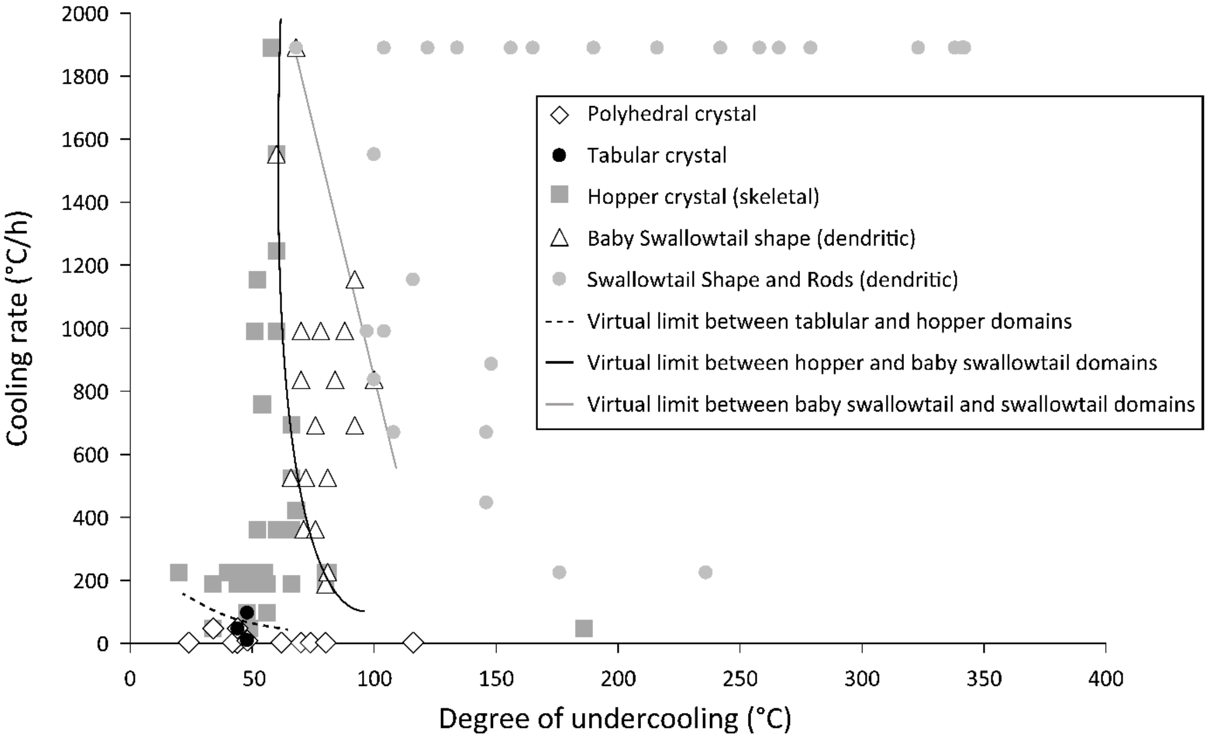

Figure 1.2. *Morphological variation of olivine as a function of cooling rate and undercooling. Redrawn and modified after Faure et al. (2003).*

Euhedral crystal shape category (equilibrium crystal shape) includes polyhedral texture (Figure 1.3a) that always displays well-defined faces, and tabular morphology (Figure 1.3b). This latter presents a rectangle shape when the crystal is oriented under [010] and needle-like shape for section normal to [010]. This morphology is less common than others, and always associated with polyhedral or hopper crystals.

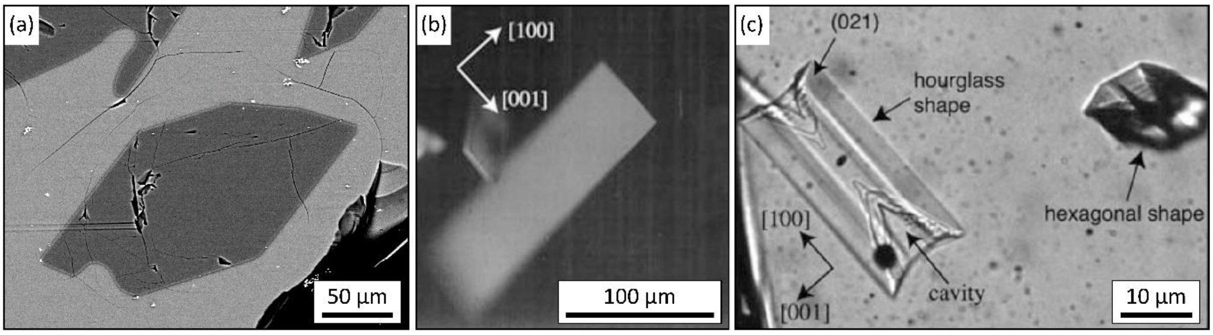

Figure 1.3. *Photomicrographs of olivine displaying the different morphologies described in the text. (a) polyhedral morphology (from Shea et al., 2019); (b) tabular morphology (modified after Faure et al., 2003); (c) hopper/skeletal morphology (modified after Faure et al., 2003).*

Anhedral crystal shape category (disequilibrium crystal shape) gathers the remaining textures (Faure et al., 2003). Skeletal or hopper morphologies (Figure 1.3c) present two different shapes according to the axis of observation. Olivine can have hexagonal ([100] direction) or hourglass shape ([010] direction). Hopper morphology is characterized by crystals that at the top terminate with a large cavity filled with glass (Donaldson, 1976; Faure et al., 2003). Swallowtail shape (Figure 1.4) corresponds to a plane view (section parallel to [010]) of a dendritic crystal (Donaldson, 1976; Faure et al., 2003). Two evolutive stages can be distinguished: baby swallowtail (Figure 1.4b) and swallowtail shapes (Figure 1.4c), corresponding at the beginning of the dendritic growth (initial degree of the dendritic growth) and a well-developed morphology, respectively (Faure et al., 2003). These shapes correspond to hopper crystals which have dendrite overgrowths (Figure 1.4a). They are displayed on the upper part of the cavity of the parent hopper crystal and never start to grow from the bottom of the hopper cavity. Dendrites are composed of several sets of fibres corresponding to several generations of crystallites (first, the four primary branches form the frame of the dendrite; then, a second generation of fibre develop on the primary ones; etc.; Figure 1.4d). Swallowtail crystals differ from baby swallowtail crystals by the occurrence of abundant dendritic growth (Faure et al., 2003).

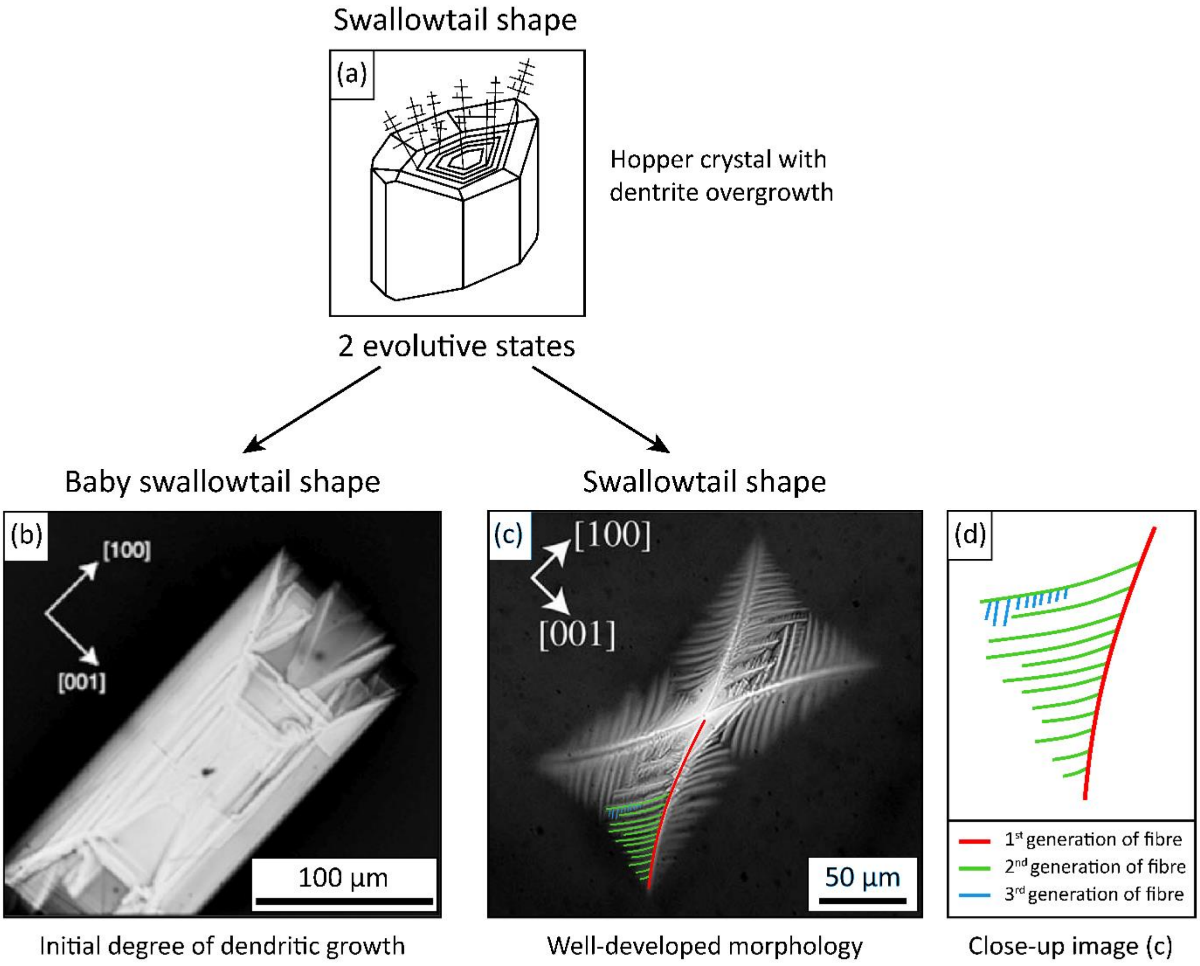
Swallowtail shape
(a)
Hopper crystal with dentrite overgrowth
2 evolutive states
Baby swallowtail shape
Swallowtail shape
(b)
[100]
[001]
100 µm
(c)
[100]
[001]
50 µm
(d)
1st generation of fibre
2nd generation of fibre
3rd generation of fibre

Initial degree of dendritic growth

Well-developed morphology

Close-up image (c)

Figure 1.4. *Photomicrographs of olivine displaying the different morphologies described in the text. (a) Scheme of a hopper crystal with dendritic overgrowth; (b) dendritic shape – baby swallowtail morphology (modified after Faure et al., 2003); (c) dendritic shape – swallowtail morphology (modified after Faure et al., 2007); (d) schematic close-up of one of the four main branches (c).*

The rod morphology (Figure 1.5a) corresponds to a cross section of the dendrite and is composed either of a single rod or a group of parallel rods belonging to the same structural entity (Faure et al., 2003). These elongated crystals are equivalent to the chain olivine described in Donaldson (1976). The internal part of the rods consists of complex microstructure composed of units having a ‘‘flattened Maltese cross’’ or ‘‘ornamental lantern form’’ (Bryan, 1972), also called H-shape by Donaldson (1976). Feather olivine (Figure 1.5b), named by Donaldson (1976), consists of very fine fibres growing on the outermost part of the swallowtail crystals and rods. The sample studied by Faure et al. (2003) show that feather olivine is always associated with dendritic pyroxene.

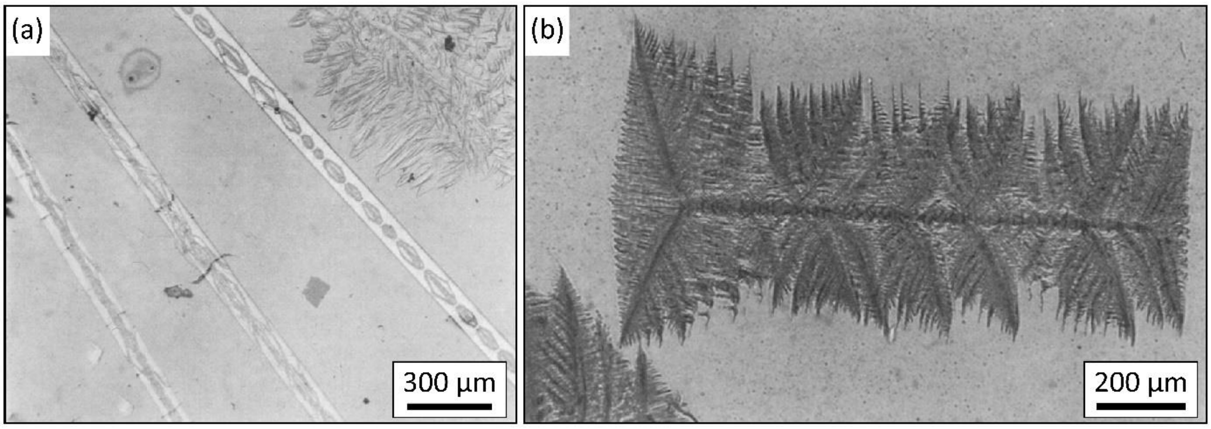

Figure 1.5. *Photomicrographs of olivine displaying the different morphologies described in the text. (a) dendritic shape – rods/ chains morphology (modified after Donaldson, 1976); (b) dendritic shape – feather morphology (modified after Donaldson, 1976).*

To summarize, olivine morphology evolves with cooling rate but mainly with the degree of undercooling from tablets, to skeletal, to dendritic texture. The other shapes described in the literature can be considered as specific crystal section of these three main shapes.

2. Olivine structure

Olivine structure was determined by Bragg and Brown (1926) using a crystal with composition $Fo_{90}Fa_{10}$. This mineral has orthorhombic symmetry with structure of independent SiO_4 tetrahedra linked by divalent cations each of which has six nearest oxygen neighbours. The oxygen-atoms lie in sheets in a quasi-close packed arrangement. The atomic sites located between the oxygen sheets are in either tetrahedral (T-) or octahedral (M-) coordinations (Deer et al., 1997; Figure 1.6). One eighth of the tetrahedral site is occupied by Si atoms, and half of the available octahedral site by M-atoms (Mg and/or Fe). Each oxygen is bonded to one silicon and three M atoms (Deer et al., 1997). The M-atoms are located on half at centers of symmetry (M1-site) and half on mirror planes (M2-site) (Figure 1.6).

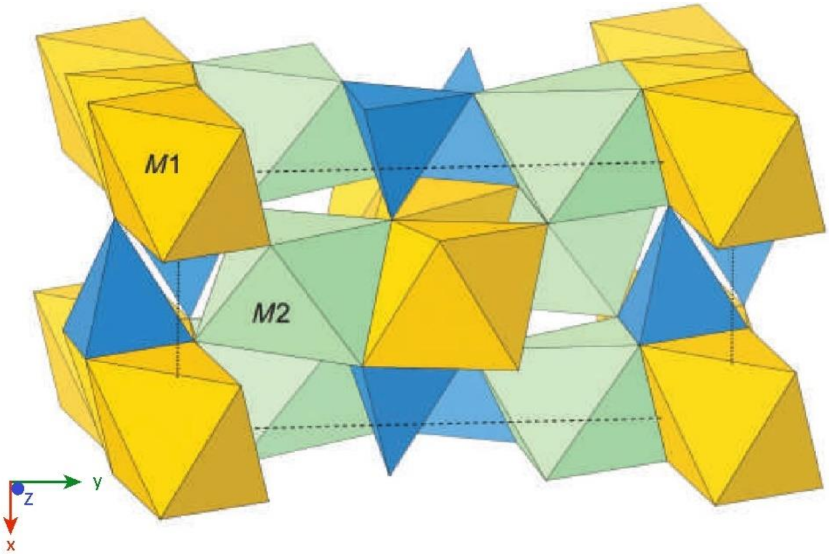

Figure 1.6. *Polyhedric model of olivine structure. The top of polyhedral corresponds to the oxygens. In the center of the polyhedra, there is Si (blue), M1-cation (yellow), and M2-cation (green). Image after Deer et al. (2013).*

2.1. Temperature and pressure effect on M-O and Si-O bond distance

The structure of olivine shows deviations from ideal hexagonal close-packing and both octahedra and tetrahedra diverge from their regular forms (Deer et al., 1997). Birle et al. (1968) determined three distinct Si-O bond lengths. For forsterite, Si-O(1) apical = 1.614 Å, Si-O(2) basal = 1.654 Å, and SiO(3,3') = 1.635 Å. The average M-O distance of M1-site is smaller than M2-site. For forsterite, M1-O = 2.103 Å and M2-O = 2.135 Å. However, the M-O distance is not constant, increasing linearly for both M1- and M2-O, as the fayalite content increases (Deer et al., 1997). Brown and Prewitt (1973), Smyth and Hazen (1973), and Smyth (1975) have studied the effect of temperature on structural variation in Mg-Fe olivine. Brown and Prewitt (1973) used two different olivine series, a lunar olivine, and a metamorphic olivine, Smyth and Hazen (1973) considered synthetic forsterite and metamorphic hortonolite (intermediate member of the Fa-Fo series), and Smyth (1975) studied synthetic fayalite. Their comparative results show that the M1- and M2-O bond lengths increase with increasing temperature. Additionally, the three studies indicate that the Si-O distance does not change with temperature. The volume and volume distortion of the M1, M2 an T polyhedra were calculated by Pamato et al. (2019) for different pressure, using the IVTON software (Balic-Zunic and Vickoviv, 1996) as $[V_i - V_p]/V_i$, where V_i is the volume of the ideal polyhedron and V_p the volume of the coordination polyhedron. In general, data from Pamato et al. (2019) show that M1 polyhedron in olivine is smaller and more distorted than the M2 one. As an example, at 1 atm, M1, M2, and T polyhedra have volumes of 11.82, 12.43, and 2.21 Å^3, respectively, and volume distortions of 0.0382, 0.0229, and 0.0127 Å^3, respectively.

2.2. Octahedral site occupancy

Ordering phenomena in the crystal structure of minerals are related to both physical properties of crystals and thermodynamic properties of mineral assemblage (Morozov et al. 2005). In olivine, divalent cation resides in two non-equivalent octahedral sites, M1 and M2. The M1-site is generally smaller and more distorted than the M2-site (Deer et al. 1997; Pamato et al., 2019). The partitioning of cations between both M1- and M2-site is the result of the difference in the crystallographic environment of the M-site as well as the difference in the chemical behaviour of Fe and Mg (Deer et al. 1997).

The early structural investigations (Sahama and Torgeson, 1949), as well as later structural studies (Hanke, 1965; Birle et al., 1968) have considered the distribution of Mg^{2+} and Fe^{2+} as essentially disordered. However, direct site refinement technique using X-ray intensity data (Nafziger and Muan, 1967; Katayama and Katsura, 1968), and later Mössbauer studies (Bush et al., 1970; Virgo and Hafner, 1972; Shinno et al., 1974) have shown that the larger Fe^{2+} cation (rFe^{2+} = 0.78 Å, relative to rMg^{2+} = 0.72 Å; Shannon, 1976) displays a slight preference for the smaller M1-site. Based on the ionic radii, site size and site distortion, we would expect Fe^{2+} to show a preference for the M2-site, as predicted by Burns (1970 and 1993). The small preference of Fe^{2+} for M1-site might be the result of a higher crystal field splitting energy gained by Fe^{2+} as the result of the smaller M1-O bond distance (Deer et al., 1997). However, although the study of Shinno et al. (1974) on plutonic and metamorphic olivine exhibits a relative enrichment of Fe^{2+} in M1-site, the two olivine of volcanic origin that the authors have investigated present a preferential ordering of Fe^{2+} in M2-site. Moreover, according to Redfern et al. (2000), Fe shows a preference for M1-site at temperature below 600 °C. Then, Fe becomes progressively disordered until 630 °C. At higher temperatures, Fe preferentially occupies the M2 polyhedron and becomes progressively more ordered into M2 with increasing temperature.

Trace cations in olivine (Ni^{2+}, Ca^{2+}, and Mn^{2+}) exhibit specific site preferences. The crystal field splitting parameter for the M1-site will be slightly larger than that for the larger M2-site. Hence, crystal field criteria suggest that the ions acquiring crystal field stabilization energy (CFSE) will be enriched in M1-position of the olivine structure, whereas those with no CFSE will prefer the M2 positions (Burns, 1970). Ni present a large CFSE of 29.2 kcal/mole (Henderson and Dale, 1968) and is expected to partition strongly into the M1-site. Conversely, Ca^{2+} and Mn^{2+} do not have CFSE in olivine and their partitioning is governed by the size. Both are relatively large, $rCa^{2+} = 1.00$ Å and $rMn^{2+} = 0.83$ Å (Shannon, 1976), consequently, Ca^{2+} and Mn^{2+} partition preferentially into the larger M2-site (Burns, 1970; Snyder and Carmichael, 1992). Chromium is present in natural olivine in two oxidation states, Cr^{2+} and Cr^{3+}, and both are octahedrally coordinated (Jollands et al. 2018). Cr^{2+} has been found in lunar and meteoritic olivine (Schreiber and Haskin, 1976; Sutton et al., 1993; McKeown et al., 2014) and is disordered between M1- and M2-sites (Li et al., 1995). On the contrary, Cr^{3+} dominates in terrestrial settings (Schreiber and Haskin, 1976; Bell et al., 2014; Jollands et al., 2018), and is always ordered into M1-site (Papike et al., 2005).

3. Partition coefficient

The partitioning of cations between olivine and melt is considered by some authors as a petrogenetic indicator. Olivine is an important mineral phase in igneous processes, both in relation to its role during partial melting of the upper mantle and during magmatic fractionation (Deer et al., 1997). The Nernst distribution law, better known as partition coefficient, or distribution coefficient, is a concept associating the concentration of an element in two different phases as:

$$Kd_i^{A-B} = \frac{a_i^A}{a_i^B} = \frac{C_i^A}{C_i^B} \qquad \text{Eqn. (1)}$$

where a is the activity of the element i in the phases A and B, whereas C is the concentration of the element i in the phases A and B (Ganguly, 2008; Mollo and Hammer, 2017; White, 2020). It can be measured either experimentally or observationally. In both cases, the focal point is the equilibrium of the system (White, 2020). Under kinetic effects (disequilibrium), chemical gradients develop in the melt adjacent to the crystal surface (IM), showing a different composition than the FFM. Indeed, by moving away from the crystal surface, chemical gradients cease, and the system returns to homogeneous concentrations. The partition coefficient measured between the advancing crystal and the IM, called ‘apparent’ partition coefficient, will be different from the partition coefficient calculated under equilibrium conditions, because of the effect of the chemical gradients in the melt (Mollo and Hammer, 2017 and White, 2020). The direct consequence is that the crystal might become less enriched in compatible elements and less depleted in incompatible elements than thermodynamic equilibrium would predict. An element is considered as ‘incompatible’ if its $Kd_i^{A-B} < 1$, and ‘compatible’ if $Kd_i^{A-B} \geq 1$. However, Kd for a given element can strongly varies between phases. Therefore, the use of the term compatible and incompatible has meaning only if the phases are specified (White, 2020).

3.1. Thermodynamic basis of element partitioning

In an equilibrium system, the distribution of elements between the co-existing phases will require that the chemical potential of the elements considered will be the same in each phase of the system (White, 2020). The chemical potential can be defined as a driving force that determines the distribution of components between phases of variable composition in a system. It tells us how the Gibbs Free Energy (measure of the capacity of the system to do chemical work) will vary with the number of moles of the element i holding temperature, pressure, and the number of moles of all other components constant as (White, 2020):

$$\mu_i = \mu_i^0 + RT\, lnX_i\lambda_i \qquad \text{Eqn. (2)}$$

where μ_i^0 is the chemical potential of the pure phase, i is the component, R is the gas constant, T is the temperature, X is the molar fraction and λ is the activity coefficient. The partition coefficient is related to the chemical potential as (White, 2020):

$$Kd_i^{A-B} = \frac{\lambda_i^B}{\lambda_i^A} exp\left(\frac{\mu_i^{oB} - \mu_i^{oA}}{RT}\right) \qquad \text{Eqn. (3)}$$

The difference in chemical potential expressed in the Eqn. (3) correspond to the standard state Gibbs Free Energy change resulting from transfer of i between these two phases (White, 2020). Therefore, $\mu_i^{oB} - \mu_i^{oA}$ can be expressed as $-\Delta G_i^{oA-B}$.

It is expected that elements present in small quantity will obey to Henry’s law (Ganguly, 2007 and White, 2020). Henry’s law was stated by William Henry. He discovered that when the mole fraction of a solute becomes very dilute (in trace), its partial pressure becomes proportional to mole fraction (Ganguly, 2007 and White, 2020). Therefore, the partitioning of an element i between two phases can be expressed as:

$$Kd_i^{A-B} = \frac{h_i^B}{h_i^A} exp\left(\frac{\mu_i^{oB} - \mu_i^{oA}}{RT}\right) \qquad \text{Eqn. (4)}$$

where h is the Henry's law constant. Later, several studies have shown that trace elements obey to Henry's law over their entire range of natural concentration (White, 2020). The comparison of the equilibrium constant with the derivation of the partition coefficient shows a close relation between the two of them, since the partition coefficient is a form of apparent equilibrium constant (White, 2020).

3.2. Parameters governing the partitioning of elements

Several factors are known to govern the value of the partition coefficient. Indeed, it is well known that the chemical potential (μ_i) depends on pressure, temperature, and the number of moles of all the other component of the solvent. Moreover, Henry's law constant (h_i) is also dependent of pressure and temperature (Ganguly, 2007 and White, 2020). Many authors have studied the partitioning of elements by investigating natural and experimental samples. They observed that for example, Ni, Mn, Ca, Cr, Ti, and Al partitioning between olivine and melt generally decreases as temperature increases (e.g., Schreiber and Haskin, 1976; Watson, 1977; Agee and Walker, 1990; Bédard, 2005; Matzen et al., 2013, 2017; Ammannati et al., 2016; Di Stefano et al., 2018; Figure 1.7). The same conclusion is found for Ni, Ca, and Ti as pressure increases (e.g., Stormer, 1973; Stephenson, 1974; Larsen, 1976; Bédard, 2005; Matzen et al., 2013, 2017; Ammannati et al., 2016; Figure 1.8a), except for Al, which increases with pressure (e.g., Agee and Walker, 1990; Bédard, 2005; Figure 1.8b).

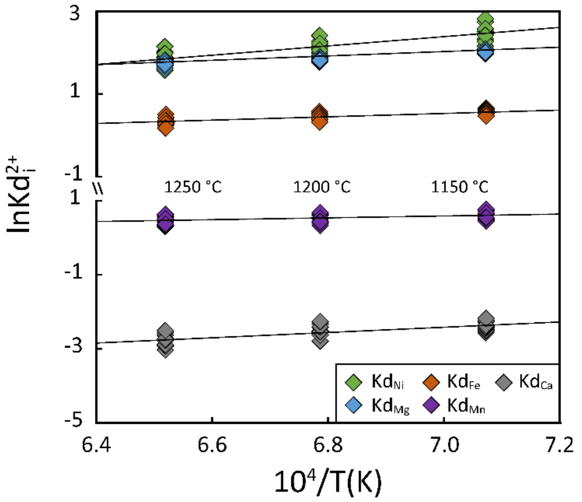

Figure 1.7. *(a) $\ln Kd_i^{2+}$ vs. 1/T diagram showing the linear correlation between divalent partition coefficient and temperature. After Di Stefano et al. (2018).*

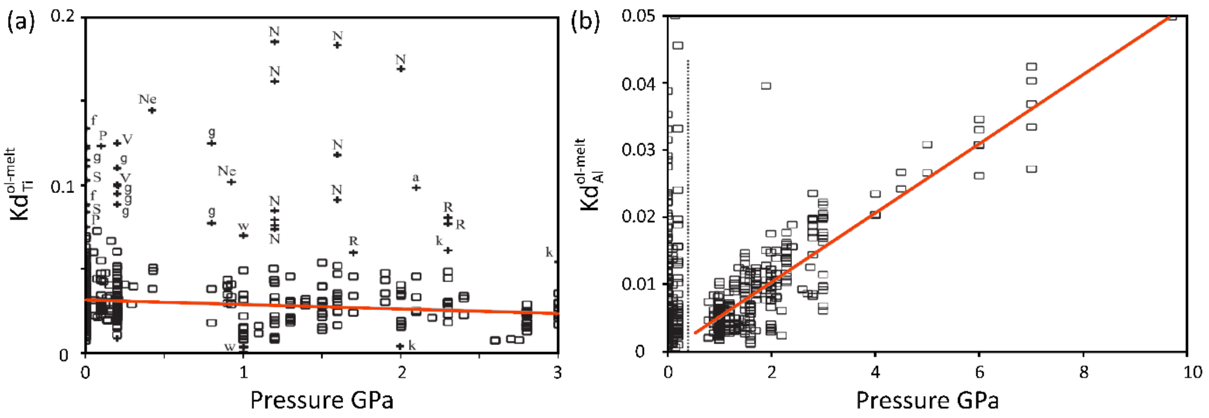

Figure 1.8. *(a) Kd_{Ti} vs. Pressure in GPa. Letters indicate the articles from which data were recovered (see table 1 of Bédard, 2005, for more details). (b) Kd_{Al} vs. Pressure in GPa. High-pressure data (> 0.5 GPa) show a positive corelation between Kd_{Al} and the pressure of the melt. Low-pressure data (< 0.5 GPa) show very scattered data. Redrawn and modified after Bédard (2005).*

Charge and size are also important for the partitioning of elements (White, 2020). Goldschmidt developed three rules concerning the substituting of elements into crystal structures, which will directly impact their partitioning (Goldschmidt, 1937). Ringwood added later a fourth rule (Ringwood, 1955):

- Rule 1: two ions with the same radius and same charge will enter a given lattice site with equal facility.
- Rule 2: if two ions have similar charge, the smaller one will enter in a given lattice site with more facility.
- Rule 3: if two ions have similar radii, the one with higher charge will enter in a given lattice site with more facility.
- Rule 4: if a substitution is possible between two elements, the one with lower electronegativity will be preferentially incorporated.

However, the key point is that the stronger the bond, the more likely the substitution (White, 2020).

The last factor controlling the partitioning of elements is the composition of the phases considered (in this study we consider olivine and glass) since the Henry’s law constant depend on the concentration of the major species. A part of this compositional dependence results from the need of coupled substitution to maintain the charge balance (e.g., elements can enter in crystal lattice by coupled substitutions, Colson et al., 1988; Beattie, 1994; Taura et al., 1998; Evans et al., 2008; Milman-Barris et al., 2008; Mallmann et al., 2009; Grant and Wood, 2010; Grant and Kohn, 2013; Mollo et al. 2013; Zhukova et al., 2017; Baudouin et al., 2020; Figure 1.9).

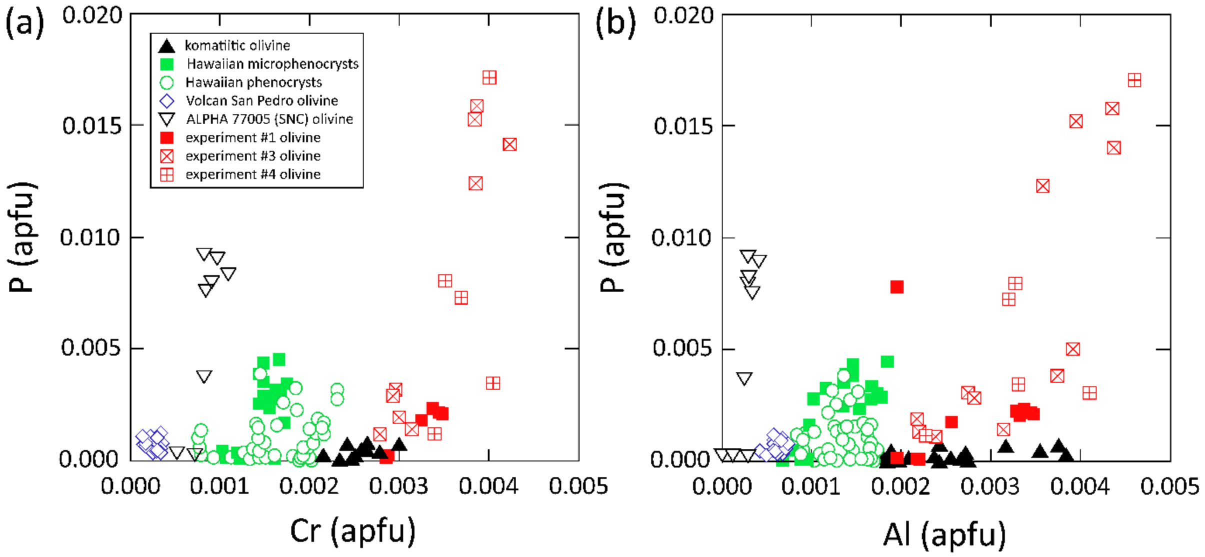

Figure 1.9. *Concentration of P, Al, and Cr in natural and synthetic olivine. (a) P vs. Cr; (b) P vs. Al. Analysis of the experiments of Milman-Barris et al., (2008) (red symbols) indicate an almost linear correlation between both P-Cr and P-Al pairs. Redrawn and modified after Milman-Barris et al., (2008).*

The olivine Fo content was also found to affect some elements, as it is the case for Ni, Mn, and Ca for example (e.g., Simkin and Smith, 1970; Watson, 1979a; Jurewicz and Watson, 1988a; Libourel, 1999; Wang and Gaetani, 2008; Figure 1.10a). Melt composition is known to be a factor controlling the partitioning of elements. However, most of the compositional dependency is related to the structural changes in the melt phase (Schmidt et al., 2006; White, 2020). The concentration of SiO_2 in the melt will directly impact on the polymerization of the melt. Indeed, as SiO_2 increases, the polymerization of the melt will increase as the Si-tetrahedra become more linked, and the changes in the partitioning of elements will more likely reflect the availability of appropriate coordinated sites in the melt (White, 2020). Additionally, if the polymerization of the melt increases, there will be less octahedral sites (or other sites) available for transition and highly charged cations in the melt. Therefore, these elements will preferentially partition into the solid phase (White, 2020). Several studies investigated the dependency of elements partitioning to the melt polymerization. The partitioning between olivine and melt of Ni, Mn, Ca, Cr, Ti, and P for example, is generally decreasing as the melt become less polymerized (e.g., Henderson and Dale, 1970; Watson, 1977; Takahashi, 1978; Kohn and Schofield, 1994; Hanson and Jones, 1998; Mysen and Dubinsky, 2004; Bédard, 2005; Mysen, 2007; Wang and Gaetani, 2008; Grant and Kohn, 2013; Di Stefano et al., 2018; Figure 1.10).

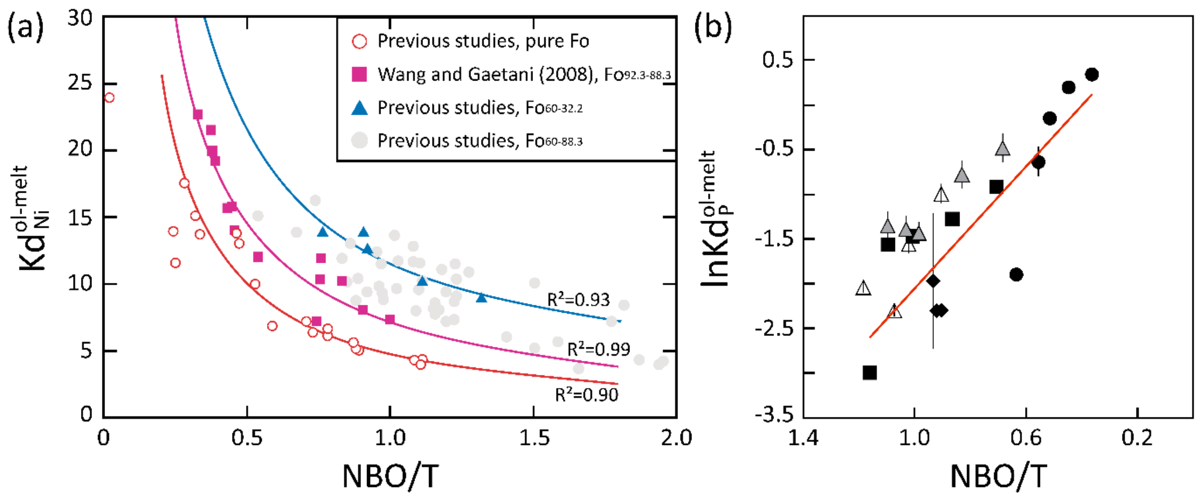

Figure 1.10. *(a) Kd_{Ni} vs. NBO/T (non-bridging oxygen per tetrahedra; lower is the value of NBO/T, higher is the melt polymerization). Pink square: data set from Wang and Gaetani (2008). Other symbols from previous studies (Bartels et al. 1991; Gaetani and Grove 1998; Grove and Bryan 1983; Grove et al. 1982; Gudfinnsson and Presnall 2000; Hart and Davis 1978; Kinzler 1997; Kinzler and Grove 1992; Kinzler et al. 1990; Libourel 1999; Longhi et al. 1978; Roeder and Emslie 1970; Sack et al. 1987; Shi 1993; Shi and Libourel 1991; Snyder and Carmichael 1992; Takahashi 1978; Tormey et al. 1987; Ulmer 1989; Walter 1998; Watson 1977) and organised for different ranges of Fo content in olivine. Lines are regressed using the Eqn. 6. Redrawn after Wang and Gaetani (2008). (b) $lnKd_P$ vs. NBO/T. Black squares: CR = 1 °C/h and T_{final} = 1400 °C; Black diamond: CR = 1 °C/h and T_{final} = 1400 °C and varying bulk P-concentration; Open triangle: CR = 5 °C/h; Grey triangle: CR = 10 °C/h. Red lines are least-squares linear fits through the 1 °C/h data only. Redrawn and modified after Grant and Kohn (2013).*

References – Chapter 1

Agee, C. B., & Walker, D. (1990). Aluminum partitioning between olivine and ultrabasic silicate liquid to 6 GPa. Contributions to Mineralogy and Petrology, 105(3), 243-254. doi.org/10.1007/BF00306537

Ammannati, E., Jacob, D. E., Avanzinelli, R., Foley, S. F., & Conticelli, S. (2016). Low Ni olivine in silica-undersaturated ultrapotassic igneous rocks as evidence for carbonate metasomatism in the mantle. Earth and Planetary Science Letters, 444, 64-74. doi.org/10.1016/j.epsl.2016.03.039

Balić Žunić, T., & Vicković, I. (1996). IVTON–a program for the calculation of geometrical aspects of crystal structures and some crystal chemical applications. Journal of Applied Crystallography, 29(3), 305-306. doi.org/10.1107/S0021889895015081

Baudouin, C., France, L., Boulanger, M., Dalou, C., & Devidal, J. L. (2020). Trace element partitioning between clinopyroxene and alkaline magmas: parametrization and role of M1 site on HREE enrichment in clinopyroxenes. Contributions to Mineralogy and Petrology, 175(5), 1-15. doi.org/10.1007/s00410-020-01680-6

Baziotis, I., Asimow, P. D., Ntaflos, T., Boyce, J. W., McCubbin, F. M., Koroneos, A., ... & Berndt, J. (2017). Phosphorus zoning as a recorder of crystal growth kinetics: application to second-generation olivine in mantle xenoliths from the Cima Volcanic Field. Contributions to Mineralogy and Petrology, 172(7), 1-32. doi.org/10.1007/s00410-017-1376-7

Beattie, P. (1994). Systematics and energetics of trace-element partitioning between olivine and silicate melts: Implications for the nature of mineral/melt partitioning. Chemical Geology, 117(1-4), 57-71. doi.org/10.1016/0009-2541(94)90121-X

Bédard, J. H. (2005). Partitioning coefficients between olivine and silicate melts. Lithos, 83(3-4), 394-419. doi.org/10.1016/j.lithos.2005.03.011

Bell, A. S., Burger, P. V., Le, L., Shearer, C. K., Papike, J. J., Sutton, S. R., ... & Jones, J. (2014). XANES measurements of Cr valence in olivine and their applications to planetary basalts. American Mineralogist, 99(7), 1404-1412. doi.org/10.2138/am.2014.4646

Birle, J. D., Gibbs, G. V., Moore, P. B., & Smith, J. V. (1968). Crystal structures of natural olivines. American Mineralogist: Journal of Earth and Planetary Materials, 53(5-6), 807-824.

Bragg. W. L., and Brown. G.B. (1926) Die Struktur des Olivins. Zeitschrift für Kristallographie-Crystalline Materials, 63(1-6), 538-556. doi.org/10.1524/zkri.1926.63.1.538

Brown, G., & Prewitt, C. T. (1973). High-temperature cystal chemistry of hortonolite. American Mineralogist: Journal of Earth and Planetary Materials, 58(7-8), 577-587.

Bryan, W. B. (1972). Morphology of quench crystals in submarine basalts. Journal of Geophysical Research, 77(29), 5812-5819. doi.org/10.1029/JB077i029p05812

Burns, R. G. (1970). Site preferences of transition metal ions in silicate crystal structures. Chemical Geology, 5(4), 275-283. doi.org/10.1016/0009-2541(70)90045-8

Bush, W. R., Hafner, S. S., & Virgo, D. (1970). Some ordering of iron and magnesium at the octahedrally coordinated sites in a magnesium-rich olivine. Nature, 227(5265), 1339-1341. doi.org/10.1038/2271339b0

Colson, R. O., McKay, G. A., & Taylor, L. A. (1989). Charge balancing of trivalent trace elements in olivine and low-Ca pyroxene: A test using experimental partitioning data. Geochimica et Cosmochimica Acta, 53(3), 643-648. doi.org/10.1016/0016-7037(89)90007-0

Cordier, P., Demouchy, S., Beausir, B., Taupin, V., Barou, F., & Fressengeas, C. (2014). Disclinations provide the missing mechanism for deforming olivine-rich rocks in the mantle. Nature, 507(7490), 51-56. doi.org/10.1038/nature13043

Cressey G., Howie R.A.. Minerals; olivines, Encyclopedia of Geology, 2005, Volume 3, Elsevier (p. 557-561). doi.org/10.1016/B0-12-369396-9/00263-X

Deer, W.A., Howie, R.A., Zussman, J. (1997): Rock-forming minerals. Orthosilicates. 2nd ed., London: Geological Soc., 919 p.

Del Gaudio, P., Mollo, S., Ventura, G., Iezzi, G., Taddeucci, J., & Cavallo, A. (2010). Cooling rate-induced differentiation in anhydrous and hydrous basalts at 500 MPa: Implications for the storage and transport of magmas in dikes. Chemical Geology, 270(1-4), 164-178. doi.org/10.1016/j.chemgeo.2009.11.014

Di Stefano, F., Mollo, S., Scarlato, P., Nazzari, M., Bachmann, O., & Caruso, M. (2018). Olivine compositional changes in primitive magmatic skarn environments: A reassessment of divalent cation partitioning models to quantify the effect of carbonate assimilation. Lithos, 316, 104-121. doi.org/10.1016/j.lithos.2018.07.008

Donaldson, C. H. (1976). An experimental investigation of olivine morphology. Contributions to mineralogy and Petrology, 57(2), 187-213. doi.org/10.1007/BF00405225

Donaldson, C. H. (1974). Olivine crystal types in harrisitic rocks of the Rhum pluton and in Archean spinifex rocks. Geological Society of America Bulletin, 85(11), 1721-1726. doi.org/10.1130/0016-7606(1974)85<1721:OCTIHR>2.0.CO;2

Evans, T. M., O’Neill, H. S. C., & Tuff, J. (2008). The influence of melt composition on the partitioning of REEs, Y, Sc, Zr and Al between forsterite and melt in the system CMAS. Geochimica et Cosmochimica Acta, 72(23), 5708-5721. doi.org/10.1016/j.gca.2008.09.017

Faure, F., Trolliard, G., Nicollet, C., & Montel, J. M. (2003). A developmental model of olivine morphology as a function of the cooling rate and the degree of undercooling. Contributions to Mineralogy and Petrology, 145(2), 251-263. doi.org/10.1007/s00410-003-0449-y

Faure, F., Schiano, P., Trolliard, G., Nicollet, C., & Soulestin, B. (2007). Textural evolution of polyhedral olivine experiencing rapid cooling rates. Contributions to Mineralogy and Petrology, 153(4), 405-416. doi.org/10.1007/s00410-006-0154-8

Ganguly, J. (2008). Thermodynamics in earth and planetary sciences. Berlin: Springer.

Goldschmidt, V. M. (1937). The principles of distribution of chemical elements in minerals and rocks. The seventh Hugo Müller Lecture, delivered before the Chemical Society on March 17th, 1937. Journal of the Chemical Society (Resumed), 655-673.

Grant, T. B., & Kohn, S. C. (2013). Phosphorus partitioning between olivine and melt: An experimental study in the system Mg2SiO4-Ca2Al2Si2O9-NaAlSi3O8-Mg3 (PO4) 2. American Mineralogist, 98(10), 1860-1869. doi.org/10.2138/am.2013.4237

Grant, K. J., & Wood, B. J. (2010). Experimental study of the incorporation of Li, Sc, Al and other trace elements into olivine. Geochimica et Cosmochimica Acta, 74(8), 2412-2428. doi.org/10.1016/j.gca.2010.01.015

Hammer, J. E. (2008). Experimental studies of the kinetics and energetics of magma crystallization. Reviews in mineralogy and geochemistry, 69(1), 9-59. doi.org/10.2138/rmg.2008.69.2

Hammer, J. E. (2006). Influence of fO2 and cooling rate on the kinetics and energetics of Fe-rich basalt crystallization. Earth and Planetary Science Letters, 248(3-4), 618-637. doi.org/10.1016/j.epsl.2006.04.022

Hanke, K. (1965). Beiträge zu Kristallstrukturen vom Olivin-Typ. Beiträge zur Mineralogie und Petrographie, 11(6), 535-558.

Hanson, B., & Jones, J. H. (1998). The systematics of Cr3+ and Cr2+ partitioning between olivine and liquid in the presence of spinel. American Mineralogist, 83(7-8), 669-684. doi.org/10.2138/am-1998-7-801

Henderson, P., & Dale, I. M. (1970). The partitioning of selected transition element ions between olivine and groundmass of oceanic basalts. Chemical Geology, 5(4), 267-274. doi.org/10.1016/0009-2541(70)90044-6

Herlach, D. M., & Feuerbacher, B. (1986). Nucleation and undercooling. In Materials Sciences in Space (pp. 168-190). Springer, Berlin, Heidelberg. doi.org/10.1007/978-3-642-82761-7_8

Iezzi, G., Mollo, S., Torresi, G., Ventura, G., Cavallo, A., & Scarlato, P. (2011). Experimental solidification of an andesitic melt by cooling. Chemical Geology, 283(3-4), 261-273. doi.org/10.1016/j.chemgeo.2011.01.024

Jollands, M. C., O'Neill, H. S. C., Van Orman, J., Berry, A. J., Hermann, J., Newville, M., & Lanzirotti, A. (2018). Substitution and diffusion of Cr2+ and Cr3+ in synthetic forsterite and natural olivine at 1200–1500 C and 1 bar. Geochimica et cosmochimica acta, 220, 407-428. doi.org/10.1016/j.gca.2017.09.030

Jurewicz, A. J., & Watson, E. B. (1988). Cations in olivine, Part 2: Diffusion in olivine xenocrysts, with applications to petrology and mineral physics. Contributions to Mineralogy and Petrology, 99(2), 186-201.

Kirkpatrick R.J. (1981) Kinetics of crystallization of igneous rocks. Rev Mineral Geochem 8:321-397

Kitayama, K., & Katsura, T. (1968). Activity measurements in orthosilicate and metasilicate solid solutions. I. Mg2SiO4-Fe2SiO4 and MgSiO3-FeSiO3 at 1204 C. Bulletin of the Chemical Society of Japan, 41(5), 1146-1151.

Kohn, S. C., & Schofield, P. F. (1994). The importance of melt composition in controlling trace-element behaviour: an experimental study of Mn and Zn partitioning between forsterite and silicate melts. Chemical Geology, 117(1-4), 73-87. doi.org/10.1016/0009-2541(94)90122-8

Larsen, L. M. (1976). Clinopyroxenes and coexisting mafic minerals from the alkaline Ilimaussaq intrusion, South Greenland. Journal of Petrology, 17(2), 258-290. doi.org/10.1093/petrology/17.2.258

Lasaga, A. C. (1982). Toward a master equation in crystal growth. American Journal of Science, 282(8), 1264-1288.

Li, J. P., O'Neil, H. S. C., & Seifert, F. (1995). Subsolidus Phase Relations in the System MgO—SiO2—Gr—O in Equilibrium with Metallic Cr, and their Significance for the Petrochemistry of Chromium. Journal of Petrology, 36(1), 107-132. doi.org/10.1093/petrology/36.1.107

Libourel, G. (1999). Systematics of calcium partitioning between olivine and silicate melt: implications for melt structure and calcium content of magmatic olivines. Contributions to Mineralogy and Petrology, 136(1), 63-80. doi.org/10.1007/s004100050524

Mahan, B. (2021). Element Partitioning (Mineral-Melt, Metal-/Sulfide-Silicate) in Planetary Sciences. In Oxford Research Encyclopedia of Planetary Science. doi.org/10.1093/acrefore/9780190647926.013.202

Mallmann, G., O'Neill, H. S. C., & Klemme, S. (2009). Heterogeneous distribution of phosphorus in olivine from otherwise well-equilibrated spinel peridotite xenoliths and its implications for the mantle geochemistry of lithium. Contributions to Mineralogy and Petrology, 158(4), 485-504. doi.org/10.1007/s00410-009-0393-6

Matzen, A. K., Baker, M. B., Beckett, J. R., Wood, B. J., & Stolper, E. M. (2017). The effect of liquid composition on the partitioning of Ni between olivine and silicate melt. Contributions to Mineralogy and Petrology, 172(1), 1-18. doi.org/10.1007/s00410-016-1319-8

Matzen, A. K., Baker, M. B., Beckett, J. R., & Stolper, E. M. (2013). The temperature and pressure dependence of nickel partitioning between olivine and silicate melt. Journal of Petrology, 54(12), 2521-2545. doi.org/10.1093/petrology/egt055

McKeown, D. A., Buechele, A. C., Tappero, R., McCoy, T. J., & Gardner-Vandy, K. G. (2014). X-ray absorption characterization of Cr in forsterite within the MacAlpine Hills 88136 EL3 chondritic meteorite. American Mineralogist, 99(1), 190-197. doi.org/10.2138/am.2014.4508

Milman-Barris, M. S., Beckett, J. R., Baker, M. B., Hofmann, A. E., Morgan, Z., Crowley, M. R., ... & Stolper, E. (2008). Zoning of phosphorus in igneous olivine. Contributions to Mineralogy and Petrology, 155(6), 739-765. doi.org/10.1007/s00410-007-0268-7

Mollo, S., & Hammer, J. E. (2017). Dynamic crystallization in magmas. EMU Notes Mineral, 16, 373-418. doi.org/10.1180/EMU-notes.16.12

Mollo, S., Blundy, J. D., Iezzi, G., Scarlato, P., & Langone, A. (2013b). The partitioning of trace elements between clinopyroxene and trachybasaltic melt during rapid cooling and crystal growth. Contributions to Mineralogy and Petrology, 166(6), 1633-1654. doi.org/10.1007/s00410-013-0946-6

Mollo, S., Lanzafame, G., Masotta, M., Iezzi, G., Ferlito, C., & Scarlato, P. (2011). Cooling history of a dike as revealed by mineral chemistry: a case study from Mt. Etna volcano. Chemical Geology, 288(1-2), 39-52. doi.org/10.1016/j.chemgeo.2011.06.016

Mollo, S., Del Gaudio, P., Ventura, G., Iezzi, G., & Scarlato, P. (2010). Dependence of clinopyroxene composition on cooling rate in basaltic magmas: Implications for thermobarometry. Lithos, 118(3-4), 302-312. doi.org/10.1016/j.lithos.2010.05.006

Morozov, M., Brinkmann, C., Lottermoser, W., Tippelt, G., Amthauer, G., & Kroll, H. (2005). Octahedral cation partitioning in Mg, Fe2+-olivine. Mossbauer spectroscopic study of synthetic (Mg0. 5 Fe2+ 0.5) 2SiO4 (Fa50). European Journal of Mineralogy, 17(3), 495-500. doi.org/10.1127/0935-1221/2005/0017-0495

Mysen, B. (2007). Partitioning of calcium, magnesium, and transition metals between olivine and melt governed by the structure of the silicate melt at ambient pressure. American Mineralogist, 92(5-6), 844-862. doi.org/10.2138/am.2007.2260

Mysen, B. O., & Dubinsky, E. V. (2004). Melt structural control on olivine/melt element partitioning of Ca and Mn. Geochimica et Cosmochimica Acta, 68(7), 1617-1633. doi.org/10.1016/j.gca.2003.09.010

Nafziger, R. H., & Muan, A. (1967). Equilibrium phase compositions and thermodynamic properties of olivines and pyroxenes in the system MgO-“FeO” SiO2. American Mineralogist: Journal of Earth and Planetary Materials, 52(9-10), 1364-1385.

Pamato, M. G., Nestola, F., Novella, D., Smyth, J. R., Pasqual, D., Gatta, G., ... & Secco, L. (2019). The high-pressure structural evolution of olivine along the forsterite–fayalite join. Minerals, 9(12), 790. doi.org/10.3390/min9120790

Papike, J. J., Karner, J. M., & Shearer, C. K. (2005). Comparative planetary mineralogy: Valence state partitioning of Cr, Fe, Ti, and V among crystallographic sites in olivine, pyroxene, and spinel from planetary basalts. American Mineralogist, 90(2-3), 277-290. doi.org/10.2138/am.2005.1779

Redfern, S. A. T., Artioli, G., Rinaldi, R., Henderson, C. M. B., Knight, K. S., & Wood, B. J. (2000). Octahedral cation ordering in olivine at high temperature. II: an in-situ neutron powder diffraction study on synthetic MgFeSiO 4 (Fa50). Physics and Chemistry of Minerals, 27(9), 630-637. doi.org/10.1007/s002690000109

Ringwood, A. E. (1955). The principles governing trace element distribution during magmatic crystallization Part I: The influence of electronegativity. Geochimica et Cosmochimica Acta, 7(3-4), 189-202.

Sahama, T. G., & Torgeson, D. R. (1949). Thermochemical study of the olivines and orthopyroxenes (Vol. 4408). US Department of the Interior, Bureau of Mines.

Schmidt, M. W., Connolly, J. A. D., Günther, D., & Bogaerts, M. (2006). Element partitioning: the role of melt structure and composition. Science, 312(5780), 1646-1650. doi.org/10.1126/science.1126690

Schreiber, H. D., & Haskin, L. A. (1976). Chromium in basalts: Experimental determination of redox states and partitioning among synthetic silicate phases. In Lunar and planetary science conference proceedings (Vol. 7, pp. 1221-1259).

Shannon, R. D. (1976). Revised effective ionic radii and systematic studies of interatomic distances in halides and chalcogenides. Acta crystallographica section A: crystal physics, diffraction, theoretical and general crystallography, 32(5), 751-767. doi.org/10.1107/S0567739476001551

Shea, T., Hammer, J. E., Hellebrand, E., Mourey, A. J., Costa, F., First, E. C., ... & Melnik, O. (2019). Phosphorus and aluminum zoning in olivine: contrasting behaviour of two nominally incompatible trace elements. Contributions to Mineralogy and Petrology, 174(10), 1-24. doi.org/10.1007/s00410-019-1618-y

Shinno, I., Hayashi, M., & Kuroda, Y. (1974). Mössbauer studies of natural olivines. Mineralogical Journal, 7(4), 344-358. doi.org/10.2465/minerj1953.7.344

Simkin, T., & Smith, J. V. (1970). Minor-element distribution in olivine. The Journal of Geology, 78(3), 304-325.

Smith, V. G., Tiller, W. A., & Rutter, J. (1955). A mathematical analysis of solute redistribution during solidification. Canadian Journal of Physics, 33(12), 723-745. doi.org/10.1139/p55-089

Smyth, J. R. (1975). High temperature crystal chemistry of fayalite. American Mineralogist: Journal of Earth and Planetary Materials, 60(11-12), 1092-1097.

Smyth, J. R., & Hazen, R. M. (1973). The crystal structures of forsterite and hortonolite at several temperatures up to 900 C. American Mineralogist: Journal of Earth and Planetary Materials, 58(7-8), 588-593.

Snyder, D. A., & Carmichael, I. S. (1992). Olivine-liquid equilibria and the chemical activities of FeO, NiO, Fe2O3, and MgO in natural basic melts. Geochimica et Cosmochimica Acta, 56(1), 303-318. doi.org/10.1016/0016-7037(92)90135-6

Stephenson, D. (1974). Mn and Ca enriched olivines from nepheline syenites of the South Qoroq Centre, south Greenland. Lithos, 7(1), 35-41. doi.org/10.1016/0024-4937(74)90036-X

Stormer Jr, J. C. (1973). Calcium zoning in olivine and its relationship to silica activity and pressure. Geochimica et Cosmochimica Acta, 37(8), 1815-1821. doi.org/10.1016/0016-7037(73)90144-0

Sutton, S. R., Jones, K. W., Gordon, B., Rivers, M. L., Bajt, S., & Smith, J. V. (1993). Reduced chromium in olivine grains from lunar basalt 15555: X-ray absorption near edge structure (XANES). Geochimica et Cosmochimica Acta, 57(2), 461-468. doi.org/10.1016/0016-7037(93)90444-2

Takahashi, E. (1978). Partitioning of Ni2+, Co2+, Fe2+, Mn2+ and Mg2+ between olivine and silicate melts: compositional dependence of partition coefficient. Geochimica et Cosmochimica Acta, 42(12), 1829-1844. doi.org/10.1016/0016-7037(78)90238-7

Taura, H., Yurimoto, H., Kurita, K., & Sueno, S. (1998). Pressure dependence on partition coefficients for trace elements between olivine and the coexisting melts. Physics and Chemistry of Minerals, 25(7), 469-484. doi.org/10.1007/s002690050138

Tiller, W. A., Jackson, K. A., Rutter, J. W., & Chalmers, B. (1953). The redistribution of solute atoms during the solidification of metals. Acta metallurgica, 1(4), 428-437. doi.org/10.1016/0001-6160(53)90126-6

Vetere, F., Iezzi, G., Behrens, H., Holtz, F., Ventura, G., Misiti, V., Cavallo, A., Mollo, S., & Marcel, D. (2015). Glass forming ability and crystallisation behaviour of sub-alkaline silicate melts. Earth-science reviews, 150, 25-44. doi.org/10.1016/j.earscirev.2015.07.001.

Virgo, D., & Hafner, S. S. (1972). Temperature-dependent Mg, Fe distribution in a lunar olivine. Earth and Planetary Science Letters, 14(3), 305-312. doi.org/10.1016/0012-821X(72)90129-X

Wang, Z., & Gaetani, G. A. (2008). Partitioning of Ni between olivine and siliceous eclogite partial melt: experimental constraints on the mantle source of Hawaiian basalts. Contributions to Mineralogy and Petrology, 156(5), 661-678. doi.org/10.1007/s00410-008-0308-y

Watson, E. B., Cherniak, D. J., & Holycross, M. E. (2015). Diffusion of phosphorus in olivine and molten basalt. American Mineralogist, 100(10), 2053-2065. doi.org/10.2138/am-2015-5416

Watson, E. B., & Müller, T. (2009). Non-equilibrium isotopic and elemental fractionation during diffusion-controlled crystal growth under static and dynamic conditions. Chemical Geology, 267(3-4), 111-124. doi.org/10.1016/j.chemgeo.2008.10.036

Watson, E. B. (1979a). Calcium content of forsterite coexisting with silicate liquid in the system Na, O-CaO-MgO-ALO3-SiO2. American Mineralogist, 64, 824-829.

Watson, E. B. (1977). Partitioning of manganese between forsterite and silicate liquid. Geochimica et Cosmochimica Acta, 41(9), 1363-1374. doi.org/10.1016/0016-7037(77)90079-5

White, W. M. (2020). Geochemistry. John Wiley & Sons.

Zhukova, I., O’Neill, H., & Campbell, I. H. (2017). A subsidiary fast-diffusing substitution mechanism of Al in forsterite investigated using diffusion experiments under controlled thermodynamic conditions. Contributions to Mineralogy and Petrology, 172(7), 1-12. doi.org/10.1007/s00410-017-1365-x

Chapter 2

Experimental and analytical methods

Table of content - Chapter 2

1. Introduction 46
2. Starting material preparation 46
    2.1. Glassy powder 46
    2.2. Experimental charge preparation 48
3. Experimental strategy 48
4. Sample preparation 50
5. Analytical techniques 51
    5.1. Historical development 51
    5.2. Scanning Electron Microscopy (SEM) 52
        5.2.1. Principle 52
        5.2.2. SEM imaging and limits 53
        5.2.3. SEM qualitative analysis and limits 55
        5.2.4. SEM analytical conditions for this study 56
    5.3. Electron Microprobe Analysis (EMPA) 56
        5.3.1. Principle and limits 56
        5.3.2. EMP analytical condition for this study 56
References – Chapter 2 58

Chapter 2

Experimental and analytical methods

1. Introduction

This chapter deals with the experimental and analytical techniques used to produce and analyse synthetic olivine crystals growing from a basaltic melt and explore the partitioning of cations and their substitution reactions.

Firstly, I will present the preparation of the starting material, followed by the details of the experimental strategy used in this project. Secondly, I will present the analytical techniques used to analyse olivine and residual melt in the samples. Electronic microscopy (Scanning Electron Microscope, SEM) was used to study the crystal texture, check the mineralogy of the sample, and determine the spatial repartition of elements in the crystals. I also used the technique of X-ray to determine the precise chemical composition of my samples (Electron MicroProbe Analysis, EMPA).

2. Starting material preparation

2.1. Glassy powder

The raw material used to produce the starting glass is a tholeiitic basalt (i.e., golden pumice) from the 1820 CE eruption of Kilauea (Garcia et al., 2003; Lynn et al., 2017; Shea et al., 2019). A sample of this pumice was sent to me by Thomas Shea (University of Hawaii). The natural sample has been finely powdered at the CRPG-CNRS (Centre de Recherches Pétrographiques et Géochimiques – Centre National de la Recherche Scientifique) laboratory of Vandoeuvre-lès-Nancy in France. A small part of this sample was analysed at the Service d'Analyses des Roches et des Minéraux (SARM, CRPG, France) to determine major and trace element concentrations (Table 2.1). Iron oxalate (~3 wt.% FeO) has been added, as previously quantified for primitive products (e.g., Freda et al., 2008), to minimize iron loss during the synthesis. A Fe-presaturated Pt-crucible containing the sample batches was loaded in a Nabertherm $MoSi_2$ chamber furnace (Nabertherm HT16/17) installed at the Volcanology and Experimental

Petrology laboratory of Roma Tre University, Italy. The glass synthesis was performed at 1 atm and temperature was kept constant at 1500 °C for 1h before raising the temperature to 1600 °C for 1 h to ensure a full melting of the rock-powder. Then the melt was rapidly quenched in a water bath to avoid the formation of microcrystals and oxides. The resulting glass was removed from the Pt-crucible and finely powdered using an agate mortar. Glassy powders were sent back at the SARM to reanalyse the concentrations of major and trace elements (Table 2.1).

(wt.%)	Natural rock powder	Starting material
SiO_2	48.68	47.28
Al_2O_3	11.87	11.64
Fe_2O_3	13.15	16.03
MnO	0.18	0.18
MgO	11.29	10.95
CaO	9.56	9.33
Na_2O	1.94	1.91
K_2O	0.39	0.39
TiO_2	2.23	2.18
P_2O_5	0.24	0.22
Total	99.62	99.61

Table 2.1. *Major, minor and trace elements of the natural rock powder and the starting material.*

2.2. Experimental charge preparation

Pt-loops of ~2 mm diameter (internal diameter) were charged with ~ 50 µg of powdered starting material mixed with polyvinyl alcohol to form a thick paste that is then inserted at the center of the loops (cf. Mollo and Vona, 2014; Di Stefano et al., 2018; Figure 2.1). This technique allows to charge the glassy powder to the Pt-wire rather than using a Pt-capsule and, therefore, reducing the Fe-Pt interaction between the starting material and the sample holder.

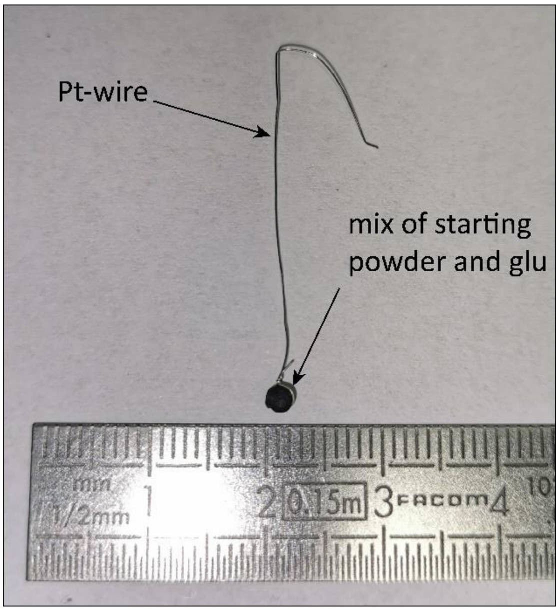

Figure 2.1. *Photo of a Pt-loop containing the glassy powder.*

3. Experimental strategy

Experiments were performed in a 1 atm vertical tube CO-CO_2 gas-mixing furnace (Nabertherm Furnace RHTV 120-300/18; Figure 2.2) installed at the HP-HT Laboratory of Experimental Volcanology and Geophysics of the Istituto Nazionale di Geofisica et Vulcanologia (INGV), Rome, Italy. Several experimental batches were designed to isolate the effects of undercooling and cooling rate without crossing interferences. For this reason, the other parameters were kept constant (Table 2.2).

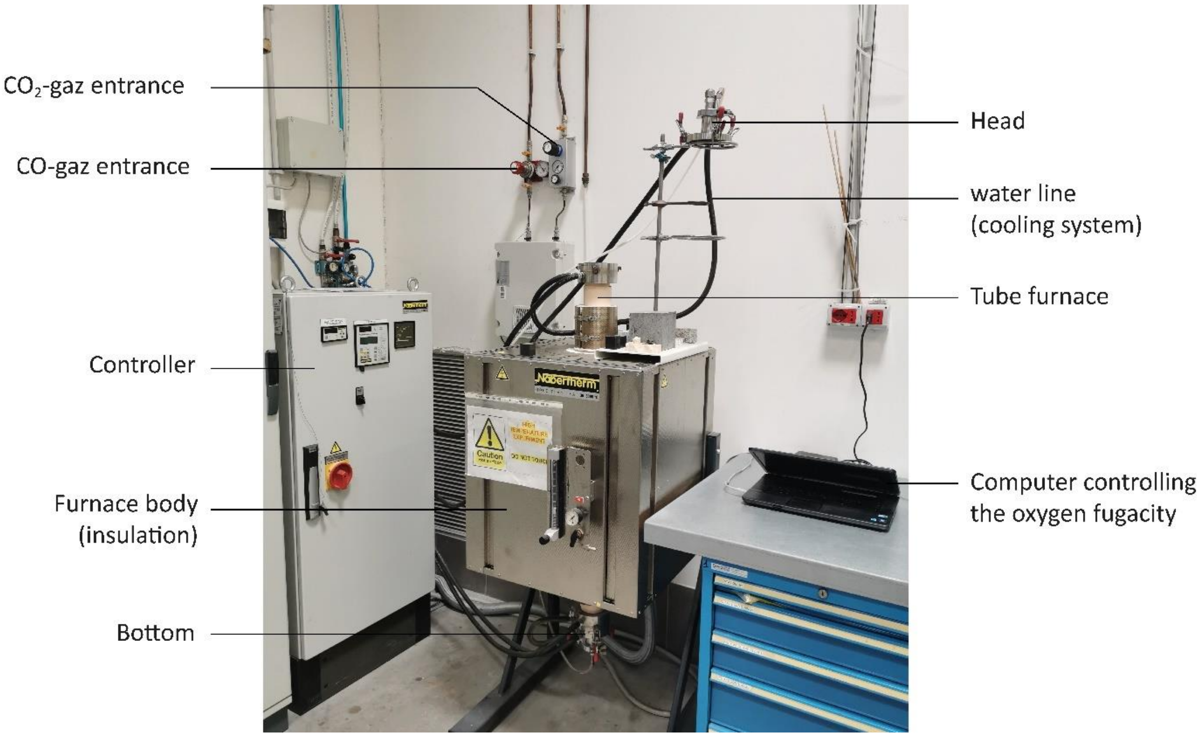
CO$_2$-gaz entrance
CO-gaz entrance
Controller
Furnace body (insulation)
Bottom
Head
water line (cooling system)
Tube furnace
Computer controlling the oxygen fugacity

Figure 2.2. *Photo of the 1 atm vertical tube CO-CO$_2$ gas-mixing furnace Nabertherm Furnace RHTV 120-300/18 installed at the laboratory HP-HT of INGV in Rome, Italy.*

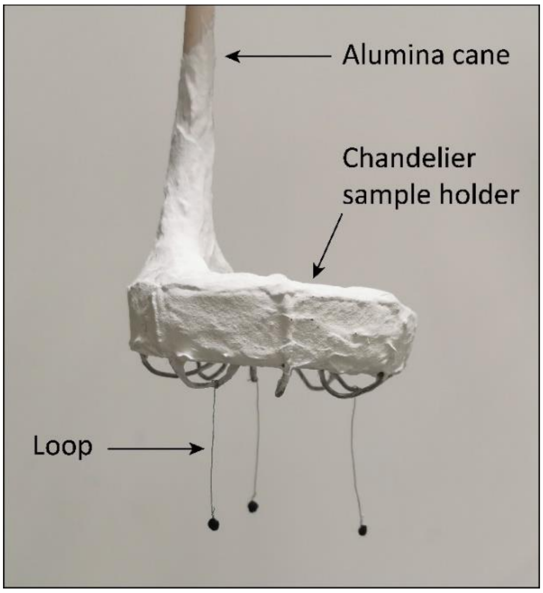
Alumina cane
Chandelier sample holder
Loop

Figure 2.3. *Photo of the chandelier sample holder with the experimental charges.*

Experiments were conducted under the QFM-2 buffering condition. The oxygen fugacity was monitored and maintained constant by an Yttria-doped-zirconia solid electrolyte oxygen sensor (SIRO2, Ceramic Oxide Fabricators, Ltd., Australia) and two digital thermal mass flow meters for CO and CO_2 controlled via software. Each experiment was performed with several loops suspended simultaneously to a chandelier sample holder (Figure 2.3). This latter is placed in the tube to place the samples in the hotspot zone. The samples were heated at a rate of 20 °C/min from room temperature to the superliquidus temperature of 1250 °C, above the basalt liquidus temperature estimated at 1210 °C. Temperature was measured by a Pt-Pt90Rh10 thermocouple, with uncertainty of ±3 °C, which was located within 1 cm of the sample chandelier holding the experimental charges. Superliquidus treatment was adopted by keeping the temperature constant for 1 hour. Then, the experimental charges were cooled at a rate of 4, 20, and 60 °C/h (CR4, CR20, and CR60, respectively) to the target temperatures of 1175 °C and 1125 °C, corresponding to undercoolings of 35 °C ($-\Delta T$ = 35 °C; $-\Delta T35$) and 85 °C ($-\Delta T$ = 85 °C; $-\Delta T85$), respectively. Then, the chandelier was dropped into a water bath, allowing a very fast quench (to freeze the system and avoid the crystallization of quench-phases, which would modify the composition of the remaining glass). It is important to note that the superheating temperature used for all my experiments is always the same. Thus, any effect that superheating temperature might have on olivine growth (First et al., 2020) will be identical between each experiment. All the experimental parameters are listed in Table 2.3.

Name experiment	Pressure	fO_2	H_2O	Starting temperature	Heating rate	Liquidus temperature (T_{liq})	Superliquidus temperature	Superliquidus treatment (dwell-time)	Cooling rate	Undercooling ($-\Delta T = T_{liq} - T_{final}$)	Final temperature (T_{final})
	(atm)	*(QFM buffer)*	*(wt. %)*	*(°C)*	*(°C/min)*	*(°C)*	*(°C)*	*(h)*	*(°C/h)*	*(°C)*	*(°C)*
VF4_35_UD	1	-2	0	24	20	1210	1250	1	4	35	1175
VF20_35_UD	1	-2	0	24	20	1210	1250	1	20	35	1175
VF60_35_UD	1	-2	0	24	20	1210	1250	1	60	35	1175
VF4_85_UD	1	-2	0	24	20	1210	1250	1	4	85	1125
VF20_85_UD	1	-2	0	24	20	1210	1250	1	20	85	1125
VF60_85_UD	1	-2	0	24	20	1210	1250	1	60	85	1125

Table 2.2. *Experimental conditions*

4. Sample preparation

The recovered experimental charges were mounted in epoxy (Figure 2.4) and polished for in situ measurements. One of the most important parameters in the preparation of the run product is the surface condition of the sample. This latter must be attained properly to minimize the effect of the topography, which would decrease the quality of images and analytical signals. The polishing of the epoxy block containing the samples is performed with silicon carbide abrasive foils (SiC) of decreasing grainsize (from 500 to 5000 grains/cm²). Then, polishing clothes with diamond paste of grainsize decreasing from 3 to ¼ µm are used with the polishing machine Struers Labopol. This step allows to obtain a very fine, smooth, and precise polishing.

When using electron microscopy technique, some materials may negatively charge under the electron beam. The negative charge at the surface of the sample repels the incident electrons, causing bad quality imaging and analysis. To inhibit charging at the sample surface, it is required to coat the samples with metal or carbon (10 to 20 nm thick film). In the case of this thesis, we used the JEOL JEC-530 to carbon coat the samples. A fine stream of carbon is deposited onto the samples by heating in a vacuum system between two high-current electrical terminals a source of carbon (thread or rod) until evaporation temperature.

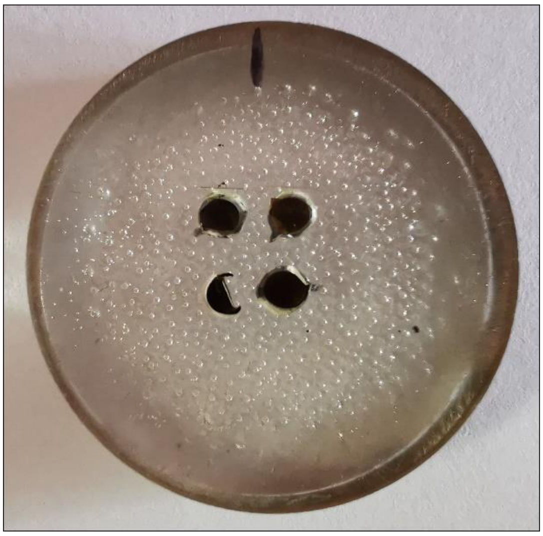

Figure 2.4. *Picture of samples mounted in epoxy and polished for analysis*

5. Analytical techniques

5.1. Historical development

In 1925, Louis De Broglie postulated in his Ph.D. thesis that electrons have a wave nature. He suggested that all matter has wave properties and that these waves propagate all over physical space and even faster than the speed of light. In 1926, Hans Busch invented the first electromagnetic lens, but it was Ernst Ruska and Max Knoll who created the first transmission electron microscope in 1931. In 1933, Ruska built the first electron microscope that exceeded the resolution attainable with an optical microscope. But it was not before 1937 that Manfred von Ardenne invented the first scanning electron microscope. Today, SEM is still the most used observation device in many scientific domains.

In 1950, Raimond Castaing developed the first electron microprobe (EMP) by fitting a crystal spectrometer to a modified electron microscope. The first prototype was presented in 1955 at the physics exhibition of la Sorbonne and commercialised in 1958 by the company CAMECA. However, Castaing did not equipped his microprobe with scanning imaging, and it will take some time before CAMECA added this device to their microprobe.

5.2. Scanning Electron Microscopy (SEM)

SEM is a highly used device for studying natural and experimental rocks mainly because of the simplicity of the sample preparation allowing to perform imaging of area from 1 cm to 5 µm width. Generally, SEM systems can provide a maximum resolution between 1 (for high resolution FEG-SEM) and 4 nm (for general purpose SEM). Moreover, SEM analysis are not destructive, therefore, other analysis can be performed latter on the same areas.

The SEM was very useful in this study to (i) take SEI (secondary electron images) and BSE (back-scattered electron) images of the crystals, determine the olivine morphology, and localize crystals and areas for further analyses, (ii) do a rapid chemical test of the crystals synthesized in the experimental charges, and (iii) perform chemical maps to investigate the distribution of elements into the crystals and glasses.

5.2.1. Principle

SEM uses a focused beam of high-energy electrons to generate signals at the surface of conductive solid specimens. Electrons are generated by heating a tungsten filament at the top of the column (Figure 2.5) and accelerated down by high energy of 1 to 40 keV. To produce a focused beam, electrons pass through electromagnetic lenses (called condenser lenses; Figure 2.5) in a column under vacuum conditions (atmosphere is evacuated by a combination of pumps). The vacuum is necessary to avoid interaction of the electron beam with atoms naturally present in the air. The sample is mounted on a stage in the chamber area that is also under vacuum. The electron beam position on the sample is controlled by scan coils that allow the beam to scan the surface of the sample. These scan coils are situated above the objective lens (Figure 2.5).

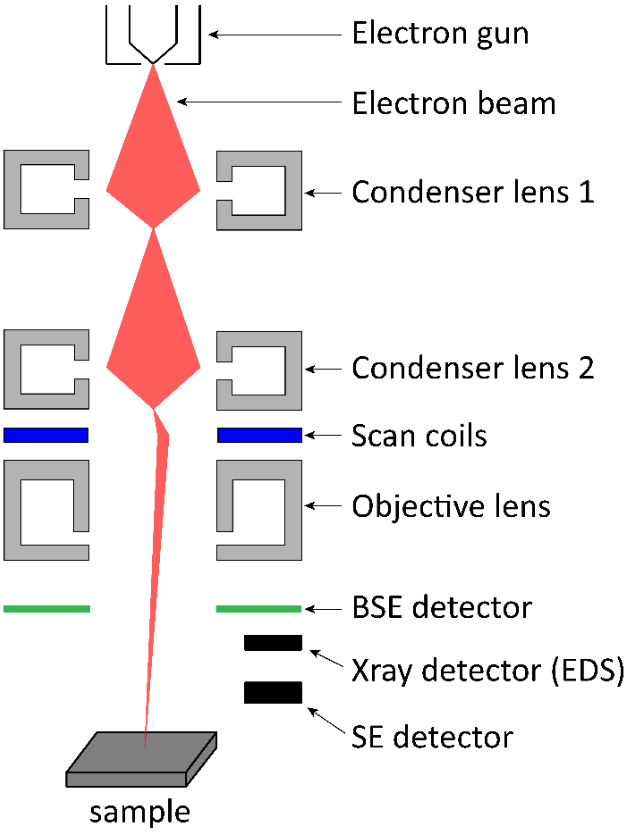
Electron gun
Electron beam
Condenser lens 1
Condenser lens 2
Scan coils
Objective lens
BSE detector
Xray detector (EDS)
SE detector
sample

Figure 2.5. *Scheme of a scanning electron microscope.*

5.2.2. SEM imaging and limits

When the electron beam hits the surface of the sample, it penetrates the sample to a depth of a few microns depending on the accelerating voltage and the density of the sample (Figure 2.6). The signal produced by the interaction electron-sample is detected by appropriate detectors: secondary electrons, back-scattered electrons (BSE), X-ray, and Auger electrons. These signals reveal a lot of information about the texture, composition, and crystalline structure of sample.

Back-scattered electrons (BSE) are produced by elastic interaction of primary electrons with the atomic nuclei of elements forming the sample. Elastic scattering will change the trajectory of the incoming electron beam when it interacts with the sample. In other words, the little particles (electrons) will collide with larger particles (atoms) in the same fashion as billiard-ball. Atoms with a larger atomic number Z have a higher probability of producing elastic collision, and therefore the number of back-scattered electrons reaching the detector depends on the atomic number. Areas composed of atoms with larger atomic number will appear "brighter", while areas composed of atoms with lower Z will appear "darker". BSE are very useful to observe intracrystalline compositional variations. However, because they only record one variable (average atomic number Z), the BSE image are limited to a grayscale range.

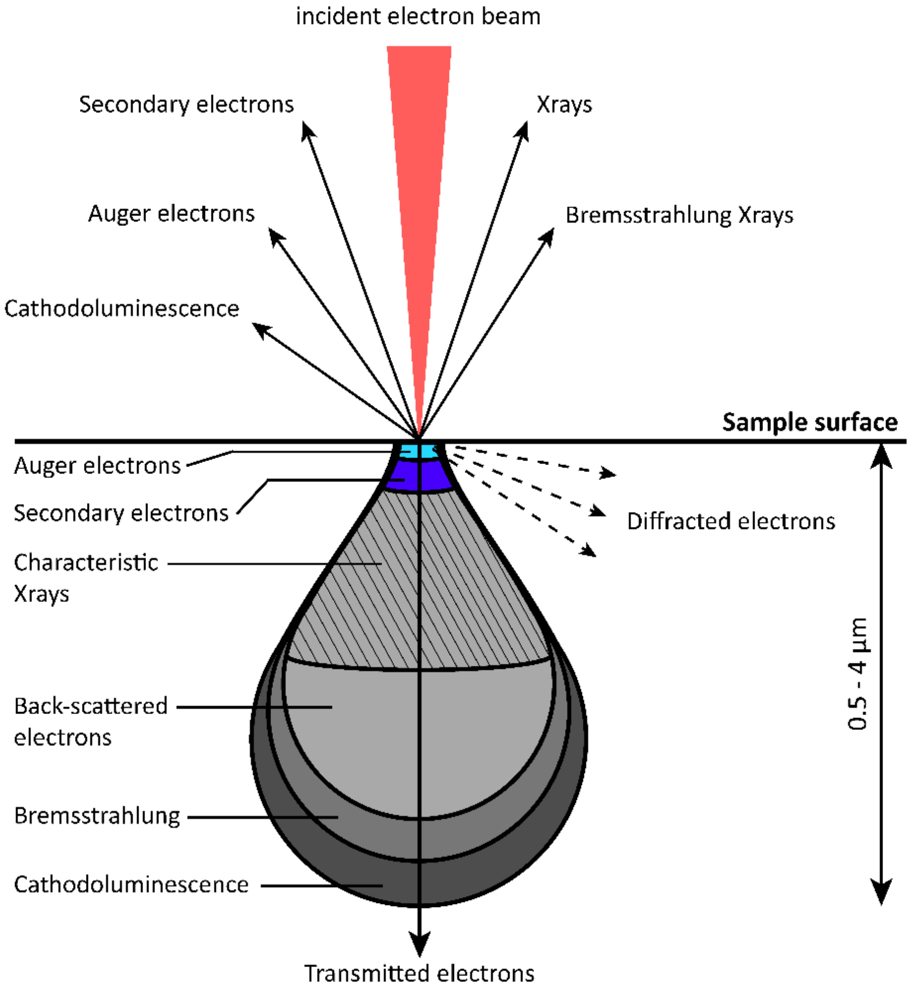
incident electron beam
Secondary electrons
Xrays
Auger electrons
Bremsstrahlung Xrays
Cathodoluminescence
Sample surface
Auger electrons
Secondary electrons
Characteristic Xrays
Diffracted electrons
0.5 - 4 µm
Back-scattered electrons
Bremsstrahlung
Cathodoluminescence
Transmitted electrons

Figure 2.6. *Scheme of the different emitted rays after interaction of an incident electron beam with a sample (over the sample surface). Electron interaction volume within a sample (under the sample surface).*

5.2.3. SEM qualitative analysis and limits

The interaction of incident electrons with the sample surface produces a diversity of signals, including X-ray. If the incident electron has a higher energy than the ionisation energy of the atom, an electron from the internal layer of the atom will detach. To regain its stability, an electron from the external layer of the atom will fill the vacancy. This phenomenon emits an X-ray photon, with an energy dependent on Z and therefore, with a very characteristic energy (and characteristic length wave). This X-ray propriety can be used for chemical analyses.

X-ray spectrum exhibits different peaks corresponding to the accumulation of X-ray photon. Peaks correspond to the jumps between the different atomic layers (Kα,β, Lα,β, etc.). The radiations can be discriminated according to their energy (Energy Dispersive X-ray Spectroscopy, EDS), or by their wavelengths (Wavelength Dispersive Spectroscopy, WDS).

When BSE is crossed with spot prob analyses (EDS and WDS) and when calibration standards are used, we can obtain qualitative analysis of the sample chemistry by chemical contrast. EDS and WDS can be used for element mapping, by rastering the element beam over an area of interest (in the same fashion as a pixel-by-pixel image but based on chemical elements). Therefore, the beam size gives the resolution, and the intensity of the signal depends on the intensity of the incident beam and on the beam dwells of the points (longer are the analysis better are the information collected). EDS maps are faster than WDS, but the resolution is lower and the detection limits higher. The spatial resolution of EDS is limited by the intensity of the source and the interaction volume of the electron with the sample. Thus, elements with low concentration may not give a response.

During EDS analysis, interferences can be recorded. These interferences are called Bremsstrahlung or “braking radiation”. They are radiations emitted by free (incident) electrons that are accelerated in the electric fields of atomic nucleus. Thus, they will emit a part of their energy as a photon of Bremsstrahlung, causing random electrostatic emissions. These emissions will generate background noise that will pollute the signal. The intensity of this radiation is dependent of the average atomic number, heavier is the element, stronger will be the radiation. However, the background noise created by these radiations can be suppressed to obtain a clean EDS spectrum.

5.2.4. SEM analytical conditions for this study

Chemical maps for Mg and Fe were collected with a Jeol-6500F FE-SEM EDS system in INGV (Rome, Italy) using 25 keV, 2.6 nA, and an acquisition time of ~3 days.

5.3. Electron Microprobe Analysis (EMPA)

5.3.1. Principle and limits

In a general way, the analytical principle of the electron microprobe is similar to that of the SEM. The technique is based on the measurement of the X-ray intensity emitted by the elements when the sample is impacted by a focused electron primary beam. However, EMP allows more precise chemical measurements than the quantitative EDS analysis of SEM. The emitted X-ray is diffracted by WD spectrometer (WDS), consisting of monochromator crystals and X-ray detector, which selects the wavelengths to analyse. These restricted selections allow better spectral resolution than EDS analysis. Quantitative analyses are performed by calibrating the spectrums through standard concentrations.

EMP allows in situ non-destructive chemical analysis of solid material polished and coated with carbon. The analytical limits of the EMP depends on the mineral measured and the elements. EMP can analyse almost all the elements, but it is unable to detect the lightest ones. Some elements can generate X-rays with overlapping peak position that must be resolved.

5.3.2. EMP analytical conditions for this study

Samples were analysed using the Jeol JXA8200 electron microprobe in INGV (Rome, Italy). Table 2.3 reports the analytical conditions used for EMP analyses of olivine following the analytical conditions of Sobolev et al., (2007) (peak analytical time and BG are different) and residual glasses following the analytical conditions of Shea et al., (2019) (peak analytical time are different) performed at INGV (Rome, Italy). Profiles were acquired for both olivine and melt, from rim to rim (or core to rim) and from interface melt (IM) to far field melt (FFM), respectively. The spot size and the step size were 2.5 µm. Two additional points were acquired for both the olivine (core and rim), and melt (IM and FFM) with a spot size of 5 µm diameter. For olivine analysis, Si, Fe, and Mg were standardized with olivine from Soppat-Kagan Valley (Kohistant, Pakistan), Na and K were standardized with orthoclase from Gothic County

(Colourado, US), Ca and P were standardized with apatite, and Ti, Al, Mn, and Cr were standardized with metals. For glass analysis, the standard used was an obsidian from Monte Pilato, Lipari.

Elements	**Crystal**		**Counting time (s)**				**Detection limit (ppm)**		**Analytical SD (%)**	
			Peak Olivine	**BG(+) Olivine**	**Peak Glass**	**BG(+) Glass**	**Olivine**	**Glass**	**Olivine**	**Glass**
		energy	20 keV		20 keV					
		intensity	300 nA		20 nA					
Si	TAP		40	20	30	15	15	72	0.05	0.17
Ti	LIF		120	60	60	30	32	46	2.20	0.80
Al	TAP		120	60	60	30	8	51	0.99	0.35
Fe	LIF		40	20	30	15	14	54	0.06	0.36
Mn	LIFH		120	60	60	30	10	53	0.44	2.84
Mg	TAPH		50	25	30	15	18	84	0.04	0.50
Ca	PETJ		120	60	30	15	11	67	0.37	0.39
Na	TAPH		120	60	15	15	12	151	5.17	0.97
K	PETJ		120	60	15	15	6	44	9.56	1.47
P	PETJ		120	60	60	30	21	131	2.28	6.75
Cr	LIFH		120	60	60	30	31	41	0.69	4.02

Table 2.3. *Electron microprobe analytical conditions for olivine crystals and glass.*

Chemical maps have also been acquired with the electron microprobe. In chapter 3, olivine and melt Mg-maps were acquired using an energy of 15 keV and an intensity of 7.5 nA. In chapter 4, olivine chemical maps of Si, Ti, Al, P, and Cr were acquired to show the chemical distribution of these elements in synthesized olivine. The energy used for these maps is 20 keV and the intensity is 300 nA.

References – Chapter 2

Di Stefano, F., Mollo, S., Scarlato, P., Nazzari, M., Bachmann, O., & Caruso, M. (2018). Olivine compositional changes in primitive magmatic skarn environments: A reassessment of divalent cation partitioning models to quantify the effect of carbonate assimilation. Lithos, 316, 104-121. doi.org/10.1016/j.lithos.2018.07.008

First, E. C., Leonhardi, T. C., & Hammer, J. E. (2020). Effects of superheating magnitude on olivine growth. Contributions to Mineralogy and Petrology, 175(2), 1-14. doi.org/10.1007/s00410-019-1638-7

Freda, C., Gaeta, M., Misiti, V., Mollo, S., Dolfi, D., & Scarlato, P. (2008). Magma–carbonate interaction: an experimental study on ultrapotassic rocks from Alban Hills (Central Italy). Lithos, 101(3-4), 397-415. doi.org/10.1016/j.lithos.2007.08.008

Garcia, M. O., Pietruszka, A. J., & Rhodes, J. M. (2003). A petrologic perspective of Kīlauea volcano's summit magma reservoir. Journal of Petrology, 44(12), 2313-2339. doi.org/10.1093/petrology/egg079

Lynn, K. J., Garcia, M. O., Shea, T., Costa, F., & Swanson, D. A. (2017). Timescales of mixing and storage for Keanakāko ‘i Tephra magmas (1500–1820 CE), Kīlauea Volcano, Hawai ‘i. Contributions to Mineralogy and Petrology, 172(9), 1-20. doi.org/10.1007/s00410-017-1395-4

Mollo, S., & Vona, A. (2014). The geochemical evolution of clinopyroxene in the Roman Province: a window on decarbonation from wall-rocks to magma. Lithos, 192, 1-7. doi.org/10.1016/j.lithos.2014.01.009

Shea, T., Hammer, J. E., Hellebrand, E., Mourey, A. J., Costa, F., First, E. C., ... & Melnik, O. (2019). Phosphorus and aluminum zoning in olivine: contrasting behaviour of two nominally incompatible trace elements. Contributions to Mineralogy and Petrology, 174(10), 1-24. doi.org/10.1007/s00410-019-1618-y

Sobolev, A.V., Hofmann, A.W., Kuzmin, D.V., Yaxley, G.M., Arndt, N.T., Chung, S.L., Danyushevsky, L.V., Elliott, T., Frey, F.A., Garcia, M.O. and Gurenko, A.A. (2007). The amount of recycled crust in sources of mantle-derived melts. science, 316(5823), 412-417. doi.org/10.1126/science. 1140516

Second part

Results

Understanding (dis)equilibrium partitioning of cations and their incorporation mechanisms in the lattice site of minerals is essential to interpret the magmatic history of rocks. Experiments performed under variable P-T-X-t conditions are important to elucidate the time-evolution of magma crystallinity and the context of magma movement through the Earth’s crust. To understand the time-evolution of crystal nucleation and growth in natural and experimental samples, it is fundamental to take in account the undercooling concept.

It is increasingly recognized that undercooling and crystallization kinetics are important processes controlling the final texture, mineral composition, and the physicochemical state of magma during ascent and emplacement. Here, I investigate the crystallization of olivine under kinetic growth conditions encountered by magmas in naturally solidifying settings. The aim is to determine, first, the magnitude of cation partitioning between olivine and melt. Deviations from chemical equilibrium develops in response to kinetically controlled cation redistributions related to the partitioning of major and trace elements between rapidly growing crystal and melt. Then, I investigate the substitution reactions of cations and the associated charge balance mechanisms controlling the entrance of these elements in the lattice of fast-growing olivine crystals.

Chapter 3

Kinetic partitioning of major and minor cations between olivine and Hawaiian tholeiitic basalt under variable undercooling and cooling rate conditions

Table of content - Chapter 3

Abstract 69

1. Introduction 70

2. Methods 72

  2.1. Experiments 72

  2.2. Analyses 74

3. Results 75

  3.1. Olivine abundance and morphology 75

  3.2. Olivine chemistry 78

  3.3. Glass chemistry 80

  3.4. Chemical maps and analytical transects 81

4. Discussion 85

  4.1. Testing for Fe^{2+}-Mg exchange between olivine and diffusive melt 85

  4.2. Olivine -melt partitioning behaviour 89

  4.3. Implication for diffusion chronometry 94

5. Concluding remarks 95

Acknowledgments 97

Supplementary Materials 98

References – Chapter 3 100

Chapter 3

Kinetic partitioning of major and minor cations between olivine and Hawaiian tholeiitic basalt under variable undercooling and cooling rate conditions

Article

Article published in *Chemical Geology* in August 2021.

Lang, Sarah[1,2], Silvio Mollo[1,3], Lydéric France[2], Valeria Misiti[3], and Manuela Nazzari[3]. "Kinetic partitioning of major-minor cations between olivine and Hawaiian tholeiitic basalt under variable undercooling and cooling rate conditions." Chemical Geology (2021): 120485.

[1]Department of Earth Sciences, Sapienza - University of Rome, P. le Aldo Moro 5, 00185 Roma, Italy

[2]Université de Lorraine, CNRS, CRPG, F-54000 Nancy, France

[3]Istituto Nazionale di Geofisica e Vulcanologia - Department Roma 1, Via di Vigna Murata 605, 00143 Roma, Italy

Abstract

In order to elucidate the kinetic partitioning of cations between olivine and basalt, we performed undercooling ($-\Delta T$) and cooling rate (*CR*) experiments at atmospheric pressure and QFM-2 buffer. Starting from the superliquidus temperature of 1,250 °C, a Hawaiian tholeiitic basalt was cooled at the rates of 4 (*CR4*), 20 (*CR20*), and 60 (*CR60*) °C/h to the final target temperatures of 1,175 °C ($-\Delta T$ = 35 °C; $-\Delta T$35) and 1,125 °C ($-\Delta T$ = 85 °C; $-\Delta T$85). Results show that polyhedral olivine morphologies are obtained at $-\Delta T$35, whereas strong disequilibrium skeletal and/or dendritic textures form at $-\Delta T$85. The amount of forsterite in olivine decreases from to 85% to 78% with increasing both $-\Delta T$ and *CR*. A diffusive boundary layer also develops in the melt next to the olivine surface and its composition becomes progressively enriched in Ca, owing to its incompatible behaviour with the lattice site. Residual melts are progressively depleted in silica and enriched in alkali from *CR4* to *CR60*, but silica-rich melts are observed with increasing $-\Delta T$. In terms of Fe^{2+}-Mg exchange, olivines obtained at $-\Delta T$35 are always in equilibrium with the diffusive boundary layer, comprising both the interface melt next to the olivine surface and the far-field melt where all chemical gradients cease. At $-\Delta T$85, however, the Fe^{2+}-Mg exchange indicates two distinct equilibration stages between olivine core and far-field melt, and between olivine rim and interface melt. Partition coefficients (Kd) of Mg, Fe, Mn, Ca, and Cr calculated at the olivine-melt interface preferentially change as a function of $-\Delta T$ rather than *CR*. From $-\Delta T35$ to $-\Delta T85$, Kd$_{Mg}$, Kd$_{Fe}$, Kd$_{Mn}$, and Kd$_{Cr}$ remarkably increase, whereas the opposite applies to Kd$_{Ca}$. Through the application of equilibrium partitioning models, we found that Mg, Fe, Mn, and Ca are incorporated into the olivine lattice site at near-equilibrium proportions. This generally good agreement with modeling data demonstrates that diffusive mass transport of cations in our experiments occurred under the conditions of local equilibrium at the olivine surface. In contrast, marked deviations from the expected equilibrium are found for K$_{Cr}$ in response to the major influence of crystal field stabilization energy on cation incorporation.

Keywords: olivine kinetic growth; cation partitioning; tholeiitic basalt; undercooling and cooling rate.

1. Introduction

Olivine is one of the most common mineral phases in naturally cooled basaltic systems. Its composition in major and minor elements is widely used to discuss magma genesis and evolution, or to quantify igneous processes and their kinetics, in studies that usually consider equilibrium-based partitioning rules (e.g., Moore, 1988; Perfit et al., 1996; Sobolev et al., 2007; Foley et al., 2013). During the last decades, a gamut of studies has documented that both textural and compositional changes of olivine are not necessarily related to the attainment of equilibrium. As documented in literature (e.g., Hammer, 2006, 2008; Koepke et al., 2011; Vetere et al., 2013; First and Hammer, 2016; Mollo and Hammer, 2017; First et al., 2020), most of the solidification path of basaltic magmas is governed by the interplay between undercooling (i.e., $-\Delta T = T_{liquidus} - T_{final}$, where T is temperature) and cooling rate (i.e., $CR = -\Delta T/t$, where t is time).

In his early experimental work, Donaldson (1976) categorized ten different types of olivine morphologies as a function of $-\Delta T$ and CR, involving changes from equant habit to elongated bladed habit to tabular habit. Afterwards, Faure et al. (2003, 2007) documented that the olivine morphology evolves from polyhedral/tablet to hopper/skeletal and finally to dendrite with increasing $-\Delta T$ (0-1850 °C) and CR (0-350 °C/h) due to competition between the dendrites and parent hopper crystals. As a general rule, small $-\Delta T$ are associated with the formation of polyhedral olivine via interface-controlled growth regimes, where the diffusion of chemical species in the melt is fast enough with respect to crystal growth rates and allows interface melt equilibration with far field melt upon grain growth. In contrast, large $-\Delta T$ promote diffusion-controlled growth processes, where the crystal growth rate exceeds the ability of chemical elements to diffuse through the melt. This disparity leads to the disequilibrium crystallization of hopper to skeletal and then to dendritic morphologies, as observed by Faure et al. (2003, 2007). However, at very low CR, a large $-\Delta T$ might also have little effect over a very long period of time (i.e., relaxation time), suggesting that $-\Delta T$ and CR (i.e., cooling time) are intrinsically interrelated and exercise a combined control on olivine morphology. Rapidly growing olivine crystals are also chemically zoned due to the formation of a diffusive boundary layer in the melt, from which incompatible components are directly incorporated in the lattice site (Grant and Kohn, 2013; Welsch et al., 2013, 2014; Shea et al., 2019).

The control of $-\Delta T$ and CR on the olivine composition, and potentially on the partition coefficients is focal to correctly decipher the solidification path of basaltic magmas. Owing to its simple neso-silicate structure, olivine nucleates and grows very readily once the saturation temperature has been reached, thereby depleting the melt in some important components (i.e., Mg and Fe) essential for the geochemical evolution of mafic systems (Corrigan, 1982). There is general consensus that strong kinetic effects may substantially change the olivine chemistry by superimposition of diffusion-limited reactions between the interface melt and advancing crystal surface (e.g., Grove and Raudsepp, 1978; Kennedy et al., 1993; Sossi and O'Neill, 2016; Shea et al., 2019). However, in what may be an emerging paradigm, several authors have documented that the Fe^{2+}-Mg exchange between olivines and basaltic melts (i.e., lunar basalt, eucrite basalt, andesitic basalt, basaltic andesite, and trachybasalt) does not substantially change under disequilibrium crystallization conditions (i.e., *CR* = 0.5-2000 °C/h), showing values comparable to those calculated through phase equilibrium experiments (Walker et al., 1976; Powell et al., 1980; Kring and McKay, 1984; Baker and Grove, 1985; Conte et al., 2006). Similarly, the partitioning of Ca between olivine and silicate melt has been found to be independent of *CR* for experiments carried out on extraterrestrial compositions cooled at highly variable rates of 1-2193 °C/h (Kennedy et al., 1993) and 1.5-1000 °C/h (Pack and Palme, 2003).

In view of the close correspondence between equilibrium and disequilibrium partition coefficients, we have investigated the partitioning behaviour of major (i.e., Mg and Fe) and minor (i.e., Mn, Ni, Cr, and Ca) cations between olivine and a Hawaiian tholeiitic basalt under variable $-\Delta T$ and *CR*. The aim of this work is to quantify the sign and magnitude of cation partitioning when the crystallization olivine is controlled by kinetic growth conditions encountered by magmas in naturally solidifying settings (e.g., Ujike, 1982; Hammer, 2008; Mollo et al., 2011; Vetere et al., 2015; Giuliani et al., 2020). Our results illustrate that $-\Delta T$ and *CR* exercise different effects on olivine morphology and major-minor cation partitioning. Although chemical elements are heterogeneously distributed in the olivine and surrounding melt, diffusive mass transport with local equilibrium at the crystal-melt interface is the most likely rate-controlling process established at the onset of olivine nucleation. Exceptions to this near-equilibrium incorporation mechanism result from the interplay between cation structural properties and their diffusivities in the melt feeding olivine growth.

2. Methods

2.1. Experiments

The starting material object of this study is a tholeiitic basalt (i.e., highly vesicular pumice) from the 1820 CE eruption of Kilauea (Garcia et al., 2003; Lynn et al., 2017; Shea et al., 2019). The powdered natural rock was loaded in a Fe-presaturated Pt-crucible and then melted at 1 atm and 1500 °C for 1 h using a Nabertherm $MoSi_2$ chamber furnace. Then, the melt was instantaneously quenched in water, in order to prevent crystallization. Iron loss was also minimized during the synthesis by adding iron oxalate (~4 wt.% FeO) to the starting composition, as previously quantified for primitive eruptive products (e.g., Freda et al., 2008). The final composition of the mixture used for the experiments is 47.92 wt.% SiO_2, 2.21 wt.% TiO_2, 11.80 wt.% Al_2O_3, 14.62 FeO_t (expressed as total iron), 0.18 wt.% MnO, 11.10 wt.% MgO, 9.46 wt.% CaO, 1.83 wt.% Na_2O, 0.40 wt.% K_2O, 0.22 wt.% P_2O_5, and 0.21 wt.% Cr_2O_3. The resulting glass was crushed with an agate mortar to obtain a fine-grained glassy powder. Experimental charges were prepared by mixing the glassy powder with polyvinyl alcohol. This mixture was shaped into spheres with diameter of 1.5 mm (~45 milligrams of material) that were surrounded by a Fe-presaturated Pt-wire loop with thickness of 0.1 mm. The use of Fe-presaturated Pt-wire was preferred to Re-wire in order to avoid Ni loss (i.e., Ni may alloy with the Re metal wire; First et al., 2020). The experiments were performed at the HP-HT Laboratory of Experimental Volcanology and Geophysics of the Istituto Nazionale di Geofisica e Vulcanologia (INGV), Rome, Italy, in a 1 atm vertical tube CO-CO_2 gas-mixing furnace (Nabertherm Furnace RHTV 120-300/18) at the QFM-2 buffer. The oxygen fugacity was monitored and maintained constant by an Yttria-doped-zirconia solid electrolyte oxygen sensor ($SIRO_2$, Ceramic Oxide Fabricators, Ltd., Australia) and two digital thermal mass flow meters for CO and CO_2 controlled via software. Temperature was measured by a Pt-$Pt_{90}Rh_{10}$ thermocouple, with uncertainty of ±3 °C, which was located within 1 cm of the sample chandelier holding the experimental charges. The liquidus temperature was estimated at 1210 °C, in agreement with the presence of a few tiny olivine crystals. A superliquidus treatment at 1250 °C (i.e., only 40 °C above the liquidus state of the melt) was adopted by keeping the temperature constant for a relative short time of 1 h (Figure. 3.1 and Table 3.1). These *T-t* conditions were selected to minimize the effect of superheating magnitude on olivine growth (First et al., 2020). Then, the charges were cooled at the rates of 4 (*CR4*), 20 (*CR20*), and 60 (*CR60*) °C/h to the final target temperatures of 1175 °C ($-\Delta T$ = 35 °C; $-\Delta T$35) and 1125 °C (-

ΔT = 85 °C; -*ΔT*85). The experiments were fast quenched by dropping the chandelier into a water bath and recovered run products were mounted in epoxy and polished for analyses. The quenching efficiency is highlighted by the lack of quench-phases crystallization (Figure. 3.2)

-ΔT	CR	P	*f*O₂	Mg#	Glass	Olivine [(1)]	G_{max} (2D) [(2)]	G_{max} (MB) [(3)]
(°C)	(°C/h)	(MPa)	(Buffer)	(melt)	(wt.%)	(wt.%)	(m/s)	(m/s)
35	4	0.1	QFM-2	62.75	89.4	10.6	1.4E-09	6.2×10^{-10}
35	20	0.1	QFM-2	52.84	89.6	10.4	2.5E-09	1.7×10^{-9}
35	60	0.1	QFM-2	52.03	88.4	11.6	5.2E-09	2.8×10^{-9}
85	4	0.1	QFM-2	55.76	88.0	12.0	6.7E-09	4.6×10^{-9}
85	20	0.1	QFM-2	56.30	85.5	14.5	2.3E-08	1.3×10^{-8}
85	60	0.1	QFM-2	50.22	85.8	14.2	4.7E-08	3.5×10^{-8}

(1)
$$Ol_{content}(wt.\%) = \sum_{1}^{n}\left(\frac{MgO^{starting\ material} - MgO^{residual\ glass}}{MgO^{olivine} - MgO^{residual\ glass}} \times 100\right)/n$$

n = number of crystals tested

(2)
$$G_{max} = \frac{\sqrt[3]{Ol_{content}/100 \times \left(\frac{4}{3}\pi r^3\right) \times \frac{3}{4\pi}}}{t_{exp} \times 10^6}$$

$Ol_{content}$ = Eqn. (1); r = crystal radius; t_{exp} = experimental duration (sec)

(3)
$$G_{max} = \frac{(W \times L)^{0.5}}{2 \times t_{exp}}$$

W = width (m); L = length (m); t_{exp} = experimental duration (sec)

Table 3.1. *Experimental conditions, phase relations, and olivine growth rates.*

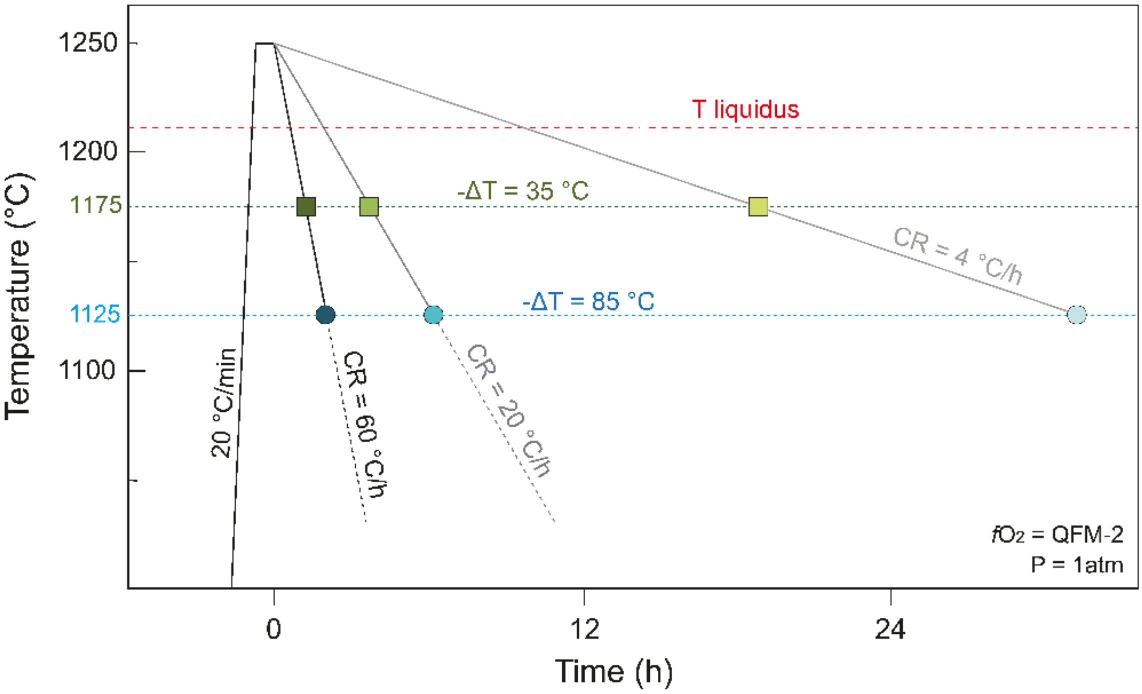

Figure 3.1. *Temperature versus time diagram illustrating the experimental strategy employed for the experiments studied herein.*

2.2. Analyses

The experiments were analysed for olivine and glass compositions (Supplementary Material 1) with a Jeol-JXA8200 electron microprobe (EDS-WDS combined analytical system) equipped with five wavelength-dispersive spectrometers at the HP-HT Lab of INGV. Element profiles for major (Fe, Mg, and Si), minor (Ca, Mn, and Ti), and trace (Cr) elements were acquired within olivine using an accelerating voltage of 20 keV, and a 300 nA beam current (following Sobolev et al., 2007), both spot and step sizes of 2.5 µm. Two additional analyses were acquired for each crystal at core and rim close to the glass interface, using analogous analytical conditions but spot size of 5 µm. Counting times were 40 (Si and Fe), 50 (Mg), and 120 (Mn, Ca, and Cr) seconds, also with half the peak times on the background (see Supplementary Material 1 for further details). Transects were collected in the glass adjacent to the olivine interface, in order to quantify the boundary layer composition and its extent. For glass analyses, the accelerating voltage and current were 20 keV and a 20 nA (Shea et al., 2019), as well as both spot and step sizes were 2.5 µm. As for olivine crystals, two additional analyses were collected for each transect (close and far from the olivine interface), using a spot size of 5 µm. Counting times were 15 (Na and K), 30 (Si, Fe, Mg, and Ca), and 60 (Ti, Al, Mn, and Cr) seconds, also with half of the peak times on the background. Mineral and glass standards were used for the calibration, including olivine from Soppat Naran-Kagan Valley (Kohistan, Pakistan) for Si, Fe, and Mg, apatite for Ca and P, orthoclase from Gothic County (Colourado, US) for Na and K, and metals for Ti, Al, Mn, and Cr. The precision of the microprobe was measured through the analysis of well characterized standards. Based on counting statistics, analytical uncertainties relative to their reported concentrations indicate that accuracy was better than 5% for all cations except for elements with abundances below 1 wt.%, for which accuracy was better than 10%. Precision was typically better than 1–5% for all analyzed elements. Chemical maps for Mg were acquired with microprobe using 15 keV and 7.5 nA. Conversely, chemical maps for Mg and Fe were collected with a Jeol-6500F FE-SEM EDS system using 25 keV, 2.6 nA, and acquisition time of ~3 days.

3. Results

3.1. Olivine abundance and morphology

The experimental charges are characterized by the ubiquitous presence of olivine surrounded by abundant glass. No other mineral phases are found, with the exception of very tiny oxides observable only at the micrometric to submicrometric scale. The amount of olivine from experiments has been quantified through the mass balance equation proposed by Mourey and Shea (2019), suggesting that the degree of crystallization slightly increases from ~11-12 to ~12-14 wt.% with increasing both -*ΔT* and *CR* (see Table 3.1 for details). This restricted range suggests that, over the experimental conditions investigated here, the final crystalline mass attained a putative equilibrium state, with minimum effects due to delay nucleation and lag time. Accordingly, thermodynamic simulations carried out with rhyolite-MELTS (v.1.1.0; Gualda et al., 2012) at the same conditions of the experiments confirm that the equilibrium olivine content is ~10-14 wt.% within a temperature range of 1125-1175 °C.

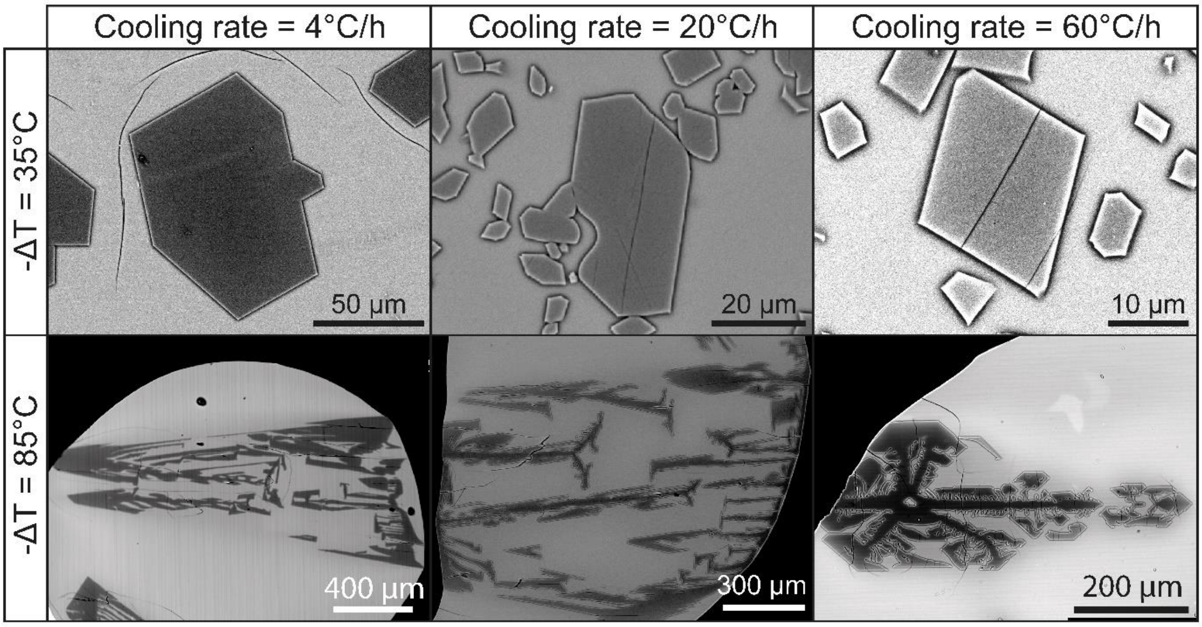

Figure 3.2. *BSE (back-scattered electron) photomicrographs of experimental olivines showing the morphology and the size of the crystals obtained under the different cooling rate and undercooling. From left to right: CR4, CR20, and CR60. From top to bottom: olivine crystals obtained under -ΔT35 and -ΔT85.*

The morphological evolution of olivine has been categorized using the terminology introduced by Donaldson (1976) and Faure et al. (2003, 2007) for crystals obtained under increasing degrees of $-\Delta T$. According to those authors, well-faced olivines with polyhedral morphologies develop at $-\Delta T$ of ~10–40 °C, whilst hopper cavities and/or skeletal to dendritic branching typically occur at $-\Delta T$ of ~40–350 °C. The transition between these different growth mechanisms depends on the efficiency of melt relaxation phenomena (Faure et al., 2007 and references therein). Additionally, in the synthetic CMAS system, there is a trade-off between $-\Delta T$ and *CR*, such that only polyhedral olivines develops at $-\Delta T \leq 116$ °C and $CR < 47$ °C/h (Faure et al., 2003). At $CR \geq 47$ °C/h, the evolution of olivine morphology depends only on the magnitude of $-\Delta T$, whereas *CR* appears to affect the crystal size and the transition temperature between the different crystalline forms (Faure et al., 2003). Figure. 3.2 shows BSE photomicrographs of olivines from this study. Euhedrality and polyhedral morphologies are obtained at small undercooling ($-\Delta T35$) and this textural feature does not change with increasing *CR*. This applies explicitly to the *CR* conditions investigated here for a natural basaltic composition, and the small $-\Delta T$ selected for this experimental batch. At large undercooling ($-\Delta T85$), the olivine texture evolves towards strong disequilibrium shapes, also with the contribution of *CR*. At *CR4* and *CR20* a few large crystals develop showing skeletal morphologies and melt infilling (Figs. 3.2 and 3.3a). At *CR60*, the experimental charge consists of either skeletal or dendritic shapes (Figure. 3.2 and 3.3b). Overall, the degree of undercooling exercises a stronger impact on the crystal texture relative to the magnitude of cooling rate and cooling time, as previously observed for the morphological evolution of olivine in mafic systems (Faure et al., 2003; Welsch et al., 2013).

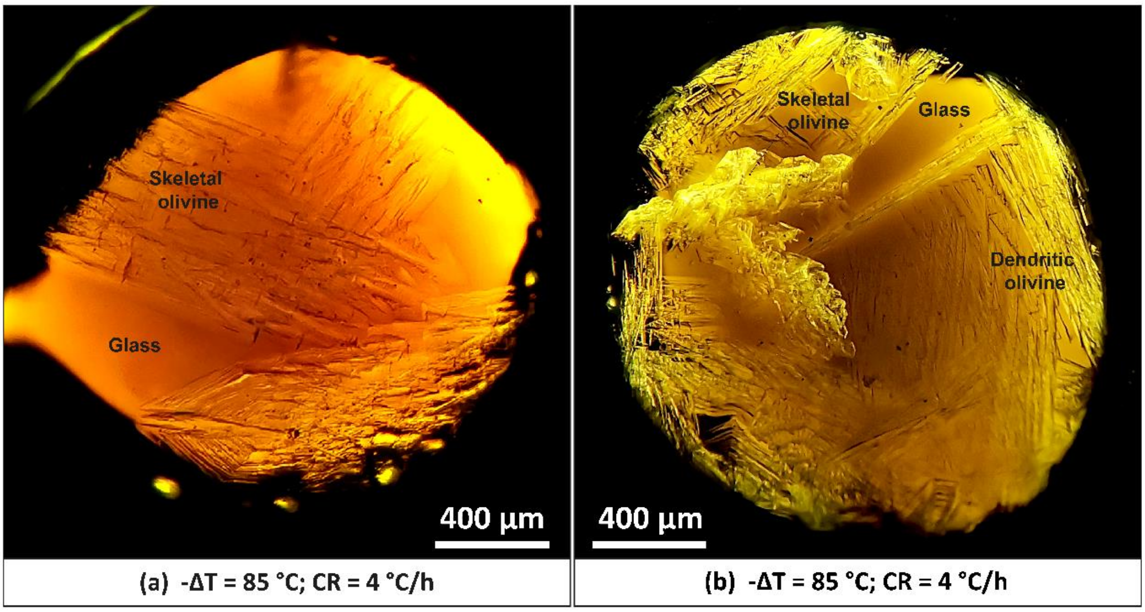

Figure 3.3. *Transmitted light photomicrographs of experimental charges obtained at undercooling condition of 85 °C and cooling rate of 4 °C/h (a) and 60 °C/h (b).*

The maximum crystal length of olivine increases from ≤5 to 150 μm (–*ΔT35*) and from 250 to 1660 μm (–*ΔT85*) with decreasing *CR* (Figure. 3.2). Generally, larger sizes are measured at –*ΔT85*. The maximum growth rate (G_{max}) has been quantified by employing two different equations reported in Table 3.1 and based on mass balance modeling (Mourey and Shea, 2019) and 2D estimations of crystal size (Hammer and Rutherford, 2002). Figure. 3.4 shows that G_{max} monotonically increases with increasing –*ΔT,* also in accord with previous data from Jambon et al. (1992) and Mourey and Shea (2019). Notably, G_{max} also increases of one order of magnitude as *CR* increases from 4 to 60 °C/min (Figure. 3.4), thus illustrating the important role played by time-dependent pathways on the olivine growth, and the formation of numerous crystals dispersed in abundant glass (Figs. 3.2 and 3.3).

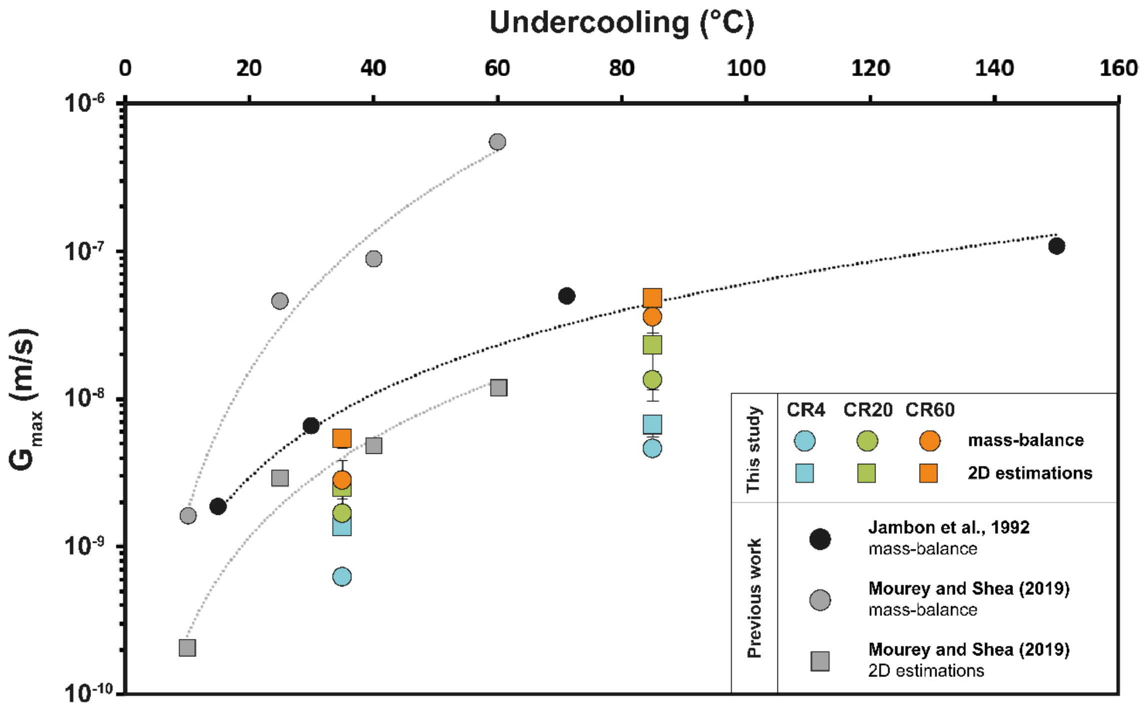

Figure 3.4. *Maximum olivine growth rate (G_{max}) versus undercooling calculated by mass-balance estimation (circles) and 2D estimation (squares) for both undercooling* $-\Delta T35$ *and* $-\Delta T85$*, and for CR4 (blue), CR20 (green) and CR60 (orange). Data from this study are compared with 2D and mass-balance estimations from Jambon et al. (1992) and Mourey and Shea (2019).*

3.2. Olivine chemistry

Olivine average compositions (core + rim) are expressed as atoms per formula unit (apfu) recalculated on the basis of 4 oxygens. As expected for the olivine stoichiometry, Mg and Fe^{2+} major cations show antithetical variations and, for simplicity, only magnesium changes will be presented herein.

Mg defines a continuous declining trajectory with increasing *CR* at $-\Delta T35$ (Figure. 3.5a). Conversely, Mg decreases from *CR4* to *CR20* at $-\Delta T85$, thereby attaining a plateau concentration between *CR20* and *CR60*. The amount of Mg measured at $-\Delta T85$ is also statistically higher than that found at $-\Delta T35$, with overlapping concentrations at *CR20* (Figure. 3.5a). Differently from Mg, the amount of Ca measured at $-\Delta T35$ is higher than that analysed at $-\Delta T85$ (Figure. 3.5b). Marked changes are measured between *CR4* and *CR20*, whereas no clear variations are resolved between *CR20* and *CR60* (Figure. 3.5b). Mn analyses are scattered between *CR20* and *CR60* at *–ΔT85* °C (Figure. 3.5c), as well as no defined trends are found with increasing *CR*. At *CR4*, the amount of Mn increases as *–ΔT* increases from 35 to 85 °C (Figure. 3.5c). The distribution of Cr in olivine is opposite to that observed for Ca. At *–ΔT35*, Cr contents are lower than those found at *–ΔT85* (Figure. 3.5e). Major changes are measured between *CR4* and *CR20*, whereas no defined trends are depicted between *CR20* and *CR60* (Figure. 3.5e). As a general rule, experimental olivine compositions obtained at *CR4* better reproduce those derived by MELTS thermodynamic simulations, suggesting that the cooling time is enough long to facilitate the attainment of near-equilibrium crystallization (Figure. 3.5).

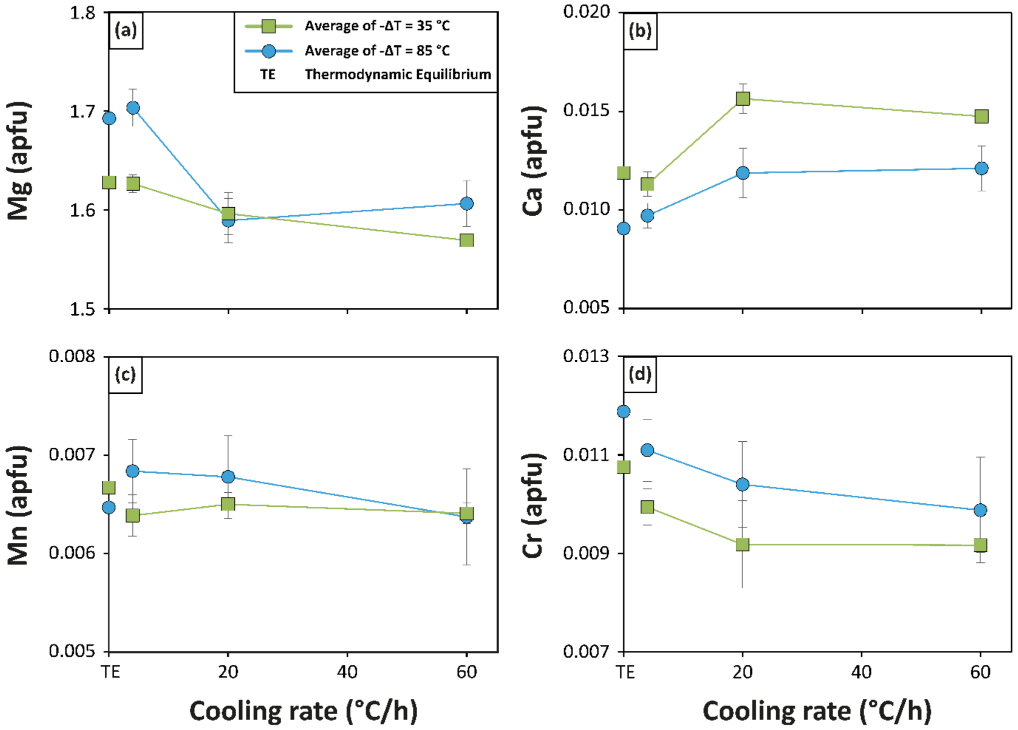

Figure 3.5. *Olivine cation concentrations in atom per formula unit versus cooling rate. Data are plotted for undercooling conditions of 35 (green square) and 85 °C (blue circle).*

Olivine components are determined through a four end-member-based solution model for forsterite (Fo; Mg_2SiO_4), fayalite (Fa; Fe_2SiO_4), calcio-olivine (Ca-ol; Ca_2SiO_4), and tephroite (Teph; Mn_2SiO_4). Olivine components change as a function of *–ΔT* and *CR*, paralleling the concentration of major cations. Fo decreases from 84.9 ± 0.5% to 78.6 ± 0.2% with increasing *CR* (Figure. 3.6a), in agreement with previous cooling experiments that show the same compositional change (Sossi et O'Neill., 2016). At *–ΔT* = 85 °C, a plateau effect around Fo_{80}

is also attained from *CR20* to *CR60*. Two distinct trends are depicted by Ca-ol as a function of *–ΔT*, with more marked variations measured from *CR4* to *CR20* (Figure. 3.6b). Considering the analytical uncertainty, the effect of *CR* on Teph is not appreciable and only little compositional differences can be resolved with increasing *–ΔT* (Figure. 3.6c). As for the case of single Mg, Ca, and Mn cations, thermodynamic olivine components derived by MELTS closely resemble those obtained at *CR4*.

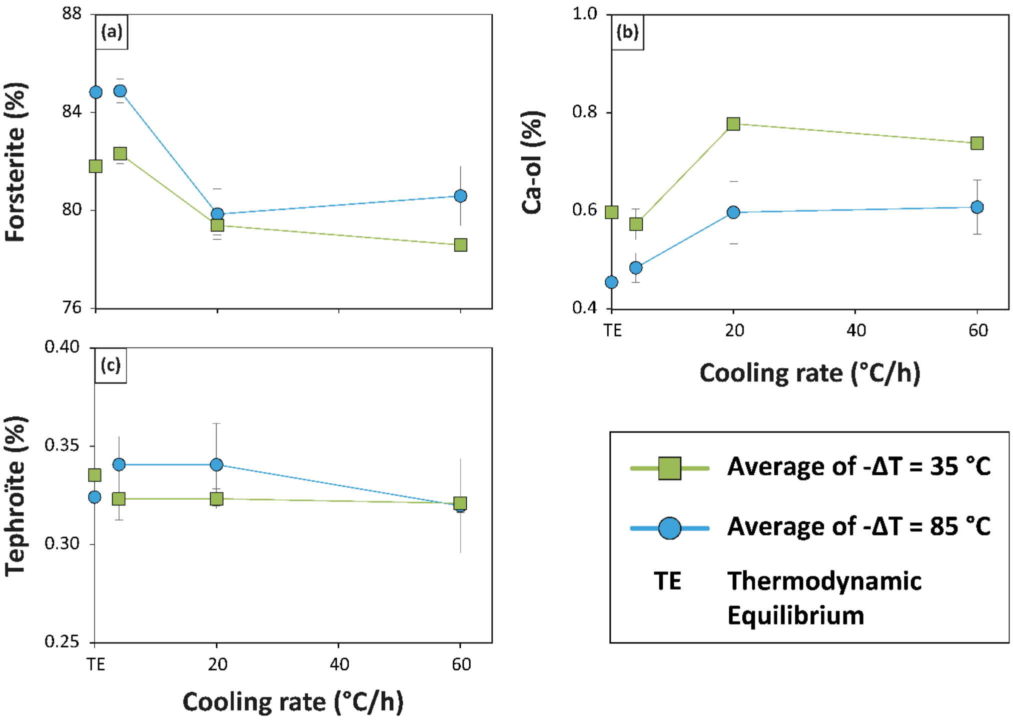

Figure 3.6. *(a) Forsterite, (b) Ca-ol, and (c) tephroite in olivine versus cooling rate. Data are plotted for undercooling conditions of 35 (green square) and 85 °C (blue circle).*

3.3. Glass chemistry

Figure. 3.7a shows the starting tholeiitic basalt and residual glass compositions plotted in the total alkali vs. silica diagram (TAS; Le Bas et al., 1986). As *CR* increases from 4 to 60 °C/h, SiO_2 decreases and Na_2O + K_2O increases. The glass chemistry clusters at low-SiO_2 (~48.0-50.5 wt.%) and high-SiO_2 (~49.5-53.3 wt.%) contents at *–ΔT35* and *–ΔT85*, respectively. Most of the experimental glasses are classified as basalts, with the exception of some basaltic andesitic data obtained at *–ΔT85* and *CR4* (Figure. 3.7a).

Figure. 3.7b shows that the average value of $^{melt}Mg\#$ [Mg-number of melt = Mg / (Mg + Fe_t) × 100 on molar basis)] decreases from ~57 to ~53 (*–ΔT35*) and from ~64 to ~53 (*–ΔT85*) with increasing *CR*. It is worth stressing that the two evolutionary paths produce more differentiated glass compositions, also in agreement with the increasing olivine content estimated by mass balance calculations (Table 3.1). However, residual glasses at CR4 from *–ΔT35* and *–ΔT85* form two distinct populations characterized by $^{melt}Mg\#_{57}$ and $^{melt}Mg\#_{64}$, respectively. Conversely, compositional data overlap for $^{melt}Mg\#_{53\text{-}57}$ and $^{melt}Mg\#_{50\text{-}55}$ for *CR20* and *CR60*, respectively (Figure. 3.7b).

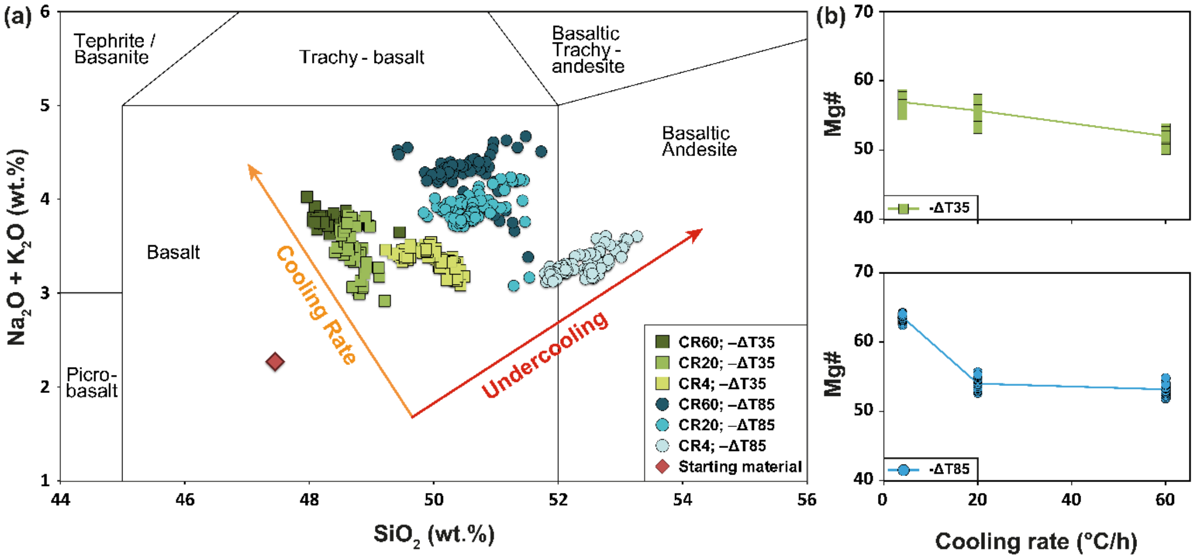

Figure 3.7. *(a) Glass compositional change plotted in the TAS (total alkali versus silica) diagram for both -ΔT35 (green square) and -ΔT85 (blue circle), as well as for CR4 (light shade), CR20 (medium shade), and CR60 (dark shade). This diagram shows silica content decrease with increasing cooling rate and decreasing undercooling. (b) Mg# versus cooling rate diagram for both -ΔT35 (green square) and -ΔT85 (blue circle). The major changes occur under the effect of the cooling rate, as Mg# decrease with decreasing cooling rate from 4 to 60 °C/h. Error bars are not observable as they are smaller than the symbols.*

3.4. Chemical maps and analytical transects

X-ray electron microprobe maps for *–ΔT35* experiments are displayed in Figure. 3.8. MgO maps have been exported using two different colour scales, in order to better highlight either compositional gradients in the glass (Figure. 3.8a) or intracrystalline variations in olivine

(Figure. 3.8b). As *CR* increases from 4 to 20 to 60 °C/h, the thickness of the Mg diffusive boundary layer in the melt increases from ~3 to ~6 to ~12 µm (Figure. 3.8a), respectively. Chemical gradients in the melt feeding olivine growth are enhanced by the effect of *CR* due to stronger supersaturation phenomena (Lu et al., 1995). At ~4 °C/h, gentle MgO chemical gradients develop in the melt, whereas stronger depletion effects are observed at 60 °C/h. Textural and compositional features of olivine reflect the role played by melt relaxation kinetics on the crystal growth (Figure. 3.8b). As *CR* increases, a greater number of tiny, MgO-poor olivines form in response to more efficient nucleation kinetics and diffusion fields surrounding the crystals (compare Figs. 3.8a and 3.8b). However, the crystal morphology remains well-faced at –*ΔT35* (Figure. 3.8b), highlighting that olivine euhedrality is principally controlled by low degrees of undercooling rather than variable cooling rates.

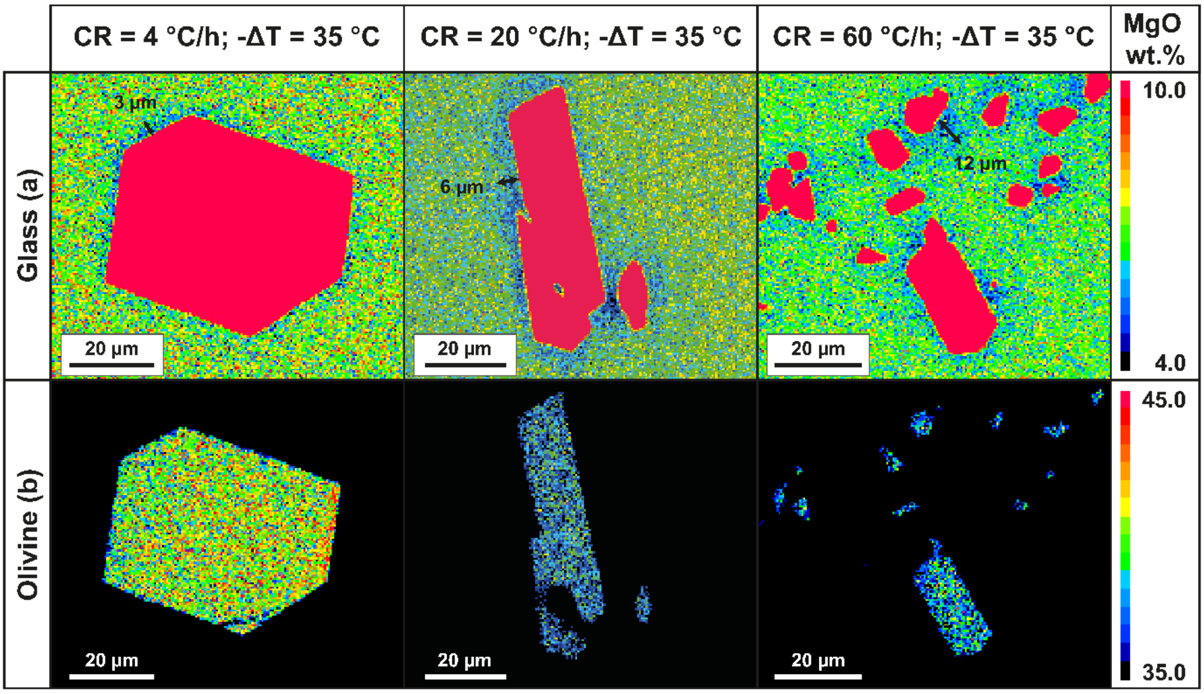

Figure 3.8. *X-ray electron microprobe maps of (a) glass and (b) olivine at undercooling condition of 35 °C.*

BSE imaging and X-ray mapping for –*ΔT85* experiments are displayed in Figure. 3.9. A combined two-band photomicrograph is obtained by assigning blue and yellow composite colours to the single-band maps of MgO and FeO, respectively. Strong chemical gradients develop in the glass surrounding skeletal and dendritic olivines, showing maximum thickness of ~120 μm (Figure. 3.9), which is one order of magnitude greater than that measured at $-\Delta T35$. As a consequence, the melt next to olivine surface is dramatically depleted in MgO at *CR* comprised between 4 and 60 °C/h (Figure. 3.9). Since multiple olivine branches develop contemporaneously over the effect of *CR*, the diffusion fields around individual crystals may also overlap with one another, thereby enhancing MgO depletion at the interface melt. Notably, for cations with the same order of relative compatibility in olivine (i.e., Mg and Cr), the overall variability of the melt diffusive boundary layer is 11% and 24% for the fast-diffusing Mg and slow-diffusing Cr cations, respectively. However, in the melts surrounding olivine crystals, no clear changes are observed as a function of $-\Delta T$ and *CR*, due to impingement of distinct diffusion fields of nearby olivine crystals.

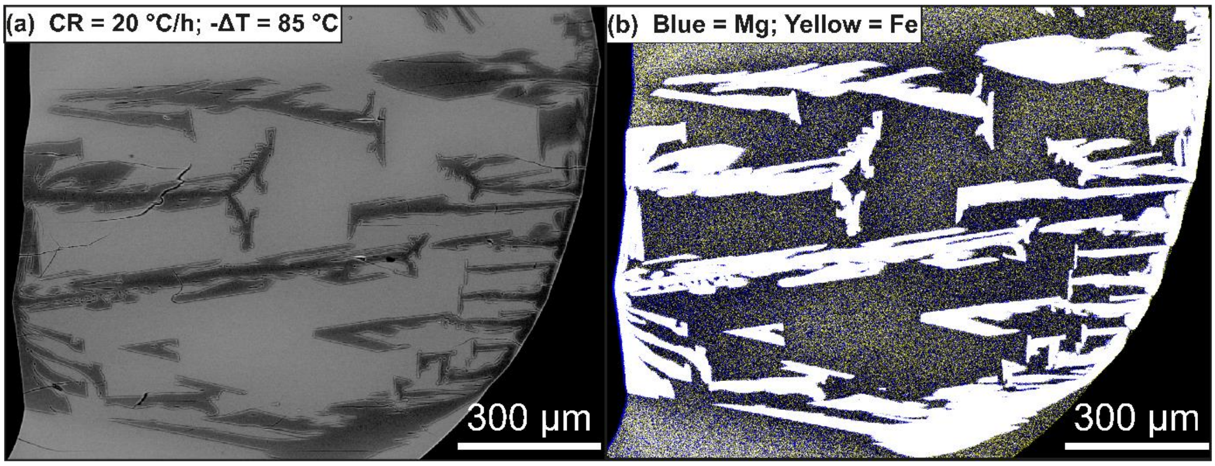

Figure 3.9. *(a) BSE (back-scattered electron) image for the experimental charge obtained at undercooling condition of 85 °C and cooling rate of 20 °C/h. (b) X-ray map of the same sample with colour scale adjusted for the glass, showing depletion in iron and magnesium around the olivine crystal.*

Figure. 3.10 shows the chemical distribution of cations from rim to core of olivine crystals. Microprobe transects refer to $-\Delta T35$ and $-\Delta T85$ experiments performed at both *CR4* and *CR60*. It is found that Mg increases from rim to core, whereas Fe, Ca, and Mn decrease. Dividing the cation concentration at the core by that at the rim, we have calculated the average enrichment (ε) and depletion (δ) factors. Results return $^{-\Delta T35}\delta_{Mg}$ and $^{-\Delta T85}\delta_{Mg}$ of ~2% and ~6%, respectively. $^{-\Delta T35}\varepsilon_{Ca}$, $^{-\Delta T35}\varepsilon_{Mn}$, and $^{-\Delta T35}\varepsilon_{Fe}$ are ~25%, ~13%, and 6%, respectively, whereas $^{-\Delta T85}\varepsilon_{Ca}$, $^{-\Delta T85}\varepsilon_{Mn}$, and $^{-\Delta T85}\varepsilon_{Fe}$ are ~42%, ~26%, and 20%, respectively. It is worth noting that the magnitude of ε

decreases in the order Ca > Mn > Fe, thus reflecting the different cation diffusivities in the melt (e.g., Zhang et al., 2010). Higher ε and δ values are measured at *–ΔT85*, in agreement with stronger supersaturation conditions resulting from larger degrees of undercooling. Finally, we emphasize that intra-crystal cation distributions in olivines are completely independent of their textures, showing chemical zonation for both well-faced polyhedral crystals and skeletal-to-dendritic shapes. In this latter case, however, major crystal zoning is systematically observed at *–ΔT85* and *CR60*.

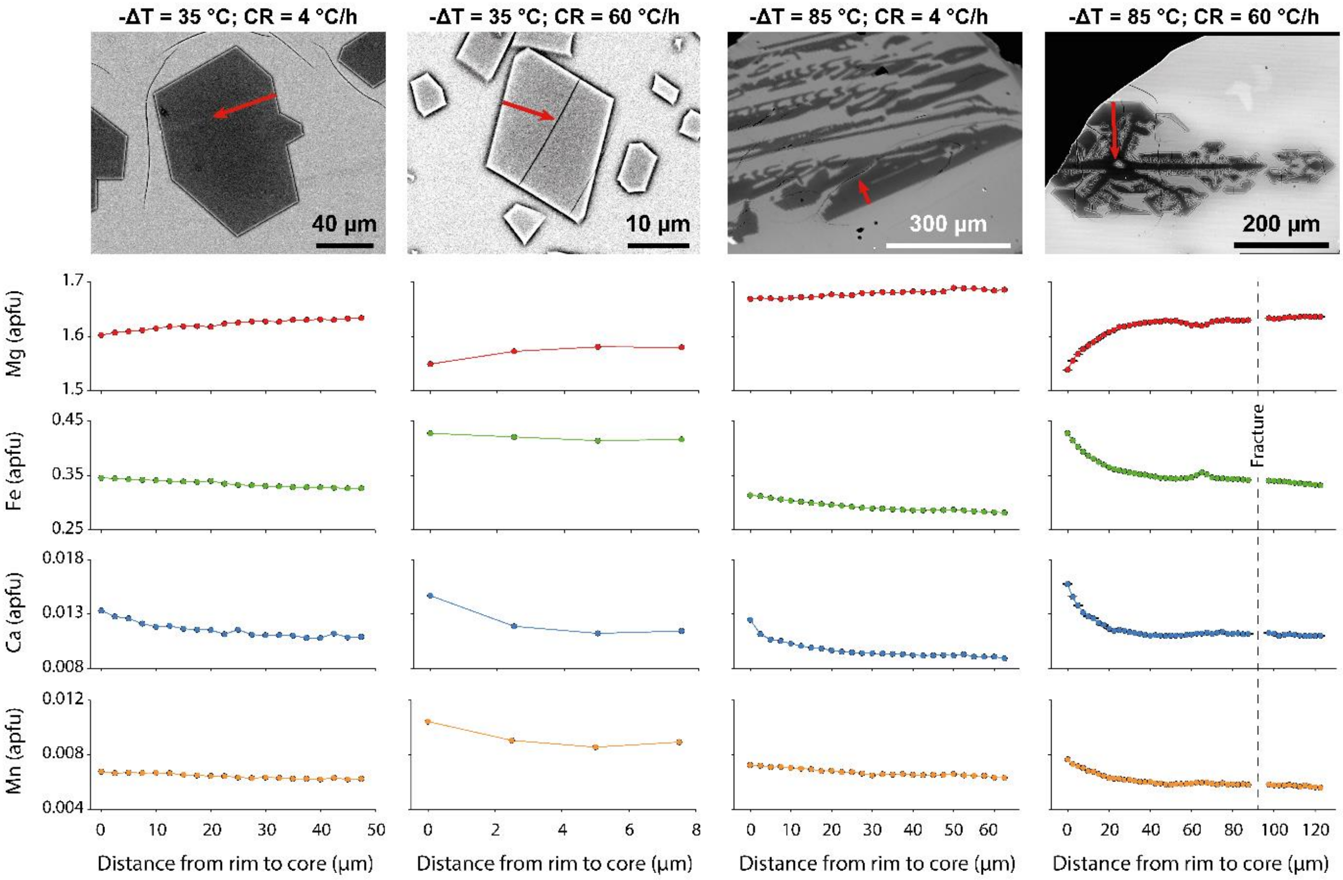

Figure 3.10. *Chemical distribution of Mg, Fe, Ca, and Mn cations from rim to core of olivine crystals. Microprobe transects refer to undercooling conditions of 35 and 85 °C and cooling rates of 4 and 60 °C/h.*

4. DISCUSSION

4.1. Testing for Fe^{2+}-Mg exchange between olivine and diffusive melt

Roeder and Emslie (1970) argued that the equilibrium Fe^{2+}-Mg exchange between olivine and melt is expressed as:

$$Kd_{ol-melt}^{(Fe^{2+}-Mg)} = \left(\frac{X_{Fe^{2+}}}{X_{Mg}}\right)^{ol} / \left(\frac{X_{Fe^{2+}}}{X_{Mg}}\right)^{melt} \quad on\ molar\ basis \qquad \text{Eqn. (1)}$$

The value of $Kd_{(Fe2+–Mg)}$ was found to be 0.30 ± 0.03, irrespective of temperature, melt redox state, and bulk composition (Roeder and Emslie, 1970). However, more recent studies have shown that Fe^{2+}-Mg exchange varies systematically from 0.13 to 0.45, responding to the physicochemical state of the crystallizing system (Kushiro and Walter, 1998; Kushiro and Mysen, 2002; Toplis, 2005; Putirka, 2016; Mollo and Hammer, 2017). The melt composition and structure exert great influence on the Fe^{2+}-Mg exchange, especially for the effect of Na_2O + K_2O (Sack et al., 1987; Toplis, 2005), TiO_2 (Wagner and Grove, 1997), and SiO_2 (Longhi et al., 1978). On this basis, Putirka (2016) has recently regressed 1270 experiments from literature, obtaining $Kd_{(Fe2+–Mg)}$ = 0.33 ± 0.04 for equilibrium crystallization in both terrestrial and extraterrestrial magmas.

Figure. 3.11 shows $Kd_{(Fe2+–Mg)}$ values from $-\Delta T35$ and $-\Delta T85$ experiments calculated using two different approaches: X^{ol} from core to rim is divided by 1) X^{melt} of the far-field melt (*FFM*) and 2) X^{melt} of the interface melt (*IM*). The Fe^{2+} content of the melt has been calculated at QFM-2 through the iron speciation model of Kress and Carmichael (1991). The effect of diffusion-controlled growth is to produce apparent values for the Fe^{2+}-Mg exchange rather than true values expected under interface-controlled regimes (Mollo and Hammer, 2017). The sign and magnitude of this exchange (and more in general the deviation of partition coefficient from equilibrium) depends on the intensive variables of the system and the balance between olivine growth rate and cation diffusivity in the melt (Mollo and Hammer, 2017). At $-\Delta T35$, olivines are in equilibrium with both *FFM* and *IM* (Figure. 3.11a), in agreement with the shorter diffusion length scales (Figure. 3.8a) and lower olivine growth rates (Figure. 3.4). These cooperative mechanisms minimize the disequilibrium effects caused by accumulation and/or depletion of cations at the olivine-melt interface, as long as the crystal growth rate does not greatly exceed the diffusion length scale of cations in the melt (Watson and Müller, 2009). At $-\Delta T85$, stronger concentration gradients develop in the melt (Figure. 3.9a) responding to the faster growth rates of olivine under larger degrees of undercooling (Figure. 3.4). As a consequence, the olivine core is in equilibrium with the *FFM*, which mostly represents the less differentiated melt composition feeding the early growth of olivine across the liquidus region (Figure. 3.11b). A similar finding has been documented by Brehm and Lange (2020) for the rapid phenocryst growth of olivine during decompression and ascent of basaltic magmas. Those authors observed that the most Mg-rich olivines remain in equilibrium with the whole-rock composition under a degree of undercooling of ~59 °C ($Kd_{(Fe2+-Mg)}$ = 0.31-0.36), as they represent the first crystals to grow from the host magma. Conversely, in the present study, the olivine rim is in equilibrium with the *IM* feeding its growth. However, no equilibrium is found between olivine core and *IM*, and between olivine rim and *FFM*. The only exception applies to $-\Delta T85$ and *CR4*, where the olivine core is always in equilibrium with both *IM* and *FFM* (Figure. 3.11b). This can be explained by the smaller value of G_{max} measured at 4 °C/h (Figure. 3.4), which induces less melt supersaturation phenomena at the crystal-melt interface. According to Sossi and O'Neill (2016), there is a systematic increase of $Kd_{(Fe2+-Mg)}$ measured at the olivine-melt interface with increasing *CR*. The increase of $Kd_{(Fe2+-Mg)}$ results from the development of more Fe-rich olivines relative to melt composition, owing the inability of the rapidly growing olivine to reject unwanted components, which, under fast *CR* have no enough time to diffuse away from the interface (cf. Grove and Raudsepp, 1978). But this kinetic effect is chiefly observed at very fast *CR* = 900 °C/hour, much faster than cooling rate experiments performed here (Sossi and O'Neill, 2016).

In absence of convective transport, diffusive boundary layers next to the advancing crystal surface may have a thickness variable from ~10 to a maximum of ~100 µm as a function of $-\Delta T$ (Lu et al., 1995). In our experiments the diffusive length scale changes from ~3 to ~150 µm. However, longer length scales may develop by impingement of diffusion fields surrounding skeletal/dendritic olivine branches that are in close proximity to one another (Figure. 3.9b; see also Baker, 2008). This causes steeper changes in melt concentration gradients, such that each single olivine branch competes with its near neighbors for chemical nutrients (Watson and Müller, 2009). Although bulk chemical disequilibrium is induced by the effect of $-\Delta T$ and *CR*, $Kd_{(Fe2+-Mg)}$ values calculated for olivine rim against *IM*, and for olivine core against *FFM*, are systematically within the equilibrium range of 0.33 ± 0.04 (Putirka, 2016). This may result from the achievement of local equilibrium at the crystal melt-interface, especially when the olivine growth rate greatly exceeds the diffusion length scale of both Fe^{2+} and Mg cations in the melt (Mollo and Hammer, 2017). A similar outcome has been documented by Conte et al. (2009) for the attainment of $Kd_{(Fe2+-Mg)}$ = 0.29-0.32 in experiments conducted on a trachybasalt cooled at 1 and 900 °C/h from the liquidus down to 1150, 1125, and 1000 °C. Comparable equilibrium values ranging from 0.27 to 0.33 have been also found in cooling-rate studies conducted on basaltic andesites (Baker and Grove, 1985) and lunar basalts (Walker et al., 1976; Powell et al., 1980; Kring and McKay, 1984). According to Walker et al. (1976), the tendency to maintain Fe^{2+}-Mg equilibrium with the coexisting melt is related to the early saturation of olivine at relatively high temperatures and in a narrow thermal range. For low-viscosity basalts, the diffusion of cations is also very fast at the interface melt. Therefore, during olivine growth, local interface equilibrium (i.e., equilibrium of a reaction in a small volume) is more favored than bulk system equilibrium (i.e., impingement of the diffusive boundary layers). Fe^{2+}-Mg partitioning data displayed in Figure. 3.11 suggest that a full equilibrium state between olivine and *IM* or *FFM* is achieved only at $-\Delta T \leq 35$ °C and *CR* ≤ 60 °C/h for $G_{max} = \sim 10^{-9}$-10^{-8} m/s (Figure. 3.4), whereas the bulk system starts to deviate from equilibrium at $-\Delta T = 85$ °C. The crystal surface remains in equilibrium with the coexisting melt through a diffusive mass transport established at the onset of olivine nucleation (Kring and McKay, 1984). It is likely that local equilibrium is achieved since there is no considerable change in the degree of crystallinity measured for the experimental charges (i.e., the degree of crystallization is bounded at ~11-14 wt.%). Even for the growth of skeletal crystals at large undercooling, it has been envisaged that the achievement of equilibrium may depend on the early formation of olivine branches, as protrusions that penetrate the diffusion field and thus sample fresh melt without the need for long-range diffusion (Walker et al., 1976). We can also speculate that at low values of $-\Delta T$ and *CR* the activation energy associated with the olivine formation is more favourable to the re-arrangement of Fe and Mg cations into the equilibrium stoichiometric ratio.

The corollary that chemical exchange reactions attain local equilibrium in a very small volume is confirmed by further tests based on the melt parameter *NBO/T*, which is the number of non-bridging oxygens *NBO* per tetrahedrally coordinated cation, *T* (Kushiro and Mysen, 2002). For melt compositions relevant to magmatic processes, Si and Al can be assumed as the dominant *T*-cations by ignoring the minor effects of P, Ti, and Fe^{3+} in tetrahedral coordination. Melt polymerization decreases as the proportion of octahedral relative to tetrahedral sites increases with increasing the number of network-modifier cations (e.g., Mg, Fe^{2+}, and Ca). As a consequence, natural magmas evolving from basalt to rhyolite exhibit *NBO/T* ranging from 2.5 to 0.05 (Mysen, 2004). For the tholeiitic basalt investigated in this study, we obtain *NBO/T* values bounded in a more restricted range comprised between 0.71 and 1.05 (see Supplementary

Material 2). In particular, *NBO/T* shows a decrease with increasing $-\Delta T$ and increase with increasing *CR*, as well as *NBO/T* measured at the *FFM* is slightly higher than that calculated at the *IM* (Supplementary Material 2). This points out that the solubility of network-modifying cations in the supersaturated melt explores minimum changes as the activity of *NBO* increases over the diffusion length scale (Mysen, 2004). Coherently with this consideration, we found that $Kd_{(Fe2+–Mg)}$ values calculated at the olivine-melt interface (i.e., 0.31-0.36 and 0.32-0.33 for $-\Delta T35$ and $-\Delta T85$, respectively) agree with those modeled (i.e., 0.32-0.33 and 0.31-0.32 for $-\Delta T35$ and $-\Delta T85$, respectively) using the partitioning equations derived for mafic terrestrial (Kushiro and Walter, 1998; Mibe et al., 2006; Kushiro and Mysen, 2002) and Martian (Filiberto and Dasgupta, 2011) basalts.

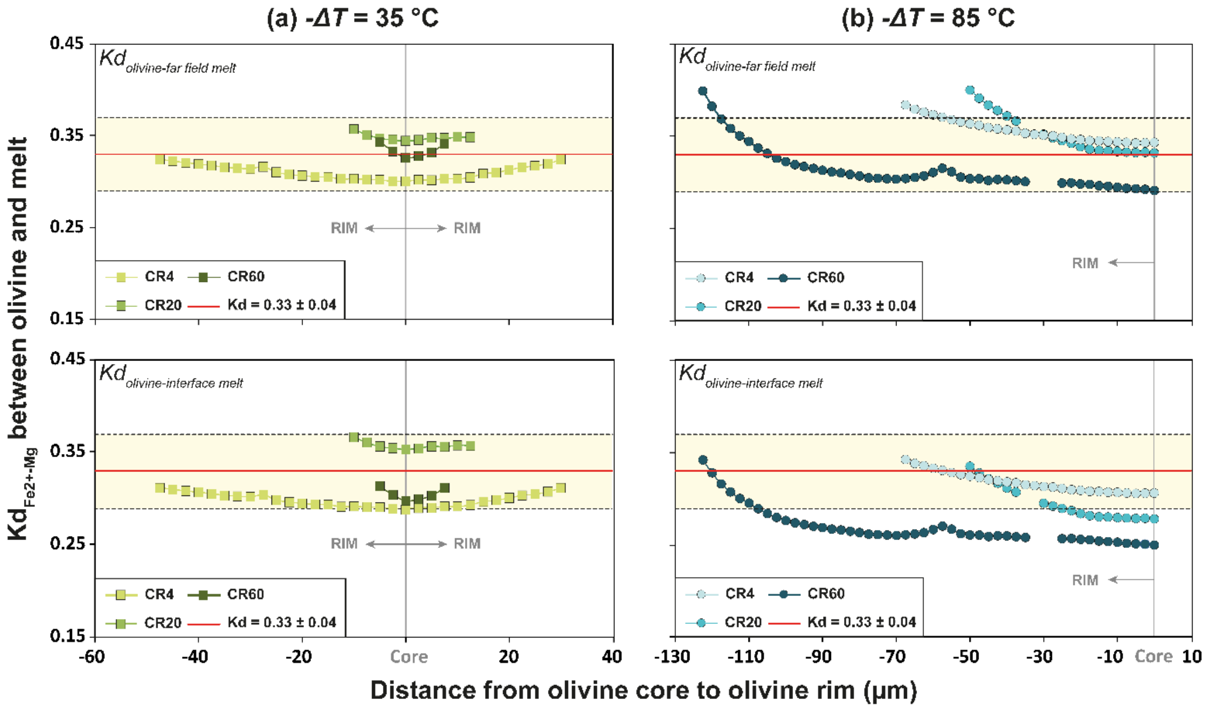

Figure 3.11. *Fe^{2+}-Mg exchange from undercooling experiments carried out at (a) 35 and (b) 85 °C. $Kd_{(Fe2+-Mg)}$ has been calculated using two different approaches: X^{ol} from core to rim is divided by 1) X^{melt} of the far-field melt (FFM) and 2) X^{melt} of the interface melt (IM). The yellow band refers to the equilibrium range determined by Putirka et al. (2016). Error bars are not observable if they are smaller than the symbols.*

As a further test of equilibrium partitioning, we have used the thermodynamic model recently proposed by Blundy et al. (2020) for the redox sensitive Fe^T-Mg exchange in olivine-saturated basalts. In this model, Fe^T is treated as total iron in the melt phase, such that $Kd_{(FeT-Mg)}$ changes as a function of $Fe^{3+}/\Sigma Fe$ by assuming a simple dilution of Fe^{2+} by Fe^{3+} in the melt. The model applicability extends over a wide range of oxygen fugacity (iron-wüstite buffer to air), pressure (≤ 1.7 GPa), temperature (1025–1425 °C) and melt composition (including ≤ 7 wt.% H_2O). We used as input parameters Fo_{78-85} (overall compositional range) measured for olivine and $Fe^{3+}/\Sigma Fe$ of the melt calculated at the experimental T–fO_2 conditions after Borisov et al. (2018), as required by the model of Blundy et al. (2020). The calculation return equilibrium crystallization for our experiments at $Kd_{(FeT-Mg)} = 0.25\text{-}0.34$, which is a remarkable result in consideration of the very different calibration strategies employed for *NBO/T*- and fO_2-based Fe^{2+}-Mg and Fe^T-Mg modeling, respectively. We conclude that almost constant $Kd_{(Fe2+-Mg)}$ and $Kd_{(FeT-Mg)}$ measured under diffusion-controlled growth regimes may indicate local equilibrium effects at the crystal-melt interface. Therefore, general form of Fe-Mg exchange does not necessarily represent bulk system equilibration, such that attained under interface-controlled growth regimes. Moreover, within the calibration error of models resulting from a weighted regression fit of equilibrium experimental data (e.g., Kress and Carmichael, 1991; Putirka, 2016; Blundy et al., 2020), the Fe-Mg exchange does not record kinetic deviations from equilibrium that may be more carefully identified by other cations sensitive to concentration-dependent partitioning between olivine and melt.

4.2. Olivine-melt partitioning behaviour

Apparent partition coefficients between olivine rim and interface melt have been calculated for Mg, Fe^{2+}, Ca, Mn, and Cr, according to the formula: $Kd = (C)^{ol} / (C)^{IM}$, where C is the cation concentration on a weight basis. Results are plotted in Figure. 3.12 as a function of *CR* for both $-\Delta T35$ and $-\Delta T85$ experimental conditions, also in comparison with MELTS simulations documenting thermodynamic equilibrium conditions. We observe that Kd_{Mg}, Kd_{Fe}, Kd_{Mn}, and Kd_{Cr} decrease with *CR* and increase with $-\Delta T$. Clear trends are measured only for the partitioning of major cations Mg and Fe^{2+}, whereas subtle variations appear for the minor cations Mn and Cr (Figure. 3.12). Kd_{Ca} depicts an opposite trend relative to the partitioning of major cations (i.e., Mg and Fe) in olivine structure (Figure. 3.12).

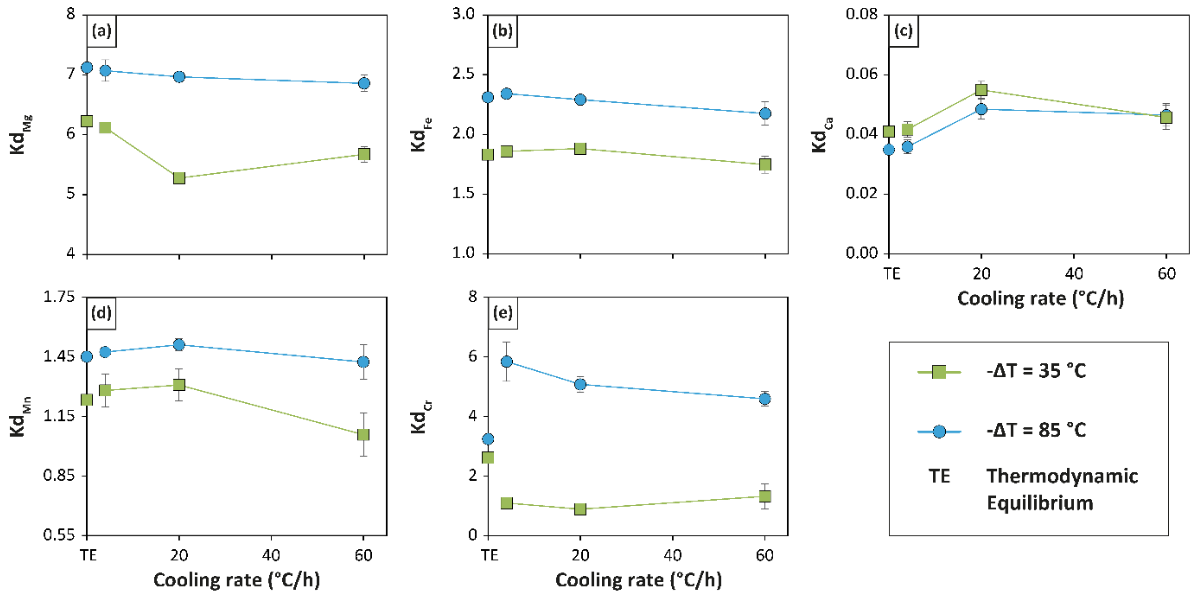

Figure 3.12. *Olivine-melt partition coefficients versus cooling rate. Data are plotted for undercooling conditions of 35 (green square) and 85 °C (blue circle).*

Figure. 3.13 shows measured partition coefficients plotted against those predicted by thermodynamic models relying on the minimization of Gibbs free energy exchange ($\Delta G_{exchange}$) and calibrated using phase equilibrium experiments. Specifically, partitioning models for Kd_{Mg} (Putirka, 2005), Kd_{Fe} (Putirka, 2005; Wang and Gaetani, 2008), Kd_{Mn} (Wang and Gaetani, 2008), and Kd_{Ca} (Libourel, 1999) point out near-equilibrium incorporation of cations in olivines from this study. Therefore, thermodynamic principles are still expected to govern the partitioning energetics, as long as the advancing olivine surface remains in local equilibrium with the adjacent melt supplying chemical nutrients to the crystalline layer (i.e., Albarede and Bottinga, 1972; Spandler and O'Neill, 2010; Mollo et al., 2013). Under such circumstances, $\Delta G_{exchange}$ holds for a small region of interface melt close to the olivine rim, where minor deviations from equilibrium occur with respect to the stronger chemical changes of the bulk system (Watson and Müller, 2009).

Bearing in mind the above considerations, there is a mutual interrelation between Fo in olivine (Figure. 3.6a) and $^{melt}Mg\#$ (Figure. 3.7b and 3.7c) upon the effect of *CR* and $-\Delta T$. Both Kd_{Mg} and Kd_{Fe} concurrently decrease with increasing disequilibrium, thereby leading to very minor changes for the general form of Fe-Mg exchange (Figure. 3.12). Thermodynamic modelling validates the linear dependence between Kd_{Fe} and Kd_{Mg}, in accordance with the relatively simple stoichiometry of olivine, in which Mg and Fe^{2+} dominate all other divalent cations (Jones, 1984, 2016). Moreover, thermodynamics of olivine mixing requires that largest Ca cations (r_{Ca}= 1.00 Å) substitute for both Fe^{2+} and Mg (r_{Fe} = 0.78 Å vs. r_{Mg} = 0.72 Å; Shannon, 1976) in the olivine structure, coherently with the antithetic relationship between Kd_{Ca} and Kd_{Fe} (or Kd_{Mg}), as displayed in Figure. 3.12. Because of differences between Fe^{2+} and Mg cation radii, Ca-Fe^{2+} substitutions in olivine are also likely more facilitated than Ca-Mg ones (Di Stefano et al., 2018). Since both Mn and Ca reside in the larger M2-site, the slight decrease of Kd_{Mn} as a function of $-\Delta T$ and *CR* may account for the higher proportion of $CaMgSiO_4$ at the expense of $MnMgSiO_4$ (Takahashi, 1978; Snyder and Carmichael, 1992). The equilibrium partitioning of Ca between olivine and interface melt agrees also with comparative results from Kennedy et al. (1993) and Pack and Palme (2003) showing that Ca in olivine is an excellent proxy to trace the CaO content of the melt even in systems rapidly cooled at rates up to 2,193 °C/h.

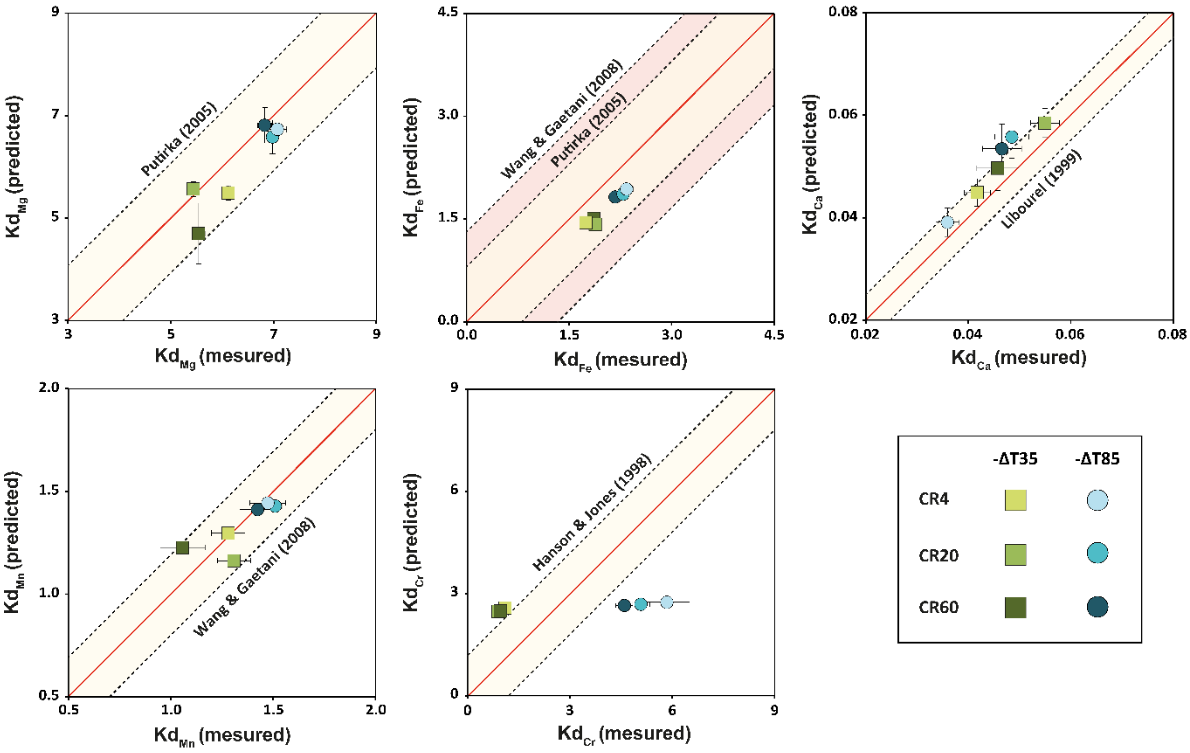

Figure 3.13. *Measured partition coefficients are plotted against those predicted by partitioning models for* Kd_{Mg} *(Putirka, 2005),* Kd_{Fe} *(Putirka, 2005; Wang and Gaetani, 2008),* Kd_{Mn} *(Wang and Gaetani, 2008),* Kd_{Ca} *(Libourel, 1999), and* Kd_{Cr} *(Hanson and Jones, 1998) for the experiments carried at* $-\Delta T35$ *(green square) and* $-\Delta T85$ *(blue circle), as well as CR4 (light shade), CR20 (medium shade), and CR60 (dark shade).*

In contrast with the cations discussed above, Figure. 3.13 shows that the partitioning model for Kd_{Cr} (Hanson and Jones, 1998) does not reproduce in full data from this study. We postulate that this model can be successfully employed for equilibrium olivine compositions, but deviations from the expected equilibrium could be caused by the influence of crystal field stabilization energy (CFSE) on the partitioning behaviour of Cr. CFSE is due to the repulsive forces generated by metal-oxygen bonds (i.e., ‹M–O›) in the mineral structure, as long as electrons in the metal orbitals are surrounded by negatively charged ligands (i.e., O^{2-} anions in metal-oxygen polyhedra; Burns, 1975). Cr in octahedral coordination have the highest crystal field stabilization energy ($^{Cr}CFSE_{octahedral}$ = 224.7 kJ/mol) and highest octahedral site preference energy ($^{Cr}OSPE$ = 157.7 kJ, where OSPE = $CFSE_{octahedral}$ – $CFSE_{tetrahedral}$; data from White, 2020). Olivine, as most mineral phases, has positive enthalpy and entropy of fusion such that entrance of cations into the lattice site increases with decreasing temperature (Blundy and Wood, 2003). However, the temperature effect is offset for the partitioning of Cr due to enthalpy changes associated with *CFSE* and *OSPE* (e.g., Henderson and Dale, 1970). In this perspective, the excess enthalpy of mixing (ΔH_{mix}) between forsterite and fayalite components in olivine solid solution can be partly described by the change of *CFSE* ($\Delta CFSE_{mix}$) as:

$$\Delta H_{mix} = W_{FoFa}(X_{Fa} - X_{Fo}) + \Delta CFSE_{mix} \qquad \text{Eqn. (2)}$$

where W_{FoFa} is the Margules mixing parameter (Ganguly and Saxena, 1987; Ganguly, 2020). Accordingly, the contribution of $\Delta CFSE_{mix}$, the partitioning of Cr is expected to increase with decreasing ‹M–O› distances of octahedral polyhedra (Burns, 1975).

Intriguingly, Figure. 3.12 displays that the value of Kd_{Cr} is of the same order of magnitude as Kd_{Mg}, especially at $-\Delta T85$. However, Cr is strongly ordered into the M1-site because of its high CFSE (Snyder and Carmichael, 1992; Papike et al., 2005). In terms of ionic radius (*r*) and charge (*Z*), Cr shows structural diversities which are responsible for the mobility of the metal cation in the melt and the Arrhenius behaviour of diffusion coefficient (*D*; Zhang et al., 2010). Although there is no *a priori* criterion to choose between the major influence of *r* relative to *Z* (and *vice versa*), LaTourrette et al. (1996) combined these two parameters as $\omega = r \times (2Z / d_{M-O})$, where d_{M-O} is the average metal-oxygen bond length and the number 2 at the numerator represents the charge of O^{2-} anions. According to the cation-oxygen coulombic potential and the knowledge that cations with low charge to radius ratio diffuse more rapidly (Zhang et al., 2010), we found that ω_{Mg} (1.37) < ω_{Cr} (1.85) by using ionic radii from Shannon (1976). At the same time, there is a clear and well-defined negative relationship between ln*D* and *ω*, as long as D_{Mg} (~10^{-11} m^2/s) > D_{Cr} (~10^{-13} m^2/s) in silicate melt systems at 1125-1175 °C (Behrens and Hahn, 2009; Zhang et al., 2010). In agreement with the structural equation proposed by LaTourrette et al. (1996), we speculate that transport of slower-diffusing Cr cations in the melt boundary layer is not sufficiently rapid to supply fresh nutrients to the advancing olivine surface in the same proportion as for faster-diffusing Mg cations. Therefore, deviation from partitioning equilibrium would be exacerbated by the slow mobility of Cr and the lack of a local interface equilibrium (i.e., equilibrium of a reaction in a small volume) due to a steady-state diffusive mass transport.

As an alternative scenario for the different partitioning behaviour of Cr upon the effect of olivine growth kinetics, we have to consider that deviation from equilibrium partitioning of Kd_{Cr} is not systematic as a function of $-\Delta T$ and *CR* (Figure. 13). Spurious modeling data could be caused by imprecision associated with microprobe analyses conducted for low concentration cations and/or disequilibrium partitioning effects due to the slow diffusivity of Mg in the melt. In this perspective, the following considerations should be kept in mind:

1) for low concentration cations, the microprobe precision is better than 10% at the analytical conditions suggested by Sobolev et al. (2007) and Shea et al. (2019) for olivine and glass, respectively. The compositional variability of the diffusive boundary layer in the melt (i.e., Cr_2O_3 variability ≥ 18% from *FFM* to *IM*) is systematically higher than microprobe uncertainty. Moreover, Ca and Mn are low concentration cations too, but their apparent partition coefficients match with those modeled at equilibrium conditions (Figure. 3.13);

2) the equilibrium partitioning model of Hanson and Jones (1998) for Cr is highly dependent on the melt composition and structure. Therefore, the lack of a systematic deviation from equilibrium partitioning (Figure. 3.13) may reflect the development of diffusive melts that invalidate the applicability of melt-dependent equilibrium models. Strong melt heterogeneities result from the impingement of distinct diffusion fields of nearby olivine crystals, leading to scattered melt analyses as a function of $-\Delta T$ and *CR* (Figure. 3.7a). This observation is consistent with the slow mobility of Cr and the lack of a local interface equilibrium during olivine growth.

Because olivine-melt partition coefficients depend on activity-composition relationships in both crystal and melt (e.g., Snyder and Carmichael, 1992), it is not straightforward to disentangle completely the effects of crystal chemistry and melt composition, especially when different diffusive boundary layers overlap. Therefore, we cannot exclude that other potential substitution mechanisms may operate at the crystal-melt interface for the incorporation of minor cations in the lattice site of olivine. Investigating these substitution models between olivine and Hawaiian tholeiitic basalt will be a subject of future study.

4.3. Implications for diffusion chronometry

Diffusion chronometry is recognized as an important technique to determine the timescales and duration of magma residence, mixing, and transfer through different magmatic reservoirs beneath active volcanic settings (e.g., Costa et al., 2008 and references therein). The basic concept of this technique relies on the fact that compositional zoning in natural olivine phenocrysts is affected by diffusive relaxation, such that intracrystalline concentration gradients between different compositional plateaus start to erase due to chemical diffusion. As a consequence, chemical heterogeneities in olivine (i.e., crystal zonation) should decay with time according to an explicit Arrhenius relationship for the diffusing cation of interest (e.g., Fe-Mg and Mn; Costa et al., 2008; Kahl et al., 2011).

Turning to data from this study, olivine compositional profiles obtained at *–ΔT85* and *CR60* (Figure. 3.10) mimic quite well natural olivine zoning patterns expected during mixing of compositionally distinct magmas via injections of mafic recharge melts into shallower storage regions. In this perspective, the kinetic growth of olivine may cause over- or under-estimation of the extent to which the initial concentration profile in olivine is erased as a function of the diffusion rate of cations within the lattice.

Therefore, in order to correctly calculate the timescales of magmatic processes, it is vital to individuate and exclude olivine concentration profiles resulting from rapid growth and/or dissolution phenomena. Following the robustness criteria defined by Kahl et al. (2011), reliable timescales can be estimated by 1) modeling anisotropic diffusion profiles measured along different crystallographic directions for the same crystal, 2) comparing modeling results from concentration profiles of multiple cations (e.g., Fe-Mg and Mn) and excluding olivine phenocrysts returning discrepant estimates, and 3) performing multielemental maps for identifying true diffusion zoning patterns of anisotropic diffusing cations, which correspond to zonation with length varying as a function of the crystallographic direction. Multielement approaches to decoding olivine zoning patterns can help determine the interplay between growth- and diffusion-induced zoning by comparing slow- and fast-diffusing cations. For example, while rapid growth zonation is preserved for slow-diffusing P cations (Welsch et al., 2014), growth-induced development of Fe-Mg gradients in olivine could be erased by intracrystalline re-equilibration of fast-diffusing Fe and Mg cations (Shea et al., 2015).

Looking at the partitioning data displayed in Figure. 3.12, we can also suggest an additional tool to test whether growth kinetics influenced the incorporation of cations in the lattice site of olivine at the time of crystallization. Indeed, partitioning trends measured for highly compatible cations (i.e., Mg and Cr) show that, from *CR4* to *CR60*, the change of Kd_{Cr} (~19%) is relatively higher than that of Kd_{Mg} (~5%). This deviation from equilibrium is exacerbated from $-\Delta T35$ to $-\Delta T85$, where Kd_{Cr} and Kd_{Mg} increase by ~341% and 18%, respectively. On this basis, we might be able to use, for example, the Mg/Cr ratio in olivine to identify regions within natural phenocrysts that are affected by increased growth rates and kinetic effects during the dynamic crystallization of magmas.

5. Concluding remarks

The kinetic growth of olivine has been experimentally investigated for a tholeiitic basalt crystallized under variable undercooling and cooling rate conditions. Textural and compositional changes of olivine crystals have been discussed in terms of crystal–melt interface reactions at conditions far from bulk chemical equilibrium. According to the role played by supersaturation phenomena on crystal growth, major-minor cation concentrations in olivine have been interpreted in relation to chemical concentration gradients in the surrounding glass. Through this comparative approach, the following conclusions can be drawn:

1) euhedrality and polyhedral olivine morphologies are obtained at small undercooling ($-\Delta T35$), irrespective of the magnitude of cooling rate (for CR varying from 4 to 60 °C/h). Conversely, at large undercooling ($-\Delta T85$), olivines show strong disequilibrium skeletal and/or dendritic textures, which are also exacerbated by the effect of cooling rate;
2) the olivine growth rate increases as both undercooling and cooling rate increase, in accord with supersaturation and strong diffusion effects in the melt feeding the crystal growth;
3) Mg-poor olivines crystallize from the tholeiitic basalt, as long as the diffusive boundary layer in the melt becomes progressively depleted in cations compatible with the lattice site. The opposite occurs for the disequilibrium incorporation Ca, owing to its

incompatible behaviour with the olivine crystal structure and consequent enrichment in the interface melt;

4) on the basis of Fe^{2+}-Mg exchange reaction, olivines formed at small undercooling are always in equilibrium with both far-field melt and interface melt, given that the crystal growth is not fast enough to cause strong concentration gradients in the interface melt. At large undercooling, the Fe^{2+}-Mg exchange indicates two distinct equilibration stages between i) olivine core and far-field and ii) olivine rim and the interface melt. A similar result is also obtained for calculations performed by Fe^{T}-Mg exchange model, where Fe^{T} is treated as total iron in the melt phase. This observation attests the maintenance of local crystal-melt equilibrium over the entire olivine growth;

5) partition coefficients Kd_{Mg}, Kd_{Fe}, Kd_{Mn}, and Kd_{Cr} decrease with cooling rate and increase with undercooling, whereas Kd_{Ca} shows an opposite trend. Partitioning modeling confirms that Mg, Fe, Mn, and Ca are incorporated in the olivine lattice site at near-equilibrium proportions. On the other hand, thermodynamic-based model fails to reproduce the value of Kd_{Cr} likely due to the influence of crystal field stabilization energy on the partitioning behaviour. Also, transport of slower-diffusing Cr cations in the interface melt is not sufficiently rapid to supply fresh nutrients to the advancing olivine surface in the same proportion as for faster-diffusing Mg cations;

6) the kinetic growth of olivine may produce intracrystalline compositional profiles similar to those expected via cation diffusion in the lattice site of the crystal. Therefore, several test criteria for the selection of concentration profiles should be adopted in order to correctly model the timescales of magmatic processes.

Acknowledgments

The authors are very grateful to Thomas Shea for sharing the same starting material used in his previous works. Thanks to Giacomo Pozzi for his help with microprobe analysis and imagery. Thanks go to Flavio Di Stefano for his help in the laboratory activities. This research was partially supported by CNRS-INSU program PNP. This work has been greatly improved by the helpful and thoughtful reviews of Keith Putirka and Paolo Sossi. Donald Dingwell is also acknowledged for his valuable editorial guidance.

Supplementary Materials

Supplementary Material 1. (table) can be found online at:

https://doi.org/10.1016/j.chemgeo.2021.120485.

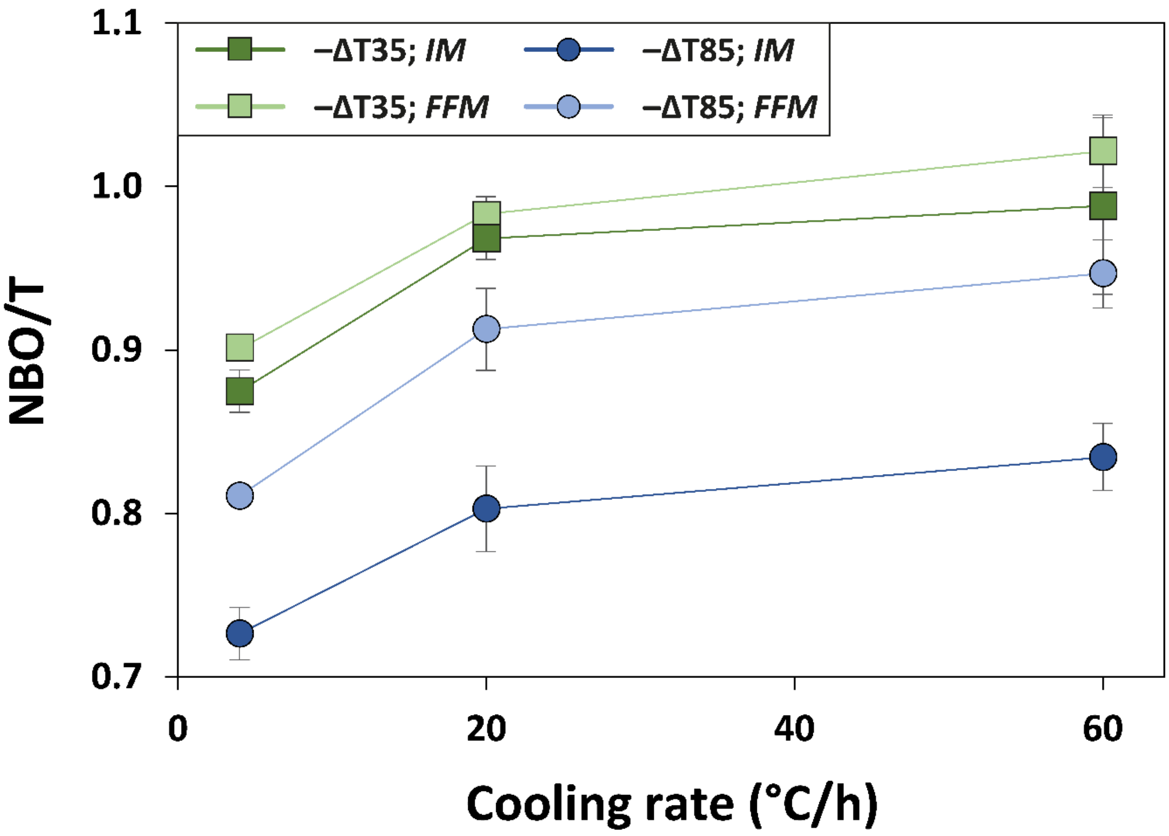

Supplementary Material 2. *NBO/T against cooling rate calculated for both –ΔT35 (green square) and –ΔT85 (blue circle), and for the interface melt (IM; dark shade) and far field melt (FFM; light shade)*

References – Chapter 3

Albarede, F., & Bottinga, Y. (1972). Kinetic disequilibrium in trace element partitioning between phenocrysts and host lava. Geochimica et Cosmochimica Acta, 36(2), 141-156. doi.org/10.1016/0016-7037(72)90003-8

Baker, D. R. (2008). The fidelity of melt inclusions as records of melt composition. Contributions to Mineralogy and Petrology, 156(3), 377-395. doi.org/10.1007/s00410-008-0291-3

Baker, M. B., & Grove, T. L. (1985). Kinetic controls on pyroxene nucleation and metastable liquid lines of descent in a basaltic andesite. American Mineralogist, 70(3-4), 279-287.

Behrens, H., & Hahn, M. (2009). Trace element diffusion and viscous flow in potassium-rich trachytic and phonolitic melts. Chemical Geology, 259(1-2), 63-77. doi.org/10.1016/j.chemgeo.2008.10.014

Blundy, J., Melekhova, E., Ziberna, L., Humphreys, M.C., Cerantola, V., Brooker, R.A., McCammon, C.A., Pichavant, M. and Ulmer, P. (2020). Effect of redox on Fe–Mg–Mn exchange between olivine and melt and an oxybarometer for basalts. Contributions to mineralogy and petrology, 175(11), 1-32. doi.org/10.1007/s00410-020-01736-7

Blundy, J., & Wood, B. (2003). Mineral-melt partitioning of uranium, thorium and their daughters. Reviews in Mineralogy and Geochemistry, 52(1), 59-123. doi.org/10.2113/0520059

Borisov, A., Behrens, H., & Holtz, F. (2018). Ferric/ferrous ratio in silicate melts: a new model for 1 atm data with special emphasis on the effects of melt composition. Contributions to Mineralogy and Petrology, 173(12), 1-15. doi.org/10.1007/s00410-018-1524-8

Brehm, S. K., & Lange, R. A. (2020). Evidence of rapid phenocryst growth of olivine during ascent in basalts from the Big Pine volcanic field: Application of olivine-melt thermometry and hygrometry at the liquidus. Geochemistry, Geophysics, Geosystems, 21(10), e2020GC009264. doi.org/10.1007/s00410-018-1524-8

Burns, R. G. (1975). Crystal field effects in chromium and its partitioning in the mantle. In Chromium: its Physicochemical Behaviour and Petrologic Significance (pp. 857-864). Pergamon. doi.org/10.1016/0016-7037(75)90031-9

Conte, A. M., Dolfi, D., Gaeta, M., Misiti, V., Mollo, S., & Perinelli, C. (2009). Experimental constraints on evolution of leucite-basanite magma at 1 and 10− 4 GPa: implications for parental compositions of Roman high-potassium magmas. European Journal of Mineralogy, 21(4), 763-782. doi.org/10.1127/0935-1221/2009/0021-1934

Conte, A. M., Perinelli, C., & Trigila, R. (2006). Cooling kinetics experiments on different Stromboli lavas: Effects on crystal morphologies and phases composition. Journal of Volcanology and Geothermal Research, 155(3-4), 179-200. doi.org/10.1016/j.jvolgeores.2006.03.025

Corrigan, G. M. (1982). Supercooling and the crystallization of plagioclase, olivine, and clinopyroxene from basaltic magmas. Mineralogical Magazine, 46(338), 31-42. doi.org/10.1180/minmag.1982.046.338.06

Costa, F., Dohmen, R., & Chakraborty, S. (2008). Time scales of magmatic processes from modeling the zoning patterns of crystals. Reviews in Mineralogy and Geochemistry, 69(1), 545-594. doi.org/10.2138/rmg.2008.69.14

Di Stefano, F., Mollo, S., Scarlato, P., Nazzari, M., Bachmann, O., & Caruso, M. (2018). Olivine compositional changes in primitive magmatic skarn environments: A reassessment of divalent cation partitioning models to quantify the effect of carbonate assimilation. Lithos, 316, 104-121. doi.org/10.1016/j.lithos.2018.07.008

Donaldson, C. H. (1976). An experimental investigation of olivine morphology. Contributions to mineralogy and Petrology, 57(2), 187-213. doi.org/10.1007/BF00405225

Faure, F., Schiano, P., Trolliard, G., Nicollet, C., & Soulestin, B. (2007). Textural evolution of polyhedral olivine experiencing rapid cooling rates. Contributions to Mineralogy and Petrology, 153(4), 405-416. doi.org/10.1007/s00410-006-0154-8

Faure, F., Trolliard, G., Nicollet, C., & Montel, J. M. (2003). A developmental model of olivine morphology as a function of the cooling rate and the degree of undercooling. Contributions to Mineralogy and Petrology, 145(2), 251-263. doi.org/10.1007/s00410-003-0449-y

Filiberto, J., & Dasgupta, R. (2011). Fe2+–Mg partitioning between olivine and basaltic melts: Applications to genesis of olivine-phyric shergottites and conditions of melting in the Martian interior. Earth and Planetary Science Letters, 304(3-4), 527-537. doi.org/10.1016/j.epsl.2011.02.029

First, E., & Hammer, J. (2016). Igneous cooling history of olivine-phyric shergottite Yamato 980459 constrained by dynamic crystallization experiments. Meteoritics & Planetary Science, 51(7), 1233-1255. doi.org/10.1111/maps.12659

First, E. C., Leonhardi, T. C., & Hammer, J. E. (2020). Effects of superheating magnitude on olivine growth. Contributions to Mineralogy and Petrology, 175(2), 1-14. doi.org/10.1007/s00410-019-1638-7

Foley, S. F., Prelevic, D., Rehfeldt, T., & Jacob, D. E. (2013). Minor and trace elements in olivines as probes into early igneous and mantle melting processes. Earth and Planetary Science Letters, 363, 181-191. doi.org/10.1016/j.epsl.2012.11.025

Freda, C., Gaeta, M., Misiti, V., Mollo, S., Dolfi, D., & Scarlato, P. (2008). Magma–carbonate interaction: an experimental study on ultrapotassic rocks from Alban Hills (Central Italy). Lithos, 101(3-4), 397-415. doi.org/10.1016/j.lithos.2007.08.008

Ganguly, J. (2008). Thermodynamics in earth and planetary sciences. Berlin: Springer.

Ganguly, J., Saxena, S.K. (1987). Mixtures and mineral reactions. 291 p. Springer-Verlag, Berlin.

Garcia, M. O., Pietruszka, A. J., & Rhodes, J. M. (2003). A petrologic perspective of the summit magma chamber of Kilauea Volcano, Hawai ‘i. Journal of Petrology, 44, 2313-2339. doi.org/10.1093/petrology/egg079

Giuliani, L., Iezzi, G., Hippeli, T., Davis, M., Elbrecht, A., Vetere, F., Nazzari, M. & Mollo, S. (2020). The Onset and Solidification Path of a Basaltic Melt by in situ Differential Scanning Calorimetry (DSC) and ex situ Investigations. Frontiers in Earth Science, 8, 337. doi.org/10.3389/feart.2020.00337

Grant, T. B., & Kohn, S. C. (2013). Phosphorus partitioning between olivine and melt: An experimental study in the system Mg2SiO4-Ca2Al2Si2O9-NaAlSi3O8-Mg3 (PO4) 2. American Mineralogist, 98(10), 1860-1869. doi.org/10.2138/am.2013.4237

Grove, T. L., & Raudsepp, M. (1978). Effects of kinetics on the crystallization of quartz normative basalt 15597-an experimental study. In Lunar and Planetary Science Conference Proceedings (Vol. 9, pp. 585-599).

Gualda, G. A., Ghiorso, M. S., Lemons, R. V., & Carley, T. L. (2012). Rhyolite-MELTS: a modified calibration of MELTS optimized for silica-rich, fluid-bearing magmatic systems. Journal of Petrology, 53(5), 875-890. doi.org/10.1093/petrology/egr080

Hammer, J. E. (2008). Experimental studies of the kinetics and energetics of magma crystallization. Reviews in mineralogy and geochemistry, 69(1), 9-59. doi.org/10.2138/rmg.2008.69.2

Hammer, J. E. (2006). Influence of fO2 and cooling rate on the kinetics and energetics of Fe-rich basalt crystallization. Earth and Planetary Science Letters, 248(3-4), 618-637. doi.org/10.1016/j.epsl.2006.04.022

Hammer, J. E., & Rutherford, M. J. (2002). An experimental study of the kinetics of decompression-induced crystallization in silicic melt. Journal of Geophysical Research: Solid Earth, 107(B1), ECV-8. doi.org/10.1029/2001jb000281

Hanson, B., & Jones, J. H. (1998). The systematics of Cr3+ and Cr2+ partitioning between olivine and liquid in the presence of spinel. American Mineralogist, 83(7-8), 669-684. doi.org/10.2138/am-1998-7-801

Henderson, P., & Dale, I. M. (1970). The partitioning of selected transition element ions between olivine and groundmass of oceanic basalts. Chemical Geology, 5(4), 267-274. doi.org/10.1016/0009-2541(70)90044-6

Jambon, A., Lussiez, P., Clocchiatti, R., Weisz, J., & Hernandez, J. (1992). Olivine growth rates in a tholeiitic basalt: An experimental study of melt inclusions in plagioclase. Chemical Geology, 96(3-4), 277-287. doi.org/10.1016/0009-2541(92)90059-E

Jones, J. H. (2016). Thoughts and reminiscences on experimental trace element partitioning. Geochemical Perspectives, 5(2), 147-147.

Jones, J. H. (1984). Temperature and pressure-independent correlations of olivine/liquid partition coefficients and their application to trace element partitioning. Contributions to Mineralogy and Petrology, 88(1), 126-132. doi.org/10.1007/BF00371417

Kahl, M., Chakraborty, S., Costa, F., & Pompilio, M. (2011). Dynamic plumbing system beneath volcanoes revealed by kinetic modeling, and the connection to monitoring data: An example from Mt. Etna. Earth and Planetary Science Letters, 308(1-2), 11-22. doi.org/10.1016/j.epsl.2011.05.008

Kennedy, A. K., Lofgren, G. E., & Wasserburg, G. J. (1993). An experimental study of trace element partitioning between olivine, orthopyroxene and melt in chondrules: equilibrium values and kinetic effects. Earth and Planetary Science Letters, 115(1-4), 177-195. doi.org/10.1029/2011GC003655

Koepke, J., France, L., Müller, T., Faure, F., Goetze, N., Dziony, W., & Ildefonse, B. (2011). Gabbros from IODP Site 1256, equatorial Pacific: Insight into axial magma chamber processes at fast spreading ocean ridges. Geochemistry, Geophysics, Geosystems, 12(9). doi.org/10.1029/2011GC003655

Kress, V. C., & Carmichael, I. S. (1991). The compressibility of silicate liquids containing Fe 2 O 3 and the effect of composition, temperature, oxygen fugacity and pressure on their redox states. Contributions to Mineralogy and Petrology, 108(1), 82-92. doi.org/10.1007/BF00307328

Kring, D. A., & McKay, G. A. (1984). Chemical gradients in glass adjacent to olivine in experimental charges and Apollo 15 green glass vitrophyres. In Lunar and Planetary Science Conference (Vol. 15, pp. 461-462).

Kushiro, I., & Mysen, B. O. (2002). A possible effect of melt structure on the Mg-Fe2+ partitioning between olivine and melt. Geochimica et Cosmochimica Acta, 66(12), 2267-2272. doi.org/10.1016/S0016-7037(01)00835-3

Kushiro, I., & Walter, M. J. (1998). Mg-Fe partitioning between olivine and mafic-ultramafic melts. Geophysical Research Letters, 25(13), 2337-2340. doi.org/10.1029/98GL01844

LaTourrette, T., Wasserburg, G. J., & Fahey, A. J. (1996). Self diffusion of Mg, Ca, Ba, Nd, Yb, Ti, Zr, and U in haplobasaltic melt. Geochimica et Cosmochimica Acta, 60(8), 1329-1340. doi.org/10.1016/0016-7037(96)00015-4

Le Bas, M. J., Maitre, R. L., Streckeisen, A., Zanettin, B., & IUGS Subcommission on the Systematics of Igneous Rocks. (1986). A chemical classification of volcanic rocks based on the total alkali-silica diagram. Journal of petrology, 27(3), 745-750. doi.org/10.1093/petrology/27.3.745

Libourel, G. (1999). Systematics of calcium partitioning between olivine and silicate melt: implications for melt structure and calcium content of magmatic olivines. Contributions to Mineralogy and Petrology, 136(1), 63-80. doi.org/10.1007/s004100050524

Longhi, J., Walker, D., & Hays, J. F. (1978). The distribution of Fe and Mg between olivine and lunar basaltic liquids. Geochimica et Cosmochimica Acta, 42(10), 1545-1558. doi.org/10.1016/0016-7037(78)90025-X

Lu, F., Anderson, A. T., & Davis, A. M. (1995). Diffusional gradients at the crystal/melt interface and their effect on the compositions of melt inclusions. The Journal of Geology, 103(5), 591-597. doi.org/10.1086/629778

Lynn, K. J., Shea, T., & Garcia, M. O. (2017). Nickel variability in Hawaiian olivine: Evaluating the relative contributions from mantle and crustal processes. American Mineralogist, 102(3), 507-518. doi.org/10.2138/am-2017-5763

Mibe, K., Fujii, T., Yasuda, A., & Ono, S. (2006). Mg–Fe partitioning between olivine and ultramafic melts at high pressures. Geochimica et Cosmochimica Acta, 70(3), 757-766. doi.org/10.1016/j.gca.2005.09.022

Mollo, S., & Hammer, J. E. (2017). Dynamic crystallization in magmas. EMU Notes Mineral, 16, 373-418. doi.org/10.1180/EMU-notes.16.12

Mollo, S., Blundy, J. D., Iezzi, G., Scarlato, P., & Langone, A. (2013). The partitioning of trace elements between clinopyroxene and trachybasaltic melt during rapid cooling and crystal growth. Contributions to Mineralogy and Petrology, 166(6), 1633-1654. doi.org/10.1007/s00410-013-0946-6

Mollo, S., Lanzafame, G., Masotta, M., Iezzi, G., Ferlito, C., & Scarlato, P. (2011). Cooling history of a dike as revealed by mineral chemistry: a case study from Mt. Etna volcano. Chemical Geology, 288(1-2), 39-52. doi.org/10.1016/j.chemgeo.2011.06.016

Moore, A. E. (1988). Olivine: a monitor of magma evolutionary paths in kimberlites and olivine melilitites. Contributions to Mineralogy and Petrology, 99(2), 238-248. doi.org/10.1007/BF00371464

Mourey, A. J., & Shea, T. (2019). Forming olivine phenocrysts in basalt: a 3D characterization of growth rates in laboratory experiments. Frontiers in Earth Science, 7, 300. doi.org/10.3389/feart.2019.00300

Mysen, B. O. (2004). Element partitioning between minerals and melt, melt composition, and melt structure. Chemical Geology, 213(1-3), 1-16. doi.org/10.1016/j.chemgeo.2004.08.028

Pack, A., & Palme, H. (2003). Partitioning of Ca and Al between forsterite and silicate melt in dynamic systems with implications for the origin of Ca, Al-rich forsterites in primitive meteorites. Meteoritics & Planetary Science, 38(8), 1263-1281. doi.org/10.1111/j.1945-5100.2003.tb00312.x

Papike, J. J., Karner, J. M., & Shearer, C. K. (2005). Comparative planetary mineralogy: Valence state partitioning of Cr, Fe, Ti, and V among crystallographic sites in olivine, pyroxene, and spinel from planetary basalts. American Mineralogist, 90(2-3), 277-290. doi.org/10.2138/am.2005.1779

Perfit, M.R., Fornari, D.J., Ridley, W.I., Kirk, P.D., Casey, J., Kastens, K.A., Reynolds, J.R., Edwards, M., Desonie, D., Shuster, R. and Paradis, S. (1996). Recent volcanism in the Siqueiros transform fault: picritic basalts and implications for MORB magma genesis. Earth and Planetary Science Letters, 141(1-4), 91-108. doi.org/10.1016/0012-821x(96)00052-0

Powell, M. A., Walker, D., & Hays, J. F. (1980). Experimental solidification of a eucrite basalt: Microprobe studies. In Lunar and Planetary Science Conference (Vol. 11, pp. 896-898).

Putirka, K. (2016). Rates and styles of planetary cooling on Earth, Moon, Mars, and Vesta, using new models for oxygen fugacity, ferric-ferrous ratios, olivine-liquid Fe-Mg exchange, and mantle potential temperature. American Mineralogist, 101(4), 819-840. doi.org/10.2138/am-2016-5402

Putirka, K. D. (2005). Mantle potential temperatures at Hawaii, Iceland, and the mid-ocean ridge system, as inferred from olivine phenocrysts: Evidence for thermally driven mantle plumes. Geochemistry, Geophysics, Geosystems, 6(5). doi.org/10.1029/2005GC000915

Roeder, P. L., & Emslie, R. (1970). Olivine-liquid equilibrium. Contributions to mineralogy and petrology, 29(4), 275-289. doi.org/10.1007/BF00371276

Sack, R. O., Walker, D., & Carmichael, I. S. (1987). Experimental petrology of alkalic lavas: constraints on cotectics of multiple saturation in natural basic liquids. Contributions to Mineralogy and Petrology, 96(1), 1-23. doi.org/10.1007/BF00375521

Shannon, R. D. (1976). Revised effective ionic radii and systematic studies of interatomic distances in halides and chalcogenides. Acta crystallographica section A: crystal physics, diffraction, theoretical and general crystallography, 32(5), 751-767. doi.org/10.1107/S0567739476001551

Shea, T., Hammer, J.E., Hellebrand, E., Mourey, A.J., Costa, F., First, E.C., Lynn, K.J. and Melnik, O. (2019). Phosphorus and aluminum zoning in olivine: contrasting behaviour of two nominally incompatible trace elements. Contributions to Mineralogy and Petrology, 174(10), 1-24. doi.org/10.1007/s00410-019-1639-6

Shea, T., Lynn, K. J., & Garcia, M. O. (2015). Cracking the olivine zoning code: Distinguishing between crystal growth and diffusion. Geology, 43(10), 935-938. doi.org/10.1130/G37082.1

Snyder, D. A., & Carmichael, I. S. (1992). Olivine-liquid equilibria and the chemical activities of FeO, NiO, Fe2O3, and MgO in natural basic melts. Geochimica et Cosmochimica Acta, 56(1), 303-318. doi.org/10.1016/0016-7037(92)90135-6

Sobolev, A.V., Hofmann, A.W., Kuzmin, D.V., Yaxley, G.M., Arndt, N.T., Chung, S.L., Danyushevsky, L.V., Elliott, T., Frey, F.A., Garcia, M.O. and Gurenko, A.A. (2007). The amount of recycled crust in sources of mantle-derived melts. science, 316(5823), 412-417. doi.org/10.1126/science. 1140516

Sossi, P. A., & O'Neill, H. S. C. (2016). Liquidus temperatures of komatiites and the effect of cooling rate on element partitioning between olivine and komatiitic melt. Contributions to Mineralogy and Petrology, 171(5), 49. doi.org/10.1007/s00410-016-1260-x

Spandler, C., & O'Neill, H. S. C. (2010). Diffusion and partition coefficients of minor and trace elements in San Carlos olivine at 1,300 C with some geochemical implications. Contributions to Mineralogy and Petrology, 159(6), 791-818. doi.org/10.1007/s00410-009-0456-8

Takahashi, E. (1978). Partitioning of Ni2+, Co2+, Fe2+, Mn2+ and Mg2+ between olivine and silicate melts: compositional dependence of partition coefficient. Geochimica et Cosmochimica Acta, 42(12), 1829-1844. doi.org/10.1016/0016-7037(78)90238-7

Toplis, M. J. (2005). The thermodynamics of iron and magnesium partitioning between olivine and liquid: criteria for assessing and predicting equilibrium in natural and experimental systems. Contributions to Mineralogy and Petrology, 149(1), 22-39. doi.org/10.1007/s00410-004-0629-4

Ujike, O. (1982). Microprobe mineralogy of plagioclase, clinopyroxene and amphibole as records of cooling rate in the Shirotori—Hiketa dike swarm, northeastern Shikoku, Japan. Lithos, 15(4), 281-293. doi.org/10.1016/0024-4937(82)90019-6

Vetere, F., Iezzi, G., Behrens, H., Holtz, F., Ventura, G., Misiti, V., Cavallo, A., Mollo, S. and Dietrich, M. (2015). Glass forming ability and crystallisation behaviour of sub-alkaline silicate melts. Earth-science reviews, 150, 25-44. doi.org/10.1016/j.earscirev.2015.07.001

Vetere, F., Iezzi, G., Behrens, H., Cavallo, A., Misiti, V., Dietrich, M., Knipping, J., Ventura, G. and Mollo, S. (2013). Intrinsic solidification behaviour of basaltic to rhyolitic melts: a cooling rate experimental study. Chemical Geology, 354, 233-242. doi.org/10.1016/j.chemgeo.2013.06.007

Wagner, T. P., & Grove, T. L. (1997). Experimental constraints on the origin of lunar high-Ti ultramafic glasses. Geochimica et Cosmochimica Acta, 61(6), 1315-1327. doi.org/10.1016/S0016-7037(96)00387-0

Walker, D., Kirkpatrick, R. J., Longhi, J., & Hays, J. F. (1976). Crystallization history of lunar picritic basalt sample 12002: Phase-equilibria and cooling-rate studies. Geological Society of America Bulletin, 87(5), 646-656. doi.org/10.1130/0016-7606(1976)87<646:CHOLPB>2.0.CO;2

Wang, Z., & Gaetani, G. A. (2008). Partitioning of Ni between olivine and siliceous eclogite partial melt: experimental constraints on the mantle source of Hawaiian basalts. Contributions to Mineralogy and Petrology, 156(5), 661-678. doi.org/10.1007/s00410-008-0308-y

Watson, E. B., & Müller, T. (2009). Non-equilibrium isotopic and elemental fractionation during diffusion-controlled crystal growth under static and dynamic conditions. Chemical Geology, 267(3-4), 111-124. doi.org/10.1016/j.chemgeo.2008.10.036

Welsch, B., Hammer, J., & Hellebrand, E. (2014). Phosphorus zoning reveals dendritic architecture of olivine. Geology, 42(10), 867-870. doi:10.1130 /G35691.1

Welsch, B., Faure, F., Famin, V., Baronnet, A., & Bachèlery, P. (2013). Dendritic crystallization: A single process for all the textures of olivine in basalts?. Journal of Petrology, 54(3), 539-574. doi.org/10.1093/petrology/egs077

White, W. M. (2020). Geochemistry. John Wiley & Sons.

Zhang, Y., Ni, H., & Chen, Y. (2010). Diffusion data in silicate melts. Reviews in Mineralogy and Geochemistry, 72(1), 311-408. doi.org/10.2138/rmg.2010.72.8

Chapter 4

Partitioning of Ti, Al, P, and Cr between olivine and a tholeiitic basaltic melt: Insights on olivine zoning patterns and cation substitution reactions under cooling rate conditions

Table of content - Chapter 4

Abstract 113

1. Introduction 114

2. Experimental and analytical techniques 116

3. Results 118
   - 3.1. Olivine textural and compositional changes as a function of cooling rate 118
   - 3.2. Olivine zonation 122
   - 3.3. Melt compositional variation 125
   - 3.4. Fe-Mg exchange between olivine and melt 127

4. Discussion 128
   - 4.1. Ti, Al, P, and Cr partitioning between olivine and tholeiitic basaltic melt 128
   - 4.2. Influence of melt and olivine chemistry on Ti, Al, P, and Cr partitioning 132

5. Conclusions 138

Acknowledgments 139

Supplementary Materials 140

References – Chapter 4 144

Chapter 4

Partitioning of Ti, Al, P, and Cr between olivine and a tholeiitic basaltic melt: Insights on olivine zoning patterns and cation substitution reactions under cooling rate conditions

Article

Article under review in *Chemical Geology*.

Lang Sarah[1,2], Silvio Mollo[1,3], Lydéric France[2], Valeria Misiti[3], and Manuela Nazzari[3]. " Partitioning of Ti, Al, P, and Cr between olivine and a tholeiitic basaltic melt: Insights on olivine zoning patterns and cation substitution reactions under cooling rate conditions" submitted to Chemical Geology

[1]Department of Earth Sciences, Sapienza - University of Rome, P. le Aldo Moro 5, 00185 Roma, Italy

[2]Université de Lorraine, CNRS, CRPG, F-54000 Nancy, France

[3]Istituto Nazionale di Geofisica e Vulcanologia - Department Roma 1, Via di Vigna Murata 605, 00143 Roma, Italy

Abstract

The mechanism governing the kinetic growth of olivine in dynamic volcanic settings has been the subject of considerable attention in recent years. Under variable cooling rate (*CR*) and undercooling ($-\Delta T$) regimes, the textual maturation of olivine proceeds from skeletal/dendritic crystals to polyhedral morphologies by infilling of the crystal framework. Owing to the establishment of a diffusion-controlled growth regime, a sharp diffusive boundary layer develops in the melt next to the advancing olivine surface. In this perspective, we have quantified the apparent partitioning of Ti, Al, P, and Cr between olivine and a Hawaiian tholeiitic basaltic melt at P = 1 atm, fO_2 = QFM-2 buffer, and CR = 4, 20, and 60 °C/h over a constant $-\Delta T$ = 85 °C. Differences in charge and/or size between the substituent minor cations and the major species in the olivine crystallographic site dominate the energetics of homovalent and heterovalent cation substitutions. While the entry of Ti in the olivine lattice site accounts for the simple exchange $[^{T}Si^{4+}] \leftrightarrow [^{T}Ti^{4+}]$, more complex charge-balancing coupled-substitution mechanisms have been determined for the incorporation of Al, P, and Cr, i.e., $[^{M}Mg^{2+}, ^{T}Si^{4+}] \leftrightarrow [^{M}Al^{3+}, ^{T}Al^{3+}]$, $[2\ ^{T}Si^{4+}] \leftrightarrow [^{T}P^{5+}, ^{T}Al^{3+}]$, and $[^{M}Mg^{2+}, ^{T}Si^{4+}] \leftrightarrow [^{M}Cr^{3+}, ^{T}Al^{3+}]$, respectively. In order to maintain charge balance, the disequilibrium uptake of minor cations in rapidly growing crystals is controlled by the same substitution mechanisms observed under equilibrium crystallization. This finding is consistent with the achievement of a local interface equilibrium at the olivine-melt interface independently of the diffusive boundary layer in the melt. A statistical approach based on multivariate analysis of olivine/melt compositional parameters confirms that the control of melt structure on the partitioning of Ti, Al, P, and Cr is almost entirely embodied in the crystallochemical change of olivine. Therefore, the magnitude of minor element partition coefficients is weakly dependent on diffusion kinetics in the melt but rather strongly governed by olivine zoning patterns resulting from fast crystal growth rates.

Keywords: kinetic partitioning; olivine rapid growth; cooling rate; Hawaiian tholeiitic basalt; charge-balance cation substitutions.

1. Introduction

As for the case of clinopyroxene and plagioclase, olivine is an important constituent of mafic magmas crystallizing and differentiating from upper mantle to shallow crustal storage regions (Putirka, 2017). A thorough understanding of the mechanisms controlling the partitioning of major, minor, and trace cations between olivine and basaltic melt is fundamental to quantitatively model the early stage of magma generation and differentiation. Substantial progress in this understanding has been made in half a century by equilibrium partitioning studies carried out at P-T-X-fO_2 conditions variable from the upper mantle to shallow crust (e.g., Roeder and Emslie, 1970; Purton et al., 1997; Taura et al., 1998; O'Neill and Eggins, 2002; Bedard, 2005; Hermann et al., 2005, Evans et al., 2008; Wang and Gaetani, 2008; Grant and Wood, 2010; Sun and Liang, 2013; Jollands et al., 2016; Sossi and O'Neill, 2016; Di Stefano et al., 2019, 2020).

Several works have also highlighted that the textural evolution and zoning patterns of natural olivine phenocrysts from active volcanoes are mostly the result of kinetic growth processes caused by temperature changes under variable cooling rates (*CR*) and degrees of undercooling ($-\Delta T = T_{liquidus} - T_{final}$; Milman-Barris et al., 2008; Faure et al., 2003, 2007; Welsch et al., 2009, 2013, 2014; Maaloe, 2011; Shea et al., 2015; 2019; Mourey and Shea, 2019; First et al., 2020; Lang et al., 2021). In the experimental work of Faure et al. (2003) that considers simplified CMAS ($CaO–MgO–Al_2O_3–SiO_2$) compositions, olivine develops a dendritic habit for any $CR \geq 47$ °C/h. 2D crystal growth measurements indicate that the olivine habit systematically changes as function of $-\Delta T$, from dendritic ($-\Delta T > 60$ °C) to skeletal ($-\Delta T = 20$-60 °C) to polyhedral ($-\Delta T < 20$ °C) morphologies (Faure et al., 2003). In the more recent study of Mourey and Shea (2019) that considers a natural tholeiitic basalt composition, 3D microtomography analysis reveals that hopper-to-skeletal olivine phenocrysts develop at $-\Delta T = 25$-60 °C and a maturation time exceeding 18 h. This implies that temperature changes in active volcanic settings may effectively produce hopper-to-skeletal olivine phenocrysts via mixing of chemically and thermally distinct magmas (Mourey and Shea, 2019). Alternatively, the kinetic growth of olivine can be promoted by temperature gradients and thermal convection in magma chambers (Faure et al., 2003; Welsch et al., 2013). The melt superliquidus thermal history may also contribute to the early morphologic instability of olivine as the result of delay in nucleation and structural relaxation phenomena (First et al., 2020).

There is general consensus that olivine crystallization is a rapid process in dynamic systems and the formation of large olivine phenocrysts is controlled by an initial disequilibrium stage where a diffusion-controlled growth regime leads to the fast development of dendrites with an early skeletal habit (Welsch et al., 2013, 2014; Shea et al., 2015). Dendrites may ripen towards a polyhedral habit by filling the hopper cavities into replete faces (i.e., infilling of the crystal framework) under the effects of continuous magma cooling and/or successive cooling-heating cycles (Faure et al., 2003; Welsch et al., 2013, 2014; Shea et al., 2015; Wallace et al., 2021). The early rapid growth of olivine promotes a strong disequilibrium uptake of P, Cr, Na, Al, and Ca cations in the lattice site under conditions of high supersaturation (Pack and Palme, 2003; Milman-Barris et al., 2008; Welsch et al., 2013, 2014; Shea et al., 2015; First et al., 2020). How apparent olivine-melt partition coefficients change under kinetic growth conditions has been also the matter of several studies (Kennedy et al., 1993; Pack and Palme, 2003; Sossi and O'Neill 2016; Mollo and Hammer, 2017; Shea et al., 2019; Lang et al., 2021). However, the strong codependency between olivine crystallochemistry and the melt composition/structure has been poorly investigated for the kinetic partitioning of cations (e.g., Snyder and Carmichael, 1992; Gaetani, 2004; Mysen, 2004).

Here, we present results from olivine-melt partitioning experiments carried out on a Hawaiian tholeiitic basalt cooled at rates encountered by magmas in naturally solidifying settings (e.g., Ujike, 1982; Hammer, 2008; Mollo et al., 2011; Vetere et al., 2015; Giuliani et al., 2020). A constant -ΔT of 85 °C was imposed to all the experimental charges to promote the skeletal/dendritic growth of olivine at *CR* of 4, 20, and 60 °C/h. Focusing on the kinetic partitioning of Ti, Al, P, and Cr, charge balance mechanisms and cation substitution reactions have been evaluated for rapidly growing olivine crystals. Such information may be an aid in determining to what extent naturally solidifying basaltic systems may deviate from close equilibrium in volcanic settings.

2. Experimental and analytical techniques

A detailed description of the experimental and analytical conditions used in this study can be found in Lang et al. (2021). Hence, we report here only the most important experimental and analytical aspects.

Table 4.1. *Composition of the starting material, olivine crystals and residual glasses. Fe-Mg exchange calculated for olivine core with FFM and olivine rim with IM.*

Run product	Starting	CR4				CR20				CR60			
Phase	material	Ol_core	FFM	Ol_rim	IM	Ol_core	FFM	Ol_rim	IM	Ol_core	FFM	Ol_rim	IM
n=													
SiO_2	47.28	38.83	52.21	39.02	52.83	39.07	50.30	38.60	51.12	38.85	50.02	38.50	51.06
TiO_2	2.18	0.14	2.58	0.14	2.50	0.17	2.53	0.16	2.48	0.16	2.51	0.22	2.49
Al_2O_3	11.64	0.18	14.20	0.15	14.73	0.18	13.82	0.17	14.54	0.17	13.69	0.19	14.53
FeO_t	16.03	13.28	6.51	14.14	6.04	17.23	9.15	19.22	8.54	16.78	9.44	18.74	8.92
MnO	0.18	0.31	0.26	0.33	0.23	0.30	0.24	0.34	0.23	0.28	0.25	0.33	0.23
MgO	10.95	45.72	7.38	45.03	6.61	42.88	6.94	41.28	6.22	43.23	7.07	41.68	6.25
CaO	9.33	0.34	11.35	0.39	11.07	0.40	11.04	0.47	10.82	0.43	11.11	0.50	10.99
Na_2O	1.91	0.02	2.53	0.02	2.71	0.02	3.39	0.02	3.43	0.02	3.84	0.02	3.67
K_2O	0.39	0.00	0.67	0.01	0.79	0.01	0.44	0.01	0.53	0.00	0.47	0.01	0.55
P_2O_5	0.22	0.31	0.34	0.31	0.35	0.19	0.42	0.17	0.41	0.29	0.42	0.26	0.42
Cr_2O_3	0.21	0.57	0.13	0.58	0.12	0.51	0.12	0.53	0.11	0.47	0.13	0.55	0.11
Total	100.31	99.70	98.14	100.12	97.97	100.95	98.41	100.96	98.43	100.69	98.96	100.98	99.23
$K^{Fe\text{-}Mg}$ *		0.33		0.34		0.30		0.34		0.29		0.32	

* according to Putirka et al. 2016, the Fe-Mg equilibrium of the system is reached at $Kd^{Fe\text{-}Mg} = 0.33 \pm 0.04$

The starting material (Table 4.1) used for this work is a powdered glass obtained from a basaltic tholeiitic pumice from the 1820 CE eruption of Kilauea (Garcia et al., 2003; Lynn et al., 2017; Shea et al., 2019; Lang et al., 2021). The experiments were performed at the HP-HT Laboratory of Experimental Volcanology and Geophysics of the Istituto Nazionale di Geofisica e Vulcanologia (INGV), Rome, Italy, using a 1 atm vertical tube CO-CO2 gas-mixing furnace at the QFM-2 buffer. The liquidus temperature was determined at 1210 °C. We adopted a superliquidus treatment by keeping the temperature at 1250 °C for only 1 h, in order to minimize superheating effects (First et al., 2020). The charges were cooled at different rates of 4, 20, and 60 °C/h (i.e., *CR4*, *CR20*, and *CR60*, respectively) until the final target temperature of 1125 °C (i.e., $-\Delta T$ = 85 °C). Then, a rapid quench was imposed by dropping the samples into a water bath, and the recovered run products were mounted in epoxy and polished for in-situ chemical analyses.

Major and minor oxides in the olivine were carried out on a Jeol-JXA8200 electron micro-probe (EMP) analysis equipped with five spectrometers (see Supplementary Material 1). Data were collected using 20 keV accelerating voltage, 300 nA beam current and counting times were 40 (Si and Fe), 50 (Mg), and 120 (Ti, Al, Mn, Ca, Na, K, P, and Cr) seconds, also with half the peak times on the background. The same elements were analyzed in the glass, using 20 keV accelerating voltage, 20 nA beam current and counting times were 15 s (Na and K measured first to prevent migration effects), 30 s (Si, Fe, Mg, and Ca), and 60 s (Ti, Mn, and Cr), also with half of the peak times on the background. For both olivine and glass, several transects were performed across the crystal and from the crystal-melt interface to the far field melt using a 2 µm beam diameter and 2.5 µm step size. X-ray element maps of Si, Ti, Al, P, and Cr were collected in one selected experimental crystal using 20 keV, 300 nA, resolutions of 0.5 µm/pixel, with dwell times of 80 ms/pixel.

Photomicrographs were collected using the backscattered electron (BSE) mode of a field emission gun-scanning electron microscopy (FE-SEM) Jeol 6500F equipped with an energy-dispersive spectrometer (EDS) detector. BSE imaging combined with X-ray mapping were both adopted for the identification of the main textural and compositional features of each sample. X-ray maps were acquired by using 15 kV accelerating voltage, 8 nA probe current, resolution 1024 × 768 pixel^2, and dwell time 10 ms/pixel. Yellow and blue colours were assigned to single-band images from X-ray maps to form a coloured two-band image for FeO and MgO.

3. Results

3.1. Olivine textural and compositional changes as a function of CR

The morphological and chemical aspects of experimental olivines obtained from *CR* experiments are discussed in detail in Lang et al. (2021):

1) the olivine crystal size increases from ~250 μm to ~2 mm as the cooling rate decreases from 60 to 4 °C/h;

2) the olivine morphology at $-\Delta T = 85$ °C is characteristic of rapid growth conditions (i.e., $\sim 4 \times 10^{-9}$-10^{-8} m/s), ranging from hopper-skeletal (*CR4* and *CR20*) to dendritic (*CR60*) shapes (Figure 4.1a), in accordance with values of *CR* and $-\Delta T$ used by previous authors (Donaldson, 1976; Faure et al., 2003, 2007);

3) olivine crystals develop primary and secondary branches. Primary branches propagate from the crystal center (outlined in red in Figures 4.1b and 4.2). Secondary branches emerge from primary branches as planes growing parallel to the crystal face (outlined in green in Figures 4.1b and 4.2), also showing irregular spacing between each other. The early rapid growth of primary and secondary dendritic branches is followed by late-stage overgrowth and infilling episodes (Welsch et al., 2013);

4) olivine crystals are characterized by Fe-Mg continuous zoning with forsterite (Fo) contents on the order of Fo_{86} (core) – Fo_{84} (rim), Fo_{82} (core) – Fo_{78} (rim), and Fo_{83} (core) - Fo_{78} (rim) for *CR4*, *CR20*, and *CR60*, respectively (Figures 4.1c);

5) BSE imaging combined with FE-SEM X-ray mapping shows normal olivine zonation with Mg-rich, Fe-poor inner portions surrounded by Fe-rich, Mg-poor outer portions for *CR20* and *CR60* (Figure 4.3).

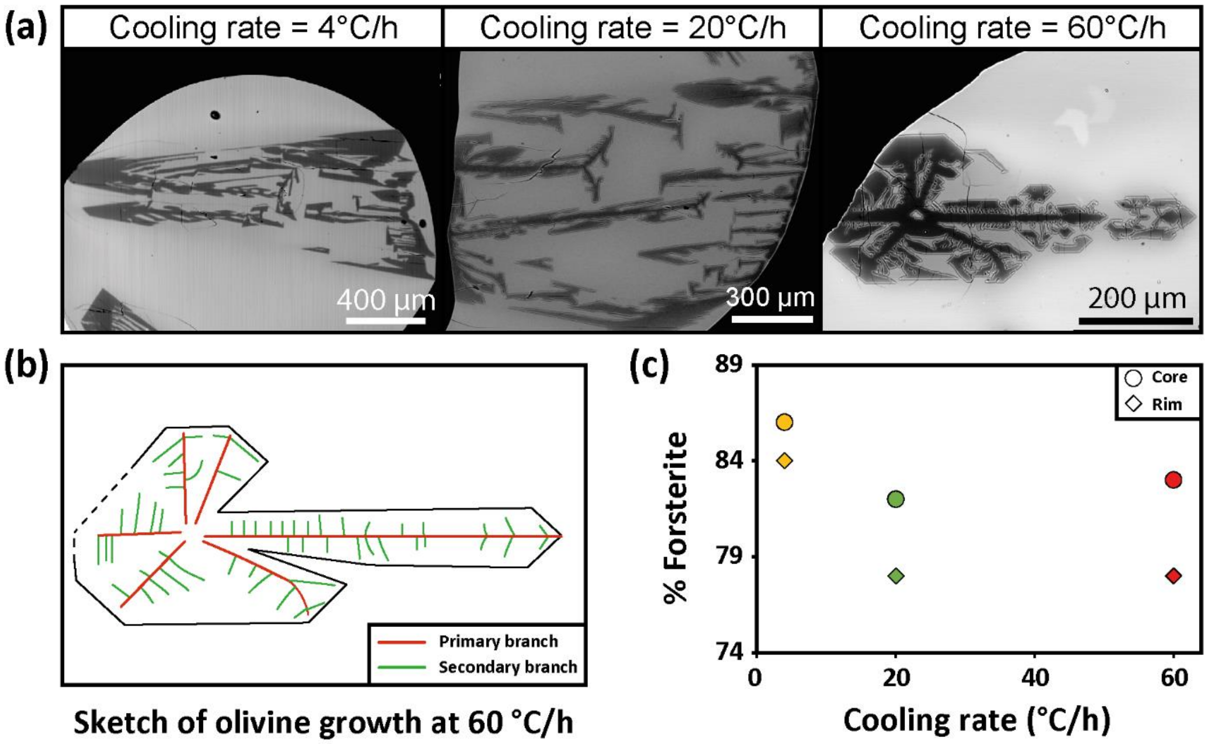

Figure 4.1. *(a) BSE (back-scattered electron) photomicrographs of olivine crystals with variable textural characteristics under the effect of cooling rate. (b) Schematic sketch of olivine obtained at cooling rate of 60 °C/h. Primary and secondary branches are represented by red and green lines, respectively. (c) Forsterite content in olivine as a function of cooling rate.*

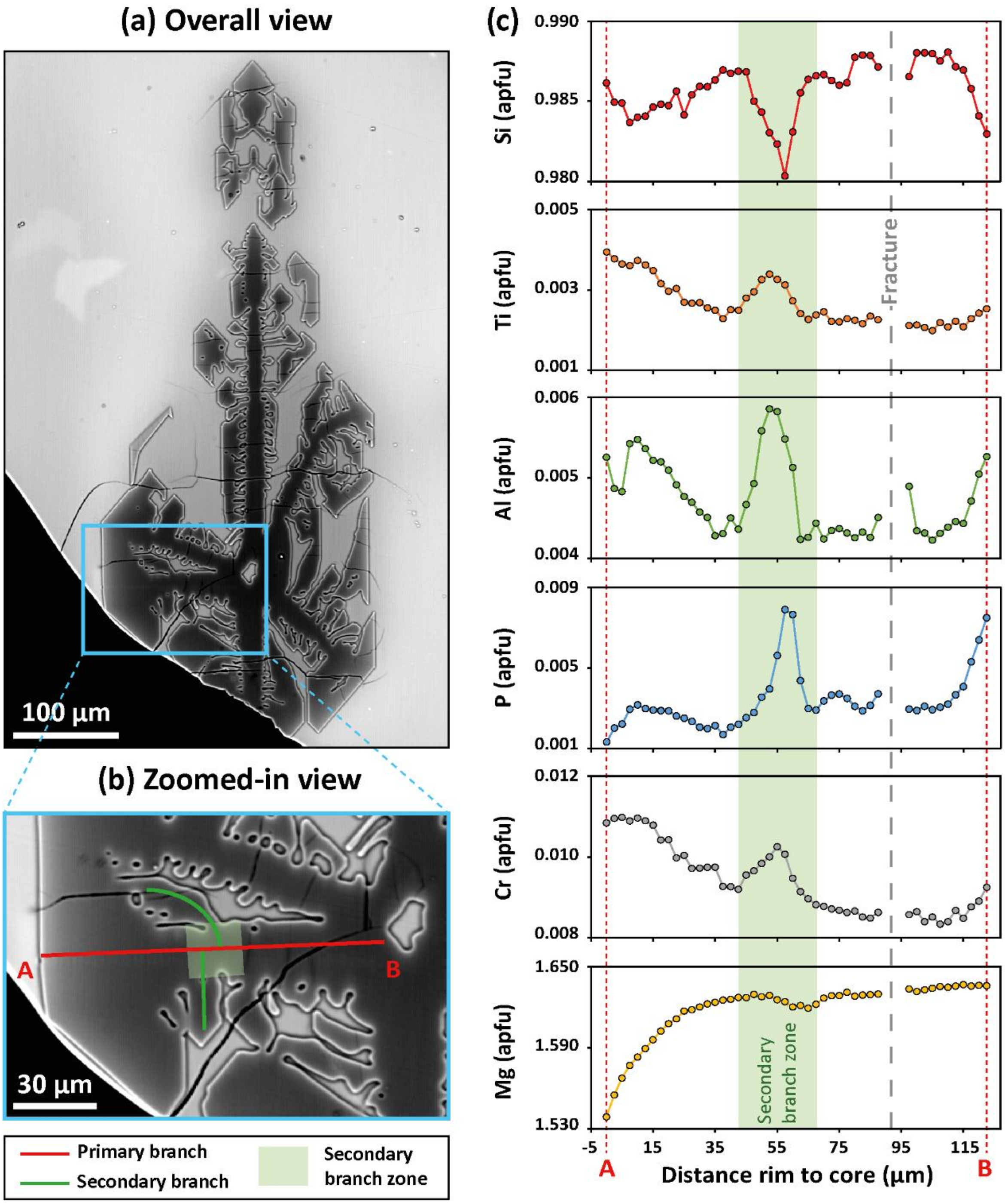

Figure 4.2. *(a) BSE (back-scattered electron) photomicrograph of olivine obtained at cooling rate of 60 °C/h; (b) Zoomed-in view showing primary (red line) and secondary (green line) olivine branches; (c) EMP (electron micro-probe) transect performed along the primary branch highlights a non-radial evolution of the cations concentration from rim to core. The main compositional changes are observed in the green sector of the transect, the "secondary branch zone" corresponding to a junction between primary and secondary branches.*

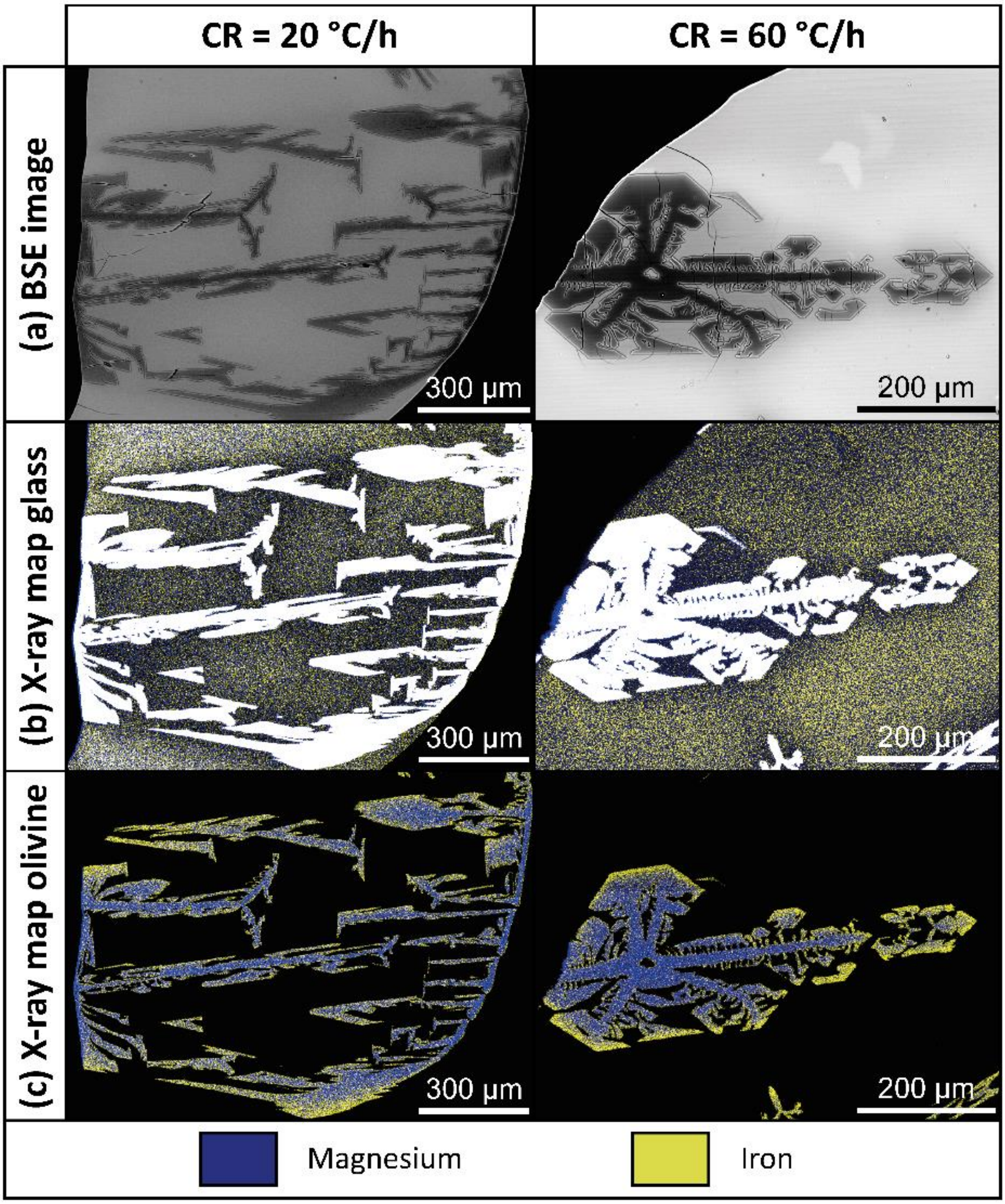
CR = 20 °C/h
CR = 60 °C/h
(a) BSE image
(b) X-ray map glass
(c) X-ray map olivine
300 µm
200 µm
300 µm
200 µm
300 µm
200 µm
Magnesium
Iron

Figure 4.3. *BSE (back-scattered electron) photomicrographs of experimental charges obtained at cooling rates of 20 and 60 °C. The figure shows also combined Fe-Mg X-ray maps with colour scales adjusted for the glass and crystal compositions.*

3.2. Olivine zonation

Chemical distribution of Si, Ti, Al, P, Cr, and Mg cations in olivine is investigated by rim to core transects. These cations are expressed as atoms per formula unit (apfu) recalculated on the basis of 4 oxygens. Figure 4.2a shows the overall view of the olivine analyzed in the *CR60* experiment. A zoomed-in view of one representative transect carried out along the primary branch is displayed in Figure 4.2b (see Supplementary Material 2 for additional data from *CR4* and *CR20*). Si, Ti, Al, and P cations in tetrahedral coordination show strong zonation, with peaks and troughs along the primary branch and also apparent enrichments of Al and Ti at the olivine rim (Figure 4.2c). In contrast, the concentration of octahedrally coordinated Mg smoothly decreases towards the rim (Figure 4.2c). At the intersection between primary and secondary branches, cation enrichments and depletions are observed along the chemical profile (Figure 4.2c). Specifically, zones of Si depletion (0.952-0.991 apfu), are counterbalanced by zones of Ti (0.002-0.005 apfu), Al (0.003-0.007 apfu), and P (0.001-0.010 apfu) enrichments. Cr follows the same trend (0.008-0.012 apfu) as tetrahedrally coordinated Ti, Al, and P. Within an individual analytical transect, the enrichment sequence is P > Ti > Al > Cr, with maximum factors of ×6.0, ×1.9, ×1.4, ×1.3, respectively (Figure 4.2c). Given that crystal sectioning matters greatly in determining the measured element concentrations (i.e., 3D crystal morphology vs. 2D thin section plan), there is strong crystal heterogeneity, and no substantial changes can be detected between *CR4*, *CR20*, and *CR60*. The only exception is represented by the slight increase of Si and decrease of Cr with increasing *CR*.

Figure 4.4 shows EMP X-ray maps of Ti, Al, P, Cr, and Si in an olivine branch from the *CR60* experiment where colour scales were adjusted to highlight intracrystalline cation changes. Ti, Al, P, and Cr enrichments depict zoning patterns that are characteristically very similar to those documented in literature (Milman-Barris et al., 2008; Sakyi et al., 2012; Welsch et al., 2013, 2014; Shea et al., 2019). High-concentration zones appear as thin lineations in both primary and secondary branches. Major lineations emerge early from the crystal core (see red lines in Figure 4.1b) and, subsequently, develop within the primary branch (Figure 4.4). On the other hand, secondary branches growth from primary branches (see green lines in Figure 4.1b), mainly as heterogeneous ramifications oriented parallel to the outermost rim (Figure 4.4).

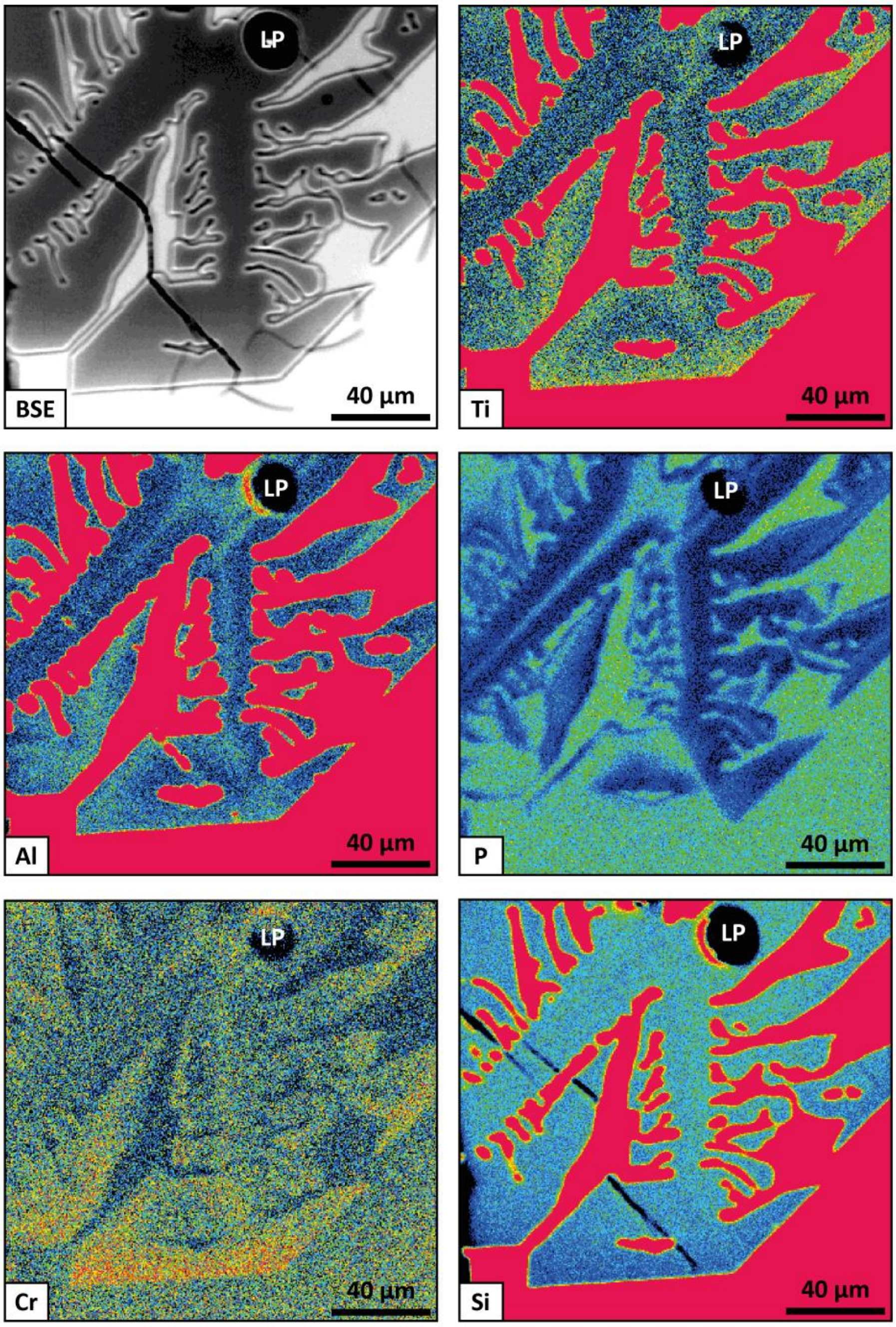

Figure 4.4. Olivine zonation obtained at cooling rate of 60 °C/h. The panels show a BSE photomicrograph and X-ray maps of Ti, Al, P, Cr, and Si with colour intensities adapted for crystal concentrations. Fine-scale enrichments are displayed for P, Ti, Al, and Cr, as minor cations in olivine. Conversely, subtle depletions are observable for Si, as major cation hosted in the lattice site. LP: laser pit.

EMP transects of P displayed in Figure 4.5a are used to localize concentration gradients occurring along the profiles (i.e., from peaks to troughs) during olivine growth. These selected subsets are plotted in Figures 4.5b together with the remaining data set. Data selection is essential to minimize any effect resulting from the scattering of data and to better define the compositional changes in the lattice site. According to this interpretation, FE-SEM X-ray maps show that olivine dendrites are mantled by diffusive boundary layers (Figure 4.3b) that may impinge upon one another as crystallization proceeds. Diffusion effects may extend completely across the melt regions among growing primary and secondary branches so that each single branch competes with its near neighbors for chemical nutrients. This competitive-diffusion mechanism causes olivine intracrystalline zonation (Figure 4.3c) and scattering of data during EMP analysis. As a consequence, zonation is more intense where branches cluster in close proximity to one another but is less intense where dendrites are relatively widely and evenly spaced. Through this approach, we observe that the sum of Ti, Al, and P linearly decreases with increasing Si (Figure 4.5b) and the regression analysis returns very good coefficients of determination ($^{CR4}R^2$ = 0.93, $^{CR20}R^2$ = 0.99, and $^{CR60}R^2$ = 0.95). P and Cr, by contrast, are positively correlated with Al (Figure 4.5b), returning appreciable regression statistics ($^{CR4}R^2$ = 0.89, $^{CR20}R^2$ = 0.90, and $^{CR60}R^2$ = 0.82 for P and $^{CR4}R^2$ = 0.98, $^{CR20}R^2$ = 0.97, and $^{CR60}R^2$ = 0.92 for Cr).

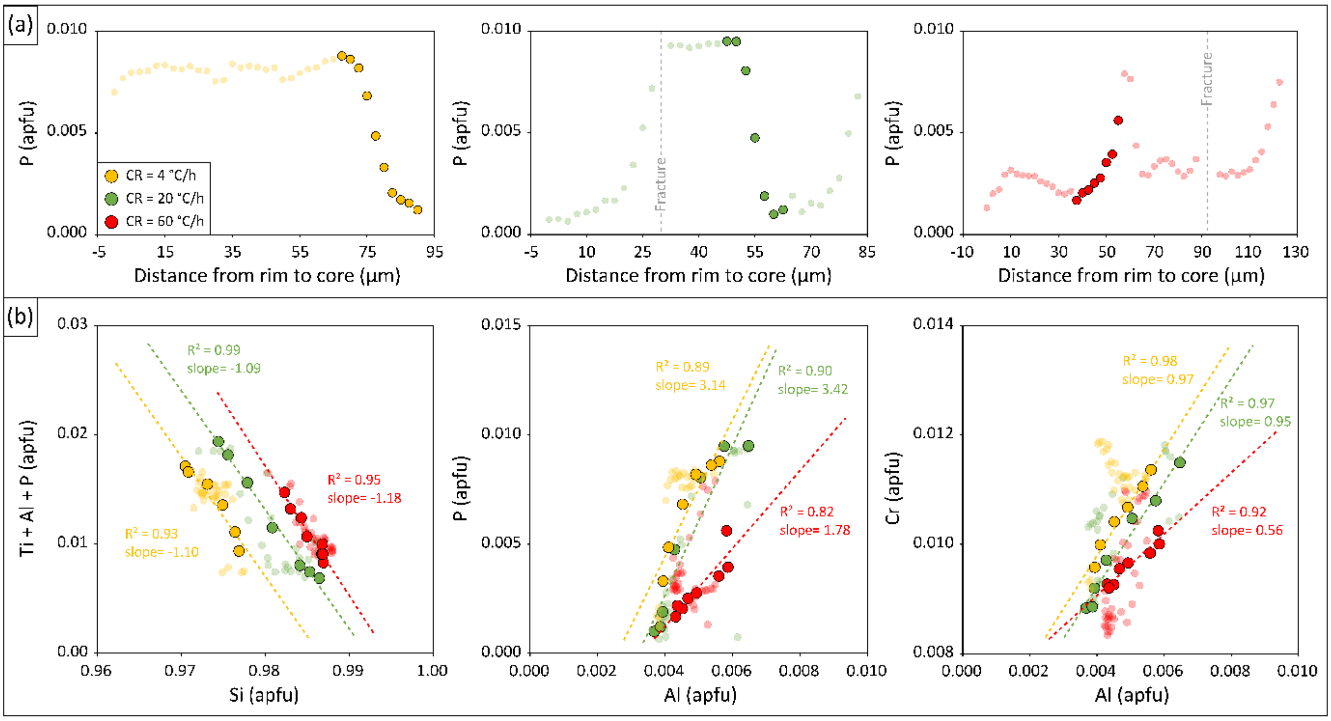

Figure 4.5. *(a) Sum of Ti, Al, and P vs. Si in olivine. (b) P vs. Al in olivine. (c) Cr vs. Al in olivine. Regression lines and coefficients of determination (R²) are reported for each cooling rate experiment.*

3.3. Melt compositional variation

The overall residual melt composition changes as a function of cooling effects (Lang et al., 2021) and one of the most important changes consists of the progressive decrease of ^{melt}Mg# [Mg-number of melt = $^{melt}X_{Mg}$ / ($^{melt}X_{Mg}$ + $^{melt}X_{Fetot}$)] from ~64 to ~53 with increasing *CR*.

Strong chemical gradients occur also in the melt surrounding the advancing olivine surface. This compositional change leads to the development a diffusive boundary layer (BL), in which the interface melt (IM) is compositionally distinct from the far field melt (FFM). For example, Figure 4.6 shows a representative analytical transect performed from IM towards FFM for the *CR60* experiment (see Supplementary Material 3 for additional data from *CR4* and *CR20*). IM is depleted by up to ~9% in TiO_2 and enriched by up to ~3% SiO_2 and ~8% in Al_2O_3. No clear trends are measured for P_2O_5 and Cr_2O_5, showing concentrations from IM to FFM in the ranges of 0.34-0.46 wt.% and 0.11-0.14 wt.%, respectively. However, considering the resolution limits of EMP transects and their analytical precisions for P (~15%) and Cr (~10%) in the glass, we cannot completely exclude weak enrichments of these cations at the crystal interface. Additionally, owing to the complex morphology of olivine, the diffusive length scale is strongly variable around each single crystal, attaining a maximum thickness of 120 µm. Accumulation or depletion of melt components may be also determined by impingement of distinct diffusion fields of nearby crystal branches (see for example the length scale of diffusion haloes in Figure 4.3b).

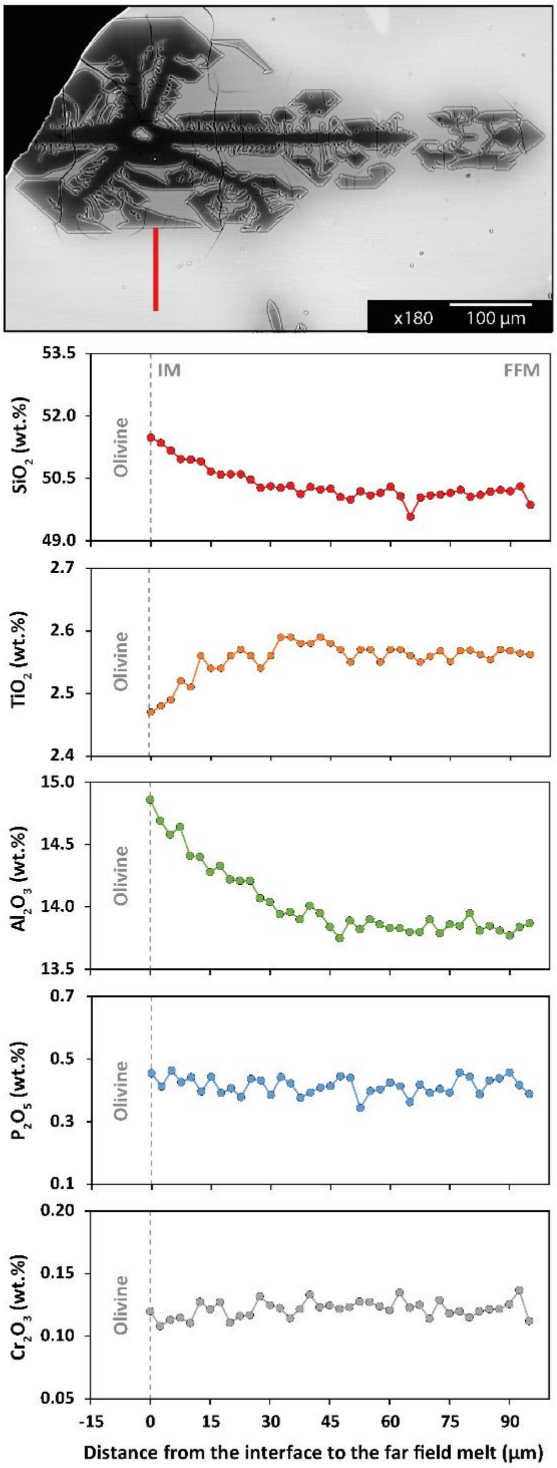

Figure 4.6. *Melt zonation obtained at cooling rate of 60 °C/h. The red line displayed in the BSE (back-scattered electron) photomicrograph corresponds to the analytical transect performed in the glass surrounding olivine. EMP (electron micro-probe) analytical profiles highlight the presence of a diffusive boundary layer, extending from the interface melt (IM) to the far-field melt (FFM).*

3.4. Fe-Mg exchange between olivine and melt

The equilibrium of the system is one of the most important aspects to be considered in measuring the partitioning of cations between minerals and melts. This is especially true for kinetic crystallization experiments, where the degree of CR and/or $-\Delta T$ may deviate significantly the incorporation of major cations from equilibrium proportions (Mollo et al., 2012).

Roeder and Emslie (1970) determined that the Fe-Mg exchange [$Kd_{(Fe-Mg)} = ({}^{ol}X_{Fetot} / {}^{ol}X_{Mg}) / ({}^{melt}X_{Fetot} / {}^{melt}X_{Mg})$] between equilibrium olivine and melt remains almost constant and close to 0.27-0.33, over a broad range of temperature, oxygen fugacity, and bulk (crystal + melt) composition. Falloon et al., (2007) constrained the olivine-melt equilibrium for both MORB and OIB systems at $Kd_{(Fe-Mg)}$ = 0.28-0.38. For the specific case of OIB compositions, Matzen et al. (2011) found equilibrium crystallization at values of 0.34-0.36. In the most recent review study of Putirka (2016), 1270 experiments from the literature were critically reappraised in order to derive a global Fe-Mg range of 0.29-0.37 for both terrestrial and extraterrestrial magmas.

According to the above considerations, Lang et al. (2021) calculated values of $Kd_{(Fe-Mg)}$ for the present kinetic experiments by considering 1) the olivine core and FFM, as proxy of the less differentiated melt composition feeding the early growth of olivine across the liquidus region, and 2) the olivine rim and IM, as a proxy for cation exchange reactions taking place at the crystal-melt interface. Results from these calculations return $Kd_{(Fe-Mg)}$ values of 0.29-0.34 (Table 4.1), which are in close agreement with the equilibrium ranges derived by previous studies. This observation is consistent with the relatively simple structure of the main olivine forsterite/fayalite end-members (i.e., $(Mg, Fe)_2SiO_4$ with a very weak cation ordering between Fe and Mg) and the achievement of a local interface equilibrium (i.e., equilibrium of a reaction in a small volume) due to a steady-state diffusive mass transport in high-temperature, low-viscosity basaltic melts (Lang et al., 2021).

4. Discussion

4.1. Ti, Al, P, and Cr partitioning between olivine and tholeiitic basaltic melt

Apparent partition coefficients ($Kd_i^{ol-melt} = C_i^{olivine}/C_i^{melt}$) representative of the variance of our experimental data set have been calculated between olivine and residual melt for titanium (Kd_{Ti}), aluminium (Kd_{Al}), phosphorus (Kd_P), and chromium (Kd_{Cr}). $C_i^{olivine}$ refers to the selected subsets displayed in Figure 4.5 (see also Supplementary Material 1 for the overall data set). According to Lang et al. (2021), diffusive mass transport of cations in our experiments occurred under the conditions of local equilibrium at the olivine surface. Therefore, in the present study, C_i^{melt} corresponds to the IM analysis, in order to consider only the composition of the melt next to the crystal surface and feeding the growth of primary and secondary branches. However, following the same approach used by Shea et al. (2019), we also recalculated the apparent partition coefficient using FFM composition. By comparing partition coefficients calculated with both methods, we observe $Kd_i^{ol-melt}$ variations in the order of 3-9%, 4-7%, 1-7%, and 1-9% for Ti, Al, P, and Cr, respectively. These minimum changes denote that the melt composition does not greatly impact the partitioning of cations (see discussion at §4.2).

Figure 4.7 shows that $\ln Kd_{Ti}$, $\ln Kd_{Al}$, and $\ln Kd_P$ decrease with increasing Si in olivine, whereas $\ln Kd_{Cr}$ increases with increasing Al (note that error bars are within the symbols). Moreover, all partitioning data depict sub-parallel trends with statistically significant R^2 values and almost similar slopes (Figure 4.7). This suggests that the mechanism controlling the incorporation of cations does not change with increasing *CR*, also in agreement with the systematic negative correlation between Ti + Al + P and Si in tetrahedral coordination (Figure 4.5a).

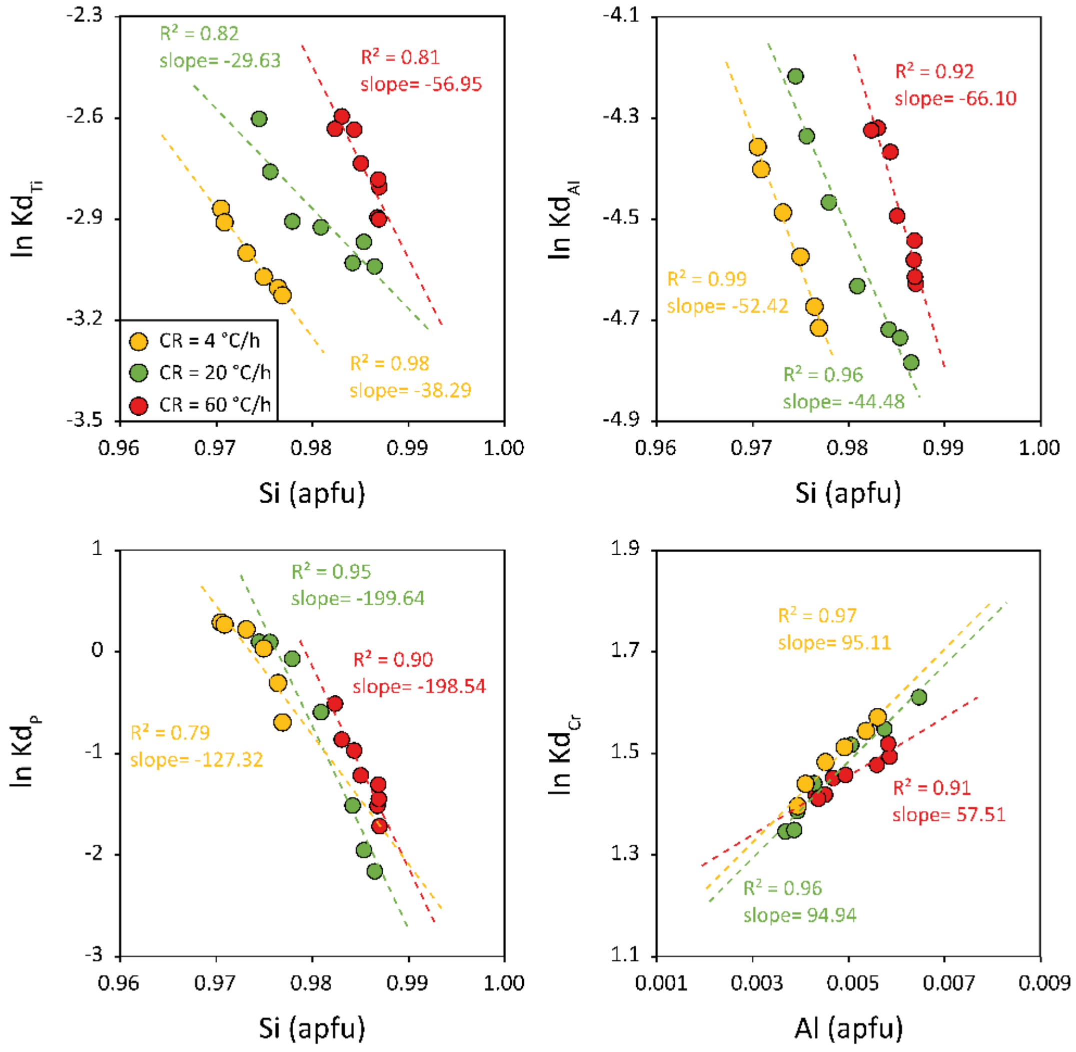

Figure 4.7. *Scatter plots showing the partition coefficient of Ti, Al and P vs. Si in olivine, and the partition coefficient of Cr vs. Al in olivine. Regression lines and coefficients of determination (R^2) are reported for each cooling rate experiment.*

According to Hermann et al. (2005), pressure has no effect on Ti incorporation in olivine and, for a given paragenesis, the amount of Ti in the lattice site increases remarkably with increasing temperature. Hermann et al. (2005) have also documented that Ti substitutes for Si on the tetrahedral site to produce the Mg_2TiO_4 component. This substitution mechanism accounts for the negative correlation between Ti and Si (Figure 4.5a) and the absence of correlation between Ti and Mg (cf. Jollands et al., 2016). Data from this study support this corollary and extend its applicability to the skeletal/dendritic growth of olivine under variable *CR* conditions. Through the interpretation of XANES and EXAFS spectra of anhydrous forsterite, Berry et al. (2007) determined that the solution energy of Ti occupying the M-site (>

2.0 eV) is about twice as high the energy measured for the T-site (0.98 eV). Moreover, the systematic change of unit cell volume with increasing Ti is more consistent with tetrahedrally-coordinated cations (i.e., Ti–O bond length of 1.81±0.01 Å; Berry et al., 2007). This excludes substantial expansion of olivine unit cell caused by larger octahedrally-coordinated cations (i.e., Ti–O bond length of 2.0 Å; Berry et al., 2007). Therefore, substitution of Ti for Mg charge-balanced by vacancy is energetically unfavored relative to direct substitution of Ti for Si, as expressed by the simple exchange:

$$[{}^{T}Si^{4+}] \leftrightarrow [{}^{T}Ti^{4+}] \qquad \text{Eqn.(1)}$$

It is also widely accepted that Al substitutes into olivine by the coupled substitution of 2 Al for Mg + Si (Tschermak-style substitution; Evans et al. 2008; De Hoog et al., 2010; Grant and Wood, 2010; Coogan et al., 2014; Di Stefano et al., 2019). Accordingly, half the Al substitutes for octahedral Mg and is charge-balanced by the other half substituting for tetrahedral Si:

$$[{}^{M}Mg^{2+}, {}^{T}Si^{4+}] \leftrightarrow [{}^{M}Al^{3+}, {}^{T}Al^{3+}] \qquad \text{Eqn.(2)}$$

Although a general principle stoichiometry can never give site occupancies unambiguously, Al is inferred to occupy both the octahedral and tetrahedral sites due to a high degree of short-range order between them (Evans et al., 2008). The antithetic correlation between $\ln Kd_{Al}$ and Si in olivine (Figure 4.7) confirms the efficacy of the Tschermak-style substitution via the formation of $MgAl_2O_4$ component. This is also facilitated by the ionic radius (r) of different cations, given that r_{Al} (0.39 Å and 0.535 Å and in T- and M-sites, respectively) is roughly in-between r_{Si} (0.26 Å) and r_{Mg} (0.72 Å) (Evans et al., 2008; Zhukova et al. 2017).

There is no theoretical reason for the substitution of cations into the lattice site of olivine to occur just by one single mechanism only. Zhukova et al. (2017) have proposed that the incorporation of Al accounts for the formation of an “octahedral-site, vacancy-coupled component” (i.e., OSVC) which has the stoichiometry of $Al_{4/3}vac_{2/3}SiO_4$. According to Evans et al. (2008) and Zhukova et al. (2017), the stability of $MgAl_2O_4$ and OSVC requires that $C_{Al}^{olivine}$ is proportional to $\sqrt{C_{Al}^{melt}}$ and C_{Al}^{melt}, respectively. However, we do not observe any proportionality between the concentration of Al in olivine and the melt composition (i.e., $R^2 = 0.1$ for both $\sqrt{C_{Al}^{melt}}$ and C_{Al}^{melt}). It is therefore postulated that the mechanism governing the incorporation of cations in tetrahedral coordination is mainly dictated by crystallochemical effects related to structural rearrangements in the lattice site of olivine. Pack and Palme (2003) present cooling rate experiments (i.e., from 1.5 to 1000 °C/h) in the CMAS system to determine the partitioning of Al between forsterite and melt. At *CR* = 1000 °C/h, Al in the melt significantly increases towards the forsterite interface in a fashion similar to that observed in Figure 4.6. However, no systematic trend of Kd_{Al} with *CR* is noted by Pack and Palme (2003) due to the temperature dependence of Al partitioning, in conjunction with the complex zoning pattern of forsterite. This intra-crystalline variability corroborates the hypothesis of a strong crystallographic site control on Kd_{Al}. Moreover, the positive correlation between P and Al ($R^2 = 0.82$-0.90) displayed in Figure 4.5b points to a local charge balance mechanism in which 2 Si are replaced by P + Al via the coupled substitution:

$$[2\ {}^{T}Si^{4+}] \leftrightarrow [{}^{T}P^{5+},\ {}^{T}Al^{3+}] \qquad \text{Eqn.(3)}$$

From a crystallochemical point of view, coupled substitutions in mafic phases are energetically more favored than the vacancy reactions for insertion of minor/trace cations into the crystallographic sites of minerals (e.g., Purton et al., 1997; Pinilla et al., 2012). Therefore, the entry of P in the lattice site of olivine by heterovalent substitution and charge compensation with Al is considerably lower in energy than vacancy compensation in tetrahedral or octahedral sites. Since r_P (0.17 Å) < r_{Al} (0.39 Å) in tetrahedral coordination, it is also not excluded that P can be preferentially incorporated over Al under kinetic growth conditions (Shea et al., 2019). A rapid growth of olivine could produce a slightly less stiff lattice, which facilitates the incorporation of smaller P cations compared to the larger Al ones (Shea et al., 2019). This mechanism may be a reasonable explanation for the higher magnitude of Kd_P relative to Kd_{Al} (Figure 4.7), in agreement with lattice strain modeling data of Shea et al. (2019), derived at $-\Delta T$ = 10-60 °C using the same Hawaiian tholeiitic basalt from this study. The coupled substitution of Eqn. (3) is also supported by the fact that P is smaller in size and higher in charge than both Al and Si, thus limiting the role of crystal interface in controlling the cation uptake (Pinilla et al., 2012). Crystal interfaces are lattice discontinuities associated with various types of defects, such as free surfaces, boundaries, voids, and channels both inter- and intra-crystalline. Computational simulations carried out on forsterite quantify the energetics of such crystal interfaces (Pinilla et al., 2012). Positive interface segregation energies favoring interface depletion, are prevalently associated with cations smaller in size and/or higher in charge than the host cation (Pinilla et al., 2012). Therefore, the small size and high charge of P render adsorption at the interface much less favorable than bulk incorporation via the coupled substitution proposed by Eqn. (3).

Cr as aliovalent cation exists in natural olivine in two oxidation states: trivalent cations dominate in terrestrial systems (Bell et al., 2014), whereas divalent cations occupy the lattice site of meteoritic and lunar olivines (Sutton et al., 1993; McKeown et al., 2014). Cr in both divalent and trivalent speciation has a preference for the octahedral site of olivine due to strong crystal field effects (Burns, 1976; Papike et al., 2005; Jollands et al., 2018). However, looking at compositional data from this study, the trend of Cr mimics the same patterns of tetrahedrally-coordinated Ti, Al, and P in olivine (Figures 4.2c and 4.4). This dichotomy accounts for a Tschermak-style substitution in which replacement of Si by Al in the T-site is charge-balanced by replacement of Mg with Cr in the M-site (Bershov et al., 1983). As a result, both Cr content in olivine ($R^2 = 0.92\text{-}0.98$; Figure 4.5c) and $\ln Kd_{Cr}$ ($R^2 = 0.91\text{-}0.97$; Figure 4.6) systematically increase with Al, in response to the following exchange reaction (Taura et al., 1998):

$$[{}^{M}Mg^{2+}, {}^{T}Si^{4+}] \leftrightarrow [{}^{M}Cr^{3+}, {}^{T}Al^{3+}] \qquad \text{Eqn.(4)}$$

Bearing in mind that $r_{Al} > r_{Si}$ and $r_{Cr} < r_{Mg}$, the T-site hosting Al will expand towards the M-site occupied by Cr, causing compaction of the M-site. At pressure ≤3 GPa, these local modifications in the crystal structure will stabilize the Tschermak-style substitution described by Eqn. (4) (Taura et al., 1998).

4.2. Influence of melt and olivine chemistry on Ti, Al, P, and Cr partitioning

It is widely known that the partitioning of major, minor, and trace cations between olivine and coexisting melt depends on the bulk chemistry of the system, including both mineral and melt compositional variations as a function of the intensive *P-T* parameters (e.g., O'Neill and Eggins, 2002; Gaetani, 2004; Mysen, 2004; Evans et al., 2008; Di Stefano et al., 2018, 2019). While minor and trace elements are likely to compete with major melt components for available structural positions, there is a close relation between major element composition and melt structure. Indeed, melt compositional effects on element partitioning may reflect the concentration behaviour of the cations in the melt and their structural interactions (Mysen, 2004; Evans et al., 2008; Di Stefano et al., 2019). As the melt becomes less polymerized, the number of bridging oxygens (i.e., ${}^{melt}BO$, oxygens bonded to two tetrahedrally coordinated cations) decreases, whereas the amount of non-bridging oxygens (i.e., ${}^{melt}NBO$, oxygens bonded to a tetrahedrally coordinated cation and to a different cation in another coordination state) increases. Therefore, the melt structure is frequently expressed through the value of ${}^{melt}NBO/T$, which refers to the number of ${}^{melt}NBO$ per tetrahedrally coordinated cations T (i.e., ${}^{melt}NBO/T$ =

[2 × total oxygens / (Si + Al + P) in mole proportions] – 4; Mysen, 2004). An alternative parameter to represent the degree of polymerization is also the optical basicity ($^{melt}\Lambda$), which represents the electron donor power of oxygen as a function of the nature of the ligand cation (Duffy and Ingram, 1971). The magnitude of $^{melt}\Lambda$ can be calculated through an empirical expression using the melt composition as: $^{melt}\Lambda = \Sigma X_n O_n \Lambda_n / \Sigma X_n O_n$, where X, O, and Λ are the mole fraction, number of oxygens in the oxide, and an empirical parameter calculated for the oxide n of interest, respectively (Duffy, 1993). $^{melt}\Lambda$ is a measure of the activity of free oxygen anions in the melt during transfer of electrons from oxygen atoms to cations (Duffy, 1993).

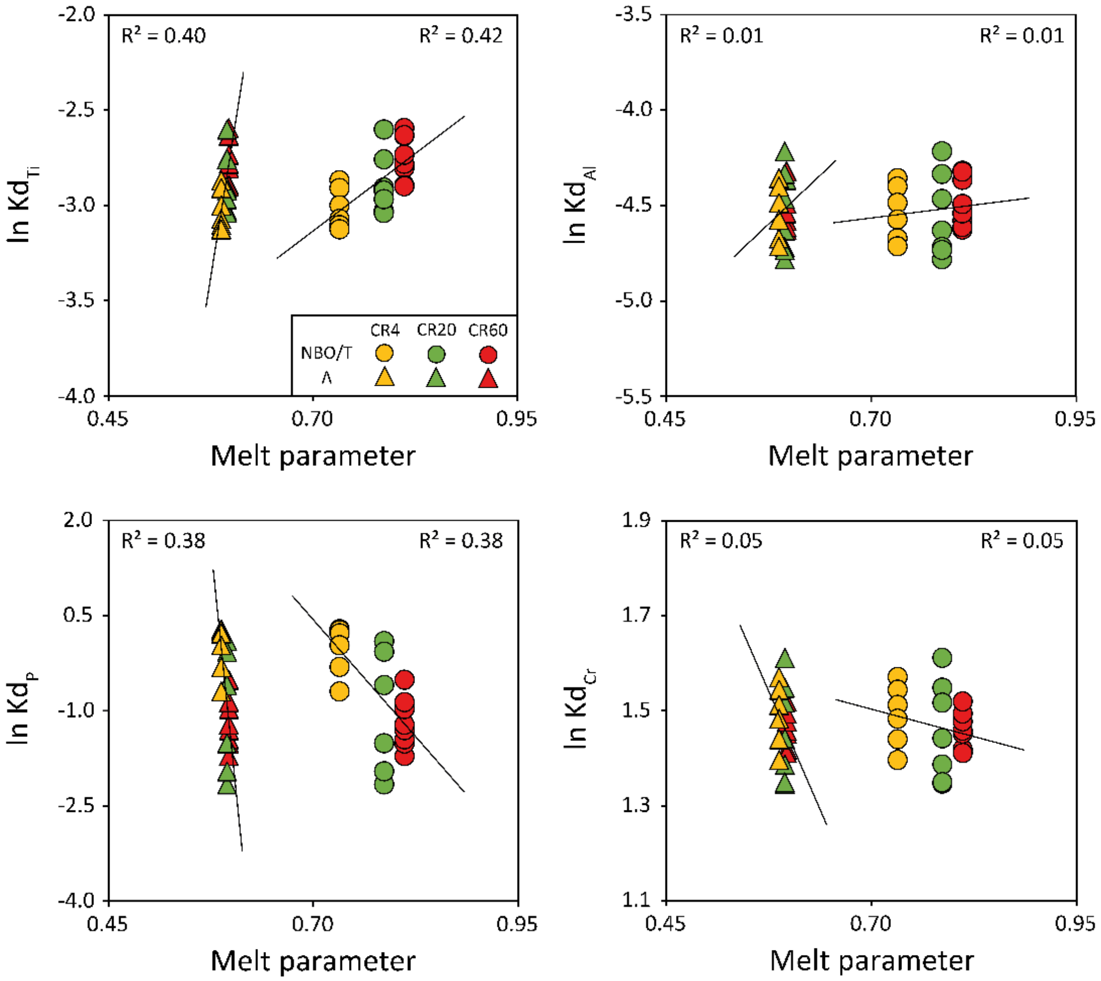

Figure 4.8. *Scatter plots showing the partition coefficient of Ti, Al, P, and Cr vs.* $^{melt}NBO/T$ *(i.e., the number of non-bridging oxygen per tetrahedrally coordinated cations in the melt) and* $^{melt}\Lambda$ *(i.e., the optical basicity of the melt). Regression lines and coefficients of determination* (R^2) *are reported for each melt parameter.*

The logarithm of Kd_{Ti}, Kd_{Al}, Kd_P, and Kd_{Cr} plotted against both $^{melt}NBO/T$ and $^{melt}\Lambda$ shows that the melt structure exercises a very weak control on cation partitioning (Figure 4.8). The value of lnKd_{Ti} weakly increases as the melt structure is less polymerized (R^2 = 0.31-0.33), whereas lnKd_P decreases as a function of CR (R^2 = 0.33-0.33; Figure 4.8). The decreasing trend measured for lnKd_P under kinetic growth conditions can be due to the slow chemical diffusion of P in the melt phase, as this cation is a network-forming species that substitutes for Si in tetrahedral coordination. According to Watson et al. (2015), the diffusivity of P is indeed similar to that of slow-diffusing Si cations in silicate melts ($D_{Si} \approx D_P \approx 4\times10^{-12}$ m^2/s at 1250 °C). There is also no significant change for lnKd_{Al} (R^2 = 0.03-0.04) and lnKd_{Cr} (R^2 = 0.11-0.12) as both $^{melt}NBO/T$ and $^{melt}\Lambda$ increase with increasing CR (Figure 4.8). The lack of melt composition effects on olivine-melt element partitioning is consistent with the knowledge that silicate melt structure becomes dominantly important on the control of Kd only over a broad melt compositional change (e.g., Schmidt, 2006). The dependence of Kd on melt structure is extremely weak for basalts (i.e., $^{melt}NBO/T \geq 0.7$) but it increases remarkably as $^{melt}NBO/T$ is below a threshold value of ~0.6 (Wang and Gaetani, 2008; Di Stefano et al., 2018).

The compositional dependence of Kd on melt components has been also tested by application of the two-lattice model of Nielsen and Drake (1979). The melt is divided in two distinct quasi-lattices: 1) the network-former (NF) quasi lattice (i.e., SiO_2, $NaAlO_2$, $KAlO_2$, TiO_2, and P_2O_5) and 2) the network modifier (NM) quasi lattice (i.e., MgO, FeO, CaO, Al_2O_3, MnO, and Cr_2O_3). The activities of melt components are calculated assuming ideal mixing within their own quasi lattice but no mixing between the two distinct quasi lattices (i.e., $a_i^{NF} = X_i^{NF}/\sum NF$ and $a_j^{NM} = X_j^{NM}/NM$, where i and j stand for network-former and network-modifier cations, respectively; Nielsen and Drake, 1979). Through this approach, the mixing properties of silicate melts are modeled in a quasi-empirical form to obviate extrapolation of more complex thermodynamic properties and the multicomponent variation in the enthalpy and entropy of mixing (Nielsen and Dungan, 1983). The statistically entropy of mixing is approximated by assuming that NF and NM cations mix independently, whereas all oxygens are energetically equivalent (Nielsen and Drake, 1979). This simple oxide-ideal mixing melt model can be used to adequately predict melt component activities over restricted variations of melt composition, such as the case of experiments from this study. Results from calculations are displayed in Figure 4.9, in which the logarithm of Kd_{Ti}, Kd_{Al}, Kd_P, and Kd_{Cr} is plotted against a_{Ti}, a_{Al}, a_P, and a_{Cr}, respectively. The partition coefficient appears poorly correlated with the activities of oxide melt components (R^2 = 0.04-0.32), in analogy with the weak dependence of *Kd* on both $^{melt}NBO/T$ and $^{melt}\Lambda$ (Figure 4.8).

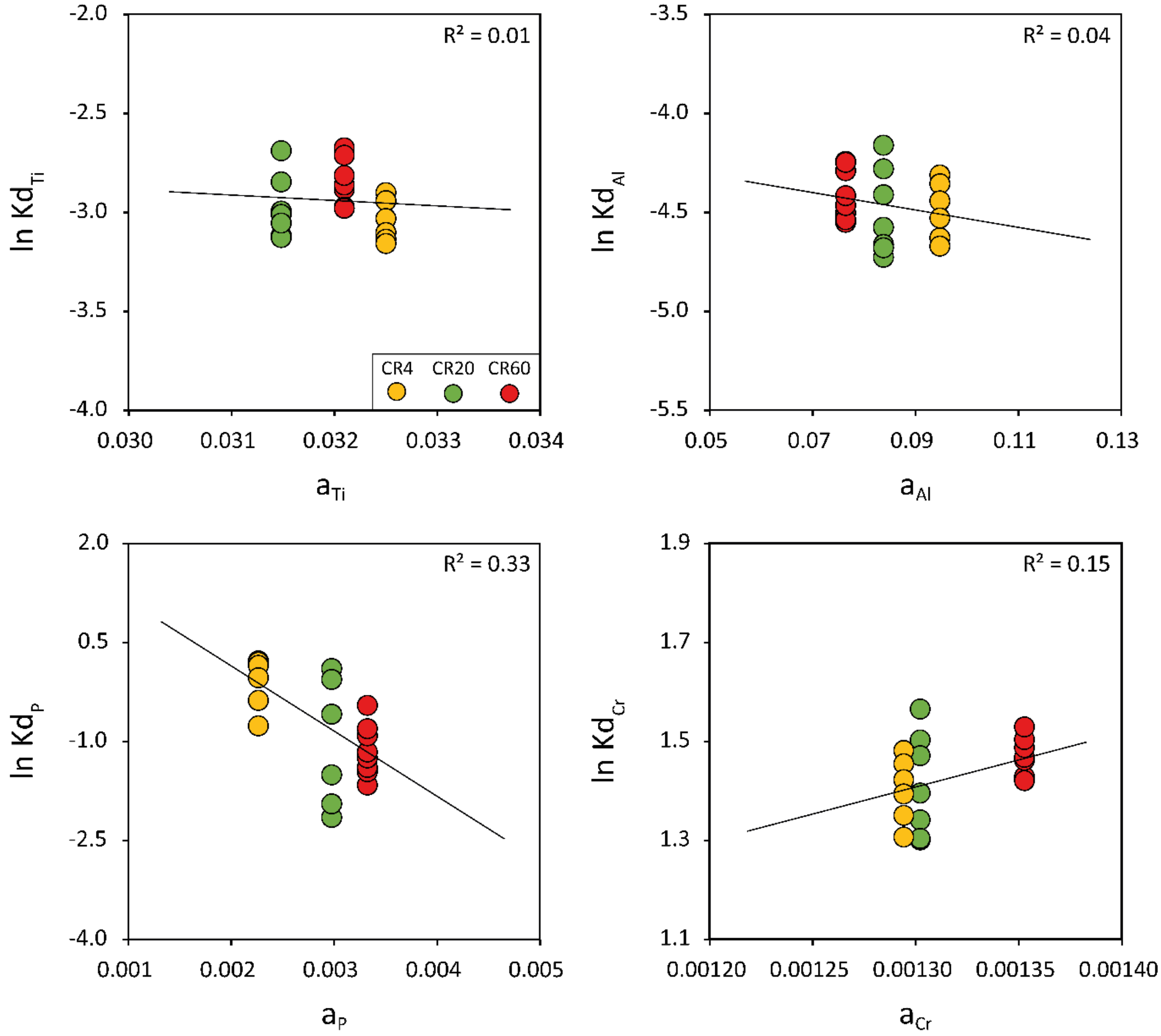

Figure 4.9. *Scatter plots showing the partition coefficient of Ti, Al, P, and Cr vs. the activity of the cations in the melt. Regression lines and coefficients of determination (R^2) are reported for each activity coefficient.*

Since olivine-melt partition coefficients depend on activity-composition relationships in both crystal and melt (e.g., Snyder and Carmichael, 1992), it is not straightforward to disentangle completely the effects of crystal chemistry and melt composition. To provide better constraints on the parameters controlling the incorporation of cations into the olivine structure, the influence of each single crystal/melt component has been quantified following the same approach reported in Mollo et al. (2020). A multivariate analysis has been carried out with the statistical algorithm of Statgraphics Centurion 18® (Statpoint Technologies, Inc., Warrenton, VA, USA) by comparing each single partition coefficient (i.e., Kd_{Ti}, Kd_{Al}, Kd_{P}, and Kd_{Cr}) with the olivine/melt compositional parameters (i.e., ${}^{ol}X_{Si}$, ${}^{ol}X_{Al}$, ${}^{ol}X_{Mg}$, ${}^{melt}NBO/T$ or ${}^{melt}\Lambda$, ${}^{melt}a_{Ti}$, ${}^{melt}a_{Al}$, ${}^{melt}a_{P}$, and ${}^{melt}a_{Cr}$). The *p-value* was used to test the statistical significance of the estimated correlation factors. A *p-value* < 0.05 indicates statistically significant non-zero correlations at the 95% confidence level, in response to a reliable linear regression analysis. Several *p-values* computed for Kd_{Ti} (i.e., ${}^{ol}X_{Si}$, ${}^{ol}X_{Mg}$, ${}^{melt}a_{Al}$, ${}^{melt}a_{P}$, and ${}^{melt}a_{Cr}$), Kd_{Al} (i.e., ${}^{ol}X_{Si}$, ${}^{ol}X_{Mg}$, ${}^{melt}NBO/T$ or ${}^{melt}\Lambda$, ${}^{melt}a_{Ti}$, ${}^{melt}a_{Al}$, ${}^{melt}a_{P}$, and ${}^{melt}a_{Cr}$), Kd_{P} (i.e., ${}^{melt}a_{Ti}$, ${}^{melt}a_{Al}$, and ${}^{melt}a_{Cr}$), and Kd_{Cr} (i.e., ${}^{ol}X_{Si}$, ${}^{ol}X_{Mg}$, ${}^{melt}NBO/T$ or ${}^{melt}\Lambda$, ${}^{melt}a_{Ti}$, ${}^{melt}a_{Al}$, ${}^{melt}a_{P}$, and ${}^{melt}a_{Cr}$) are remarkably high (0.09-0.73), thus indicating no effective correlation between the partition coefficient and olivine/melt parameters. The strength of the relevant linear relationships is calculated through the product moment correlation coefficient *Pearson's r*. This parameter determines the variance of the data set selected for a linear least square fit (e.g., a value of *Pearson's* $r = \pm 1$ corresponds to $\pm 1^2 \times 100 = 100\%$ of correlation) and ranges between −1 (highest negative correlation) and +1 (highest positive correlation). A set of statistically significant *Pearson's r* are derived for Kd_{Ti} (i.e., 0.79 ${}^{ol}X_{Al}$, 0.46 ${}^{melt}NBO/T$ *or* ${}^{melt}\Lambda$, and -0.34 ${}^{melt}a_{Ti}$), Kd_{Al} (i.e., 0.91 ${}^{ol}X_{Al}$), Kd_{P} (i.e., -0.94 ${}^{ol}X_{Si}$, 0.53 ${}^{ol}X_{Al}$, 0.48 ${}^{ol}X_{Mg}$, -0.54 ${}^{melt}NBO/T$ *or* ${}^{melt}\Lambda$, -0.53 ${}^{melt}a_{P}$), and Kd_{Cr} (i.e., 0.87 ${}^{ol}X_{Al}$). The influence (i.e., *I-n* where *n* is the parameter of interest and *I* is expressed in percentage) exerted by each single olivine/melt parameter on the partition coefficient is quantified via the standardized regression coefficient (see Mollo et al., 2020 for further details). Results from these calculations return the following quantities:

1) for Kd_{Ti}: 64% *I*- ${}^{ol}X_{Al}$, 21% *I*- ${}^{melt}NBO/T$ (or -${}^{melt}\Lambda$), 15% *I*- ${}^{melt}a_{Ti}$;
2) for Kd_{Al}: 100% *I*- ${}^{ol}X_{Al}$;
3) for Kd_{P}: 36% *I*- ${}^{ol}X_{Si}$, 17% *I*-${}^{melt}NBO/T$ (or -${}^{melt}\Lambda$), 16% *I*-${}^{melt}a_{P}$, 16% *I*-${}^{ol}X_{Al}$, 15% *I*-${}^{ol}X_{Mg}$;
4) for Kd_{Cr}: 100% *I*- ${}^{ol}X_{Al}$;

It is worth noting that both Kd_{Al} and Kd_{Cr} are entirely controlled by the number of Al cations in the lattice site of olivine, in agreement with the cation exchange $[{}^{M}Mg^{2+}, {}^{T}Si^{4+}] \leftrightarrow [{}^{M}Cr^{3+}, {}^{T}Al^{3+}]$ of Eqn. (2).

Owing to the kinetically-controlled substitution of Si for Al in tetrahedral coordination, the incorporation of Ti in olivine is also apparently correlated with ${}^{ol}X_{Al}$. As a consequence, ${}^{ol}X_{Al}$ can be assumed as a proxy for the increasing magnitude of Kd_{Ti} under *CR* conditions. There is also influence of the melt compositional change on Kd_{Ti} due to the combined effect of $^{melt}NBO/T$ and a_{Ti} (i.e., $I\text{-}^{melt}NBO/T + I\text{-}a_{Ti} = 36\%$). This dependence can be ascribed to the exchange $[^{T}Si^{4+}] \leftrightarrow [^{T}Ti^{4+}]$ that typically occurs in the structure of oxidized silicate melts. Differently from the substitution of Si for Al in tetrahedral coordination of the melt phase, Ti does not need to be associated with a charge compensating cation. Moreover, Ti-poor melts such as basalts are dominated with 4-fold coordinated Ti cations (Yarker et al., 1986; Cormier et al., 2001; Henderson et al., 2002).

As expected from the crystallochemical Eqn. (3), the value of Kd_P is primarily controlled by olivine-related parameters (i.e., $I\text{-}^{ol}X_{Si} + I\text{-}^{ol}X_{Al} + I\text{-}^{ol}X_{Mg} = 67\%$) and only secondary by melt-related parameters (i.e., $I\text{-}^{melt}NBO/T$ *or* $\text{-}^{melt}\Lambda + I\text{-}^{melt}a_P = 33\%$). According to Shea et al. (2015), the lack of a clear P-rich diffusive boundary layer in the melt (Figure 4.6) is counterbalanced by a Kd_P that is strongly growth rate- and time-dependent. The authors have modeled P zonation in olivine dendritic branches by employing Kd_P, D_P, and crystal growth rate parameters all decreasing with time, as expected when the temperature of a cooling system progressively decreases, and the interface melt attempts to relax towards equilibrium concentrations. Our statistical data confirm that P enrichment in olivine is poorly sensitive to the sluggish diffusion kinetics in the surrounding melt. Rather, the change of Kd_P is mostly sensitive to a crystallochemical control resulting from olivine zonation as a function of crystal growth rate. Because both the growth rate of olivine and the diffusivity of P in the melt are expected to decrease with time (Shea et al., 2015), it is plausible that the kinetic incorporation of minor cations in the lattice site proceeds by the attainment of a local thermodynamic equilibrium at the crystal-melt interface (cf. Mollo et al., 2013). The constant equilibrium range of $Kd_{(Fe-Mg)}$ measured for skeletal/dendritic olivine crystals (Table 4.1) testifies to major cation partitioning at equilibrium proportions, although the Fo content in olivine abruptly decreases at $CR \geq 20$ °C/h (Figure 4.1c). Sossi and O'Neill (2016) have also observed that, for a constant *CR*, the Fe-Mg exchange is dictated by a steady state condition where the crystal growth rate and cation diffusivities in the melt are all constant or nearly constant. Owing to the strong crystallochemical control of olivine on the partitioning of Ti, Al, P, and Cr, a steady-state diffusive boundary layer would explain why the kinetic uptake of minor cations in the lattice site of rapidly growing crystals (i.e., disequilibrium cation partitioning) follows the same charge-balance mechanisms documented under equilibrium crystallization.

5. Conclusions

We have performed cooling rate experiments on a Hawaiian tholeiitic basalt to quantify the partitioning of Ti, Al, P, and Cr (*Kd*) between olivine and melt under the effect of crystal growth kinetics. Results from this study bring to the following conclusions:

1) both the crystal size and morphology of olivine are controlled by the cooling rate;

2) the disequilibrium uptake of Ti, Al, P, and Cr cations in skeletal/dendritic olivine crystals highlights complex zoning patterns that are characterized by the enrichment sequence P > Ti > Al > Cr;

3) strong chemical gradients are observed in the melt next to the advancing olivine surface. The diffusive boundary layer is depleted in TiO_2 and enriched in SiO_2 and Al_2O_3. No clear chemical gradients are observed for P_2O_5 and Cr_2O_3 over a maximum diffusive length scale of 120 µm;

4) Kd_{Ti}, Kd_{Al}, and Kd_{P} linearly decrease with increasing Si in olivine, whereas Kd_{Cr} increases with increasing Al. In order to maintain charge balance, the incorporation of minor cations is controlled by the same homovalent and heterovalent substitution reactions observed under equilibrium crystallization conditions. This observation is also consistent with equilibrium $Kd_{(Fe-Mg)}$ values measured for all *CR* experiments and the achievement of a local interface equilibrium due to a steady-state diffusive mass transport in high-temperature, low-viscosity basaltic melts;

5) the magnitude of Ti, Al, P, and Cr partitioning is mostly governed by crystallochemical changes related to the structural rearrangements of cations in the lattice site of olivine. The leverage of crystallographic effects over the melt composition and structure is illustrated by a multivariate statistical analysis showing that Kd_{Al} and Kd_{Cr} are independent of melt parameters, whereas only a weak influence of the melt is measured for Kd_{Ti} and Kd_{P}.

Acknowledgements

We are very grateful to Thomas Shea for sharing the same starting material used in his previous interesting works. We thank Giacomo Pozzi for his great help with microprobe analysis and image acquisitions. Thanks go also to Flavio Di Stefano for sharing his expertise in experimental activities. This research was partially supported by CNRS-INSU program PNP 2796.

Supplementary Materials

Supplementary Material 1: (table) can be found online at:

https://drive.google.com/drive/folders/1Chy-CFrtAWJdUb6rS1gDXqYoja1Lm60I?usp=sharing

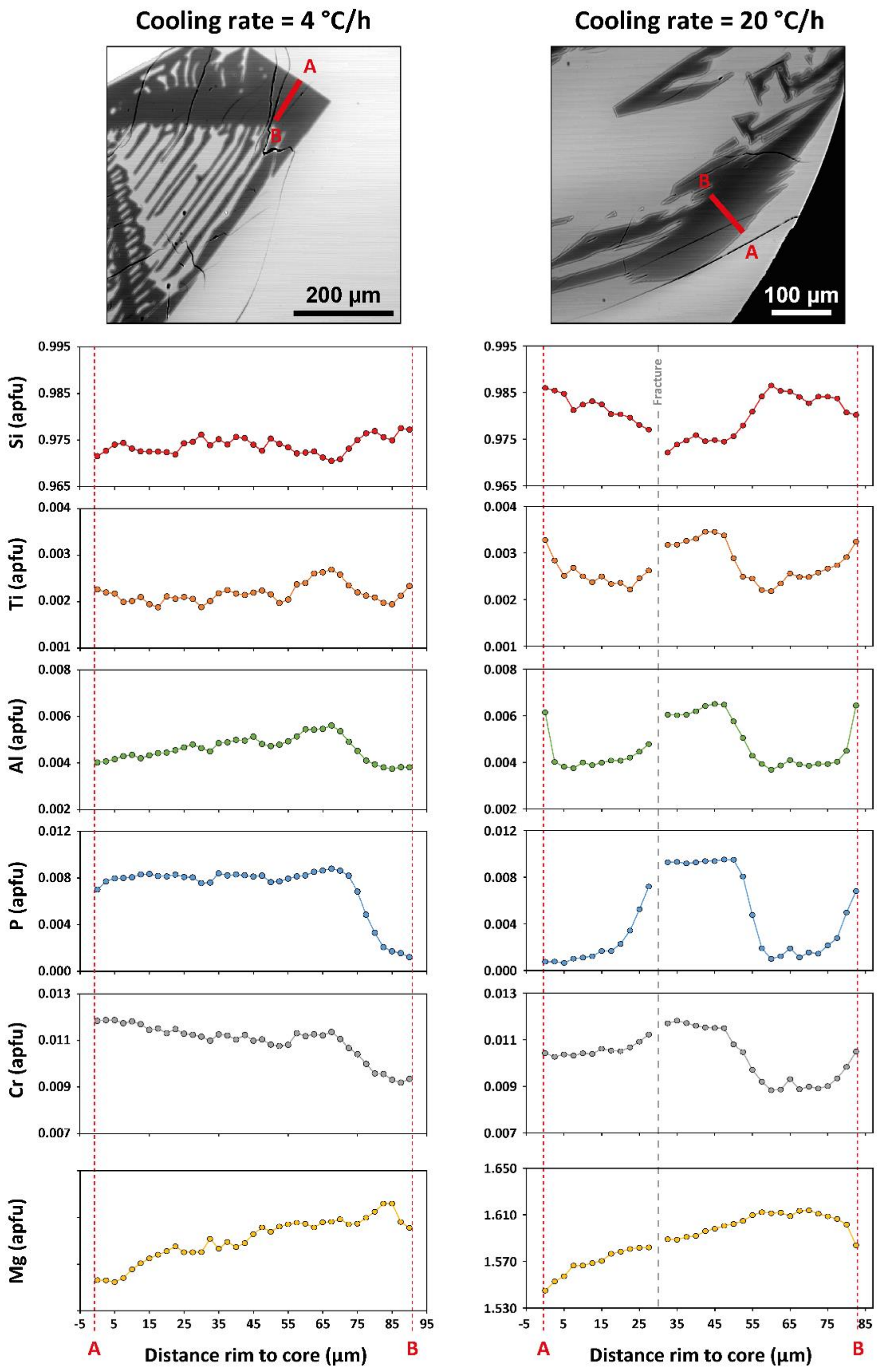

Supplementary Material 2. *BSE (back-scattered electron) photomicrographs of olivine crystals obtained at cooling rates of 4 and 20 °C/h. The red line on the image corresponds to the analytical transect in the olivine crystal. EMP (electron micro-probe) analytical profiles performed along the primary branch highlight a non-radial evolution of the cation concentration from rim to core.*

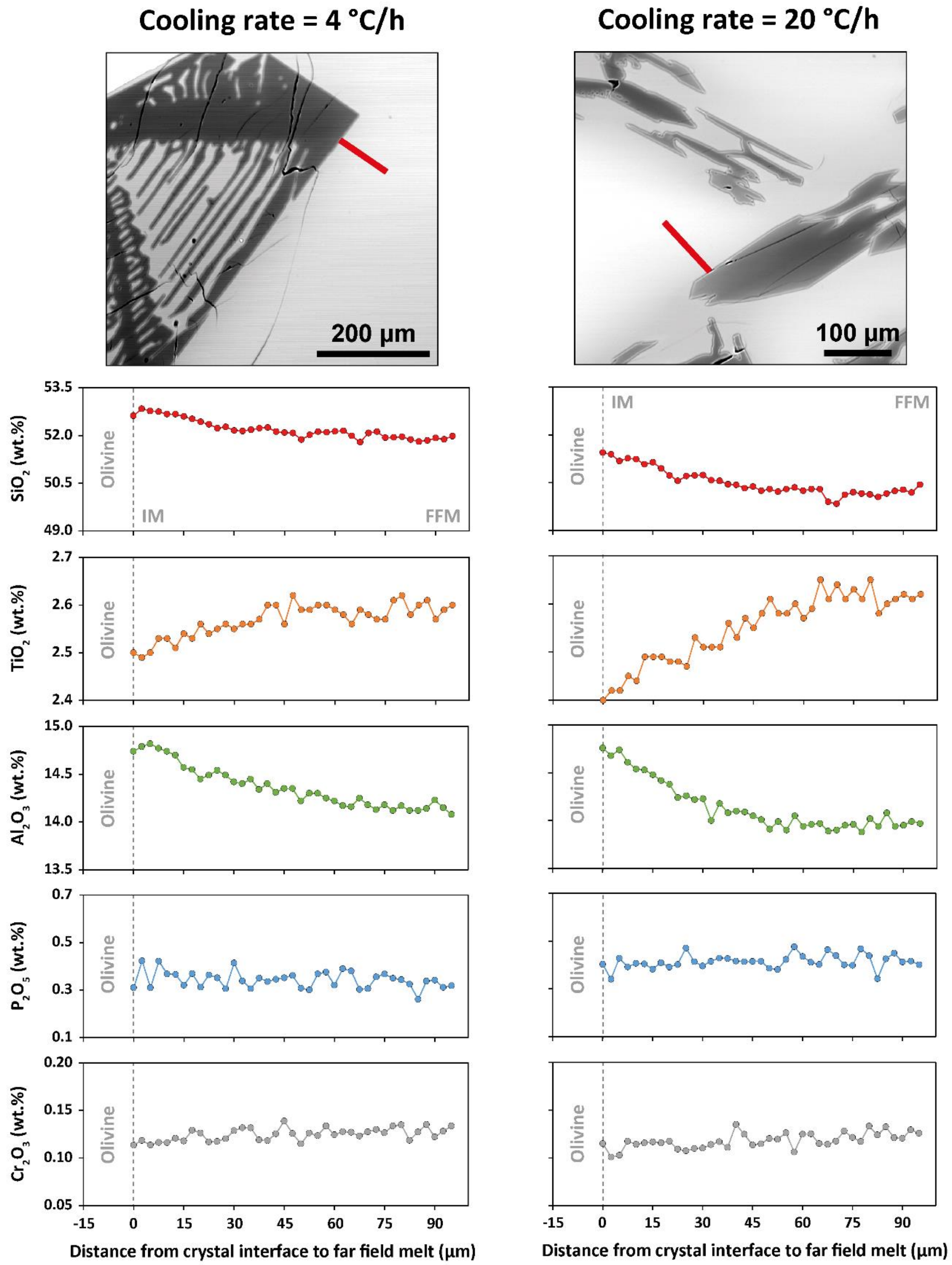

Supplementary Material 3. *BSE (back-scattered electron) photomicrographs of olivine crystals obtained at cooling rates of 4 and 20 °C/h. The red line on the image corresponds to the analytical transect in the glass surrounding the crystal. EMP (electron micro-probe) analytical profiles highlight the presence of a diffusive boundary layer, extending from the interface melt (IM) to the far-field melt (FFM).*

References – Chapter 4

Bédard, J. H. (2005). Partitioning coefficients between olivine and silicate melts. Lithos, 83(3-4), 394-419. doi.org/10.1016/j.lithos.2005.03.011

Bell, A. S., Burger, P. V., Le, L., Shearer, C. K., Papike, J. J., Sutton, S. R., ... & Jones, J. (2014). XANES measurements of Cr valence in olivine and their applications to planetary basalts. American Mineralogist, 99(7), 1404-1412. doi.org/10.2138/am.2014.4646

Berry, A. J., Walker, A. M., Hermann, J., O'Neill, H. S. C., Foran, G. J., & Gale, J. D. (2007). Titanium substitution mechanisms in forsterite. Chemical Geology, 242(1-2), 176-186. doi.org/10.1016/j.chemgeo.2007.03.010

Bershov, L. V., Gaite, J. M., Hafner, S. S., & Rager, H. (1983). Electron paramagnetic resonance and ENDOR studies of Cr3+-Al3+ pairs in forsterite. Physics and Chemistry of Minerals, 9(3), 95-101. doi.org/10.1007/BF00308364

Burns, R. G. (1976). Crystal field effects in chromium and its partitioning in the mantle. In Chromium: its Physicochemical Behaviour and Petrologic Significance (pp. 857-864). Pergamon. doi.org/10.1016/B978-0-08-019954-2.50010-X

Coogan, L. A., Saunders, A. D., & Wilson, R. N. (2014). Aluminum-in-olivine thermometry of primitive basalts: Evidence of an anomalously hot mantle source for large igneous provinces. Chemical Geology, 368, 1-10. doi.org/10.1016/j.chemgeo.2014.01.004

Cormier, L., Calas, G., Neuville, D. R., & Bellissent, R. (2001). A high temperature neutron diffraction study of a titanosilicate glass. Journal of non-crystalline solids, 293, 510-516. doi.org/10.1016/S0022-3093(01)00764-5

De Hoog, J. C., Gall, L., & Cornell, D. H. (2010). Trace-element geochemistry of mantle olivine and application to mantle petrogenesis and geothermobarometry. Chemical Geology, 270(1-4), 196-215. doi.org/10.1016/j.chemgeo.2009.11.017

Di Stefano, F., Mollo, S., Scarlato, P., Nazzari, M., Bachmann, O., & Caruso, M. (2018). Olivine compositional changes in primitive magmatic skarn environments: A reassessment of divalent cation partitioning models to quantify the effect of carbonate assimilation. Lithos, 316, 104-121. doi.org/10.1016/j.lithos.2018.07.008

Di Stefano, F., Mollo, S., Blundy, J., Scarlato, P., Nazzari, M., & Bachmann, O. (2019). The effect of CaO on the partitioning behaviour of REE, Y and Sc between olivine and melt: Implications for basalt-carbonate interaction processes. Lithos, 326, 327-340. doi.org/10.1016/j.lithos.2018.12.019

Donaldson, C. H. (1976). An experimental investigation of olivine morphology. Contrib Mineral Petrol 57:187–213. doi. org/10.1007/bf004 05225

Duffy, J. A., & Ingram, M. D. (1971). Establishment of an optical scale for Lewis basicity in inorganic oxyacids, molten salts, and glasses. Journal of the American Chemical Society, 93(24), 6448-6454. doi.org/10.1021/ja00753a019

Duffy, J. A. (1993). A review of optical basicity and its applications to oxidic systems. Geochimica et Cosmochimica Acta, 57(16), 3961-3970. doi.org/10.1016/0016-7037(93)90346-X

Evans, T. M., O'Neill, H. S. C., & Tuff, J. (2008). The influence of melt composition on the partitioning of REEs, Y, Sc, Zr and Al between forsterite and melt in the system CMAS. Geochimica et Cosmochimica Acta, 72(23), 5708-5721. doi.org/10.1016/j.gca.2008.09.017

Falloon, T. J., Danyushevsky, L. V., Ariskin, A., Green, D. H., & Ford, C. E. (2007). The application of olivine geothermometry to infer crystallization temperatures of parental liquids: Implications for the temperature of MORB magmas. Chemical Geology, 241(3-4), 207-233. doi.org/10.1016/j.chemgeo.2007.01.015

Faure F, Trolliard G, Nicollet C, Montel J-M (2003) A developmen- tal model of olivine morphology as a function of the cooling rate and the degree of undercooling. Contrib Mineral Petrol 145:251. doi.org/10.1007/s0041 0-003-0449-y

Faure, F., Schiano, P., Trolliard, G., Nicollet, C., & Soulestin, B. (2007). Textural evolution of polyhedral olivine experiencing rapid cooling rates. Contrib Miner Petrol 153:405. doi.org/10.1007/ s0041 0-006-0154-8

First, E. C., Leonhardi, T. C., & Hammer, J. E. (2020). Effects of superheating magnitude on olivine growth. Contributions to Mineralogy and Petrology, 175(2), 1-14. doi.org/10.1007/s00410-019-1638-7.

Gaetani, G. A. (2004). The influence of melt structure on trace element partitioning near the peridotite solidus. Contributions to Mineralogy and Petrology, 147(5), 511-527. doi.org/10.1007/s00410-004-0575-1

Garcia, M. O., Pietruszka, A. J., & Rhodes, J. M. (2003). A petrologic perspective of Kīlauea volcano's summit magma reservoir. Journal of Petrology, 44(12), 2313-2339. doi.org/10.1093/petrology/egg079

Giuliani, L., Iezzi, G., Vetere, F., Nazzari, M., Behrens, H., Mollo, S., Cauti, F., Ventura, G., & Scarlato, P. (2020). Evolution of textures, crystal size distributions and growth rates of plagioclase, clinopyroxene and spinel crystallized at variable cooling rates from a mid-ocean ridge basaltic melt. Earth-Science Reviews, 204, 103165, https://doi.org/10.1016/j.earscirev.2020.103165.

Grant, K. J., & Wood, B. J. (2010). Experimental study of the incorporation of Li, Sc, Al and other trace elements into olivine. Geochimica et Cosmochimica Acta, 74(8), 2412-2428. doi.org/10.1016/j.gca.2010.01.015

Hammer, J. E. (2008). Experimental studies of the kinetics and energetics of magma crystallization. Reviews in mineralogy and geochemistry, 69(1), 9-59. doi.org/10.2138/rmg.2008.69.2

Henderson, G. S., Liu, X., & Fleet, M. E. (2002). A Ti L-edge X-ray absorption study of Ti-silicate glasses. Physics and Chemistry of Minerals, 29(1), 32-42. doi.org/10.1007/s002690100208

Hermann, J., O’Neill, H. S. C., & Berry, A. J. (2005). Titanium solubility in olivine in the system TiO 2–MgO–SiO 2: no evidence for an ultra-deep origin of Ti-bearing olivine. Contributions to Mineralogy and Petrology, 148(6), 746-760. doi.org/10.1007/s00410-004-0637-4

Jollands, M. C., Hermann, J., O’Neill, H. S. C., Spandler, C., & Padrón-Navarta, J. A. (2016). Diffusion of Ti and some divalent cations in olivine as a function of temperature, oxygen fugacity, chemical potentials and crystal orientation. Journal of petrology, 57(10), 1983-2010. doi.org/10.1093/petrology/egw067

Jollands, M. C., O'Neill, H. S. C., Van Orman, J., Berry, A. J., Hermann, J., Newville, M., & Lanzirotti, A. (2018). Substitution and diffusion of Cr2+ and Cr3+ in synthetic forsterite and natural olivine at 1200–1500 C and 1 bar. Geochimica et cosmochimica acta, 220, 407-428. doi.org/10.1016/j.gca.2017.09.030

Kennedy, A. K., Lofgren, G. E., & Wasserburg, G. J. (1993). An experimental study of trace element partitioning between olivine, orthopyroxene and melt in chondrules: equilibrium values and kinetic effects. Earth and Planetary Science Letters, 115(1-4), 177-195. doi.org/10.1016/0012-821X(93)90221-T.

Lang, S., Mollo, S., France, L., Nazzari, M., & Misiti, V. (2021). Kinetic partitioning of major-minor cations between olivine and Hawaiian tholeiitic basalt under variable undercooling and cooling rate conditions. Under review.

Lynn, K. J., Garcia, M. O., Shea, T., Costa, F., & Swanson, D. A. (2017). Timescales of mixing and storage for Keanakāko ‘i Tephra magmas (1500–1820 CE), Kīlauea Volcano, Hawai ‘i. Contributions to Mineralogy and Petrology, 172(9), 1-20. doi.org/10.1007/s00410-017-1395-4

Maaløe, S. (2011). Olivine phenocryst growth in Hawaiian tholeiites: Evidence for supercooling. Journal of Petrology, 52(7-8), 1579-1589. doi.org/10.1093/petrology/egr015

Matzen, A. K., Baker, M. B., Beckett, J. R., & Stolper, E. M. (2011). Fe–Mg partitioning between olivine and high-magnesian melts and the nature of Hawaiian parental liquids. Journal of Petrology, 52(7-8), 1243-1263. doi.org/10.1093/petrology/egq089

McKeown, D. A., Buechele, A. C., Tappero, R., McCoy, T. J., & Gardner-Vandy, K. G. (2014). X-ray absorption characterization of Cr in forsterite within the MacAlpine Hills 88136 EL3 chondritic meteorite. American Mineralogist, 99(1), 190-197. doi.org/10.2138/am.2014.4508

Milman-Barris, M. S., Beckett, J. R., Baker, M. B., Hofmann, A. E., Morgan, Z., Crowley, M. R., ... & Stolper, E. (2008). Zoning of phosphorus in igneous olivine. Contributions to Mineralogy and Petrology, 155(6), 739-765. doi.org/10.1007/s00410-007-0268-7

Mollo, S., Lanzafame, G., Masotta, M., Iezzi, G., Ferlito, C., & Scarlato, P. (2011). Cooling history of a dike as revealed by mineral chemistry: a case study from Mt. Etna volcano. Chemical Geology, 288(1-2), 39-52. doi.org/10.1016/j.chemgeo.2011.06.016

Mollo, S., Misiti, V., Scarlato, P., & Soligo, M. (2012). The role of cooling rate in the origin of high temperature phases at the chilled margin of magmatic intrusions. Chemical Geology, 322, 28-46. doi.org/10.1016/j.chemgeo.2012.05.029

Mollo, S., Blundy, J. D., Iezzi, G., Scarlato, P., & Langone, A. (2013). The partitioning of trace elements between clinopyroxene and trachybasaltic melt during rapid cooling and crystal growth. Contributions to Mineralogy and Petrology, 166(6), 1633-1654. doi.org/10.1007/s00410-013-0946-6

Mollo, S., & Hammer, J. E. (2017). Dynamic crystallization in magmas. EMU Notes Mineral, 16, 373-418. doi.org/10.1180/EMU-notes.16.12

Mollo, S., Blundy, J., Scarlato, P., Vetere, F., Holtz, F., Bachmann, O., & Gaeta, M. (2020). A review of the lattice strain and electrostatic effects on trace element partitioning between clinopyroxene and melt: Applications to magmatic systems saturated with Tschermak-rich clinopyroxenes. Earth-Science Reviews, 103351. doi.org/10.1016/j.earscirev.2020.103351.

Mourey, A. J., & Shea, T. (2019). Forming olivine phenocrysts in basalt: a 3D characterization of growth rates in laboratory experiments. Frontiers in Earth Science, 7, 300. doi.org/10.3389/feart.2019.00300

Mysen, B. O. (2004). Element partitioning between minerals and melt, melt composition, and melt structure. Chemical Geology, 213(1-3), 1-16. doi.org/10.1016/j.chemgeo.2004.08.028

Nielsen, R. L., & Drake, M. J. (1979). Pyroxene-melt equilibria. Geochimica et Cosmochimica Acta, 43(8), 1259-1272. doi.org/10.1016/0016-7037(79)90117-0

Nielsen, R. L., & Dungan, M. A. (1983). Low pressure mineral-melt equilibria in natural anhydrous mafic systems. Contributions to Mineralogy and Petrology, 84(4), 310-326. doi.org/10.1007/BF01160284

O'Neill, H. S. C., & Eggins, S. M. (2002). The effect of melt composition on trace element partitioning: an experimental investigation of the activity coefficients of FeO, NiO, CoO, MoO2 and MoO3 in silicate melts. Chemical Geology, 186(1-2), 151-181. doi.org/10.1016/S0009-2541(01)00414-4

Pack, A., & Palme, H. (2003). Partitioning of Ca and Al between forsterite and silicate melt in dynamic systems with implications for the origin of Ca, Al-rich forsterites in primitive meteorites. Meteoritics & Planetary Science, 38(8), 1263-1281. doi.org/10.1111/j.1945-5100.2003.tb00312.x

Papike, J. J., Karner, J. M., & Shearer, C. K. (2005). Comparative planetary mineralogy: Valence state partitioning of Cr, Fe, Ti, and V among crystallographic sites in olivine, pyroxene, and spinel from planetary basalts. American Mineralogist, 90(2-3), 277-290. doi.org/10.2138/am.2005.1779

Pinilla, C., Davis, S. A., Scott, T. B., Allan, N. L., & Blundy, J. D. (2012). Interfacial storage of noble gases and other trace elements in magmatic systems. Earth and Planetary Science Letters, 319, 287-294. doi.org/10.1016/j.epsl.2011.12.018.

Purton, J. A., Allan, N. L., & Blundy, J. D. (1997). Calculated solution energies of heterovalent cations in forsterite and diopside: implications for trace element partitioning. Geochimica et Cosmochimica Acta, 61(18), 3927-3936. doi.org/10.1016/S0016-7037(97)00198-1.

Putirka, K. (2017). Geothermometry and geobarometry. Encyclopedia of geochemistry: a comprehensive reference source on the chemistry of the Earth. Springer International Publishing, Cham, 1-19.

Putirka, K. (2016). Rates and styles of planetary cooling on Earth, Moon, Mars, and Vesta, using new models for oxygen fugacity, ferric-ferrous ratios, olivine-liquid Fe-Mg exchange, and mantle potential temperature. American Mineralogist, 101(4), 819-840. doi.org/10.2138/am-2016-5402

Roeder, P. L., & Emslie, R. (1970). Olivine-liquid equilibrium. Contributions to mineralogy and petrology, 29(4), 275-289. doi.org/10.1007/BF00371276

Sakyi, P. A., Tanaka, R., Kobayashi, K., & Nakamura, E. (2012). Inherited Pb isotopic records in olivine antecryst-hosted melt inclusions from Hawaiian lavas. Geochimica et Cosmochimica Acta, 95, 169-195, doi.org/10.1016/j.gca.2012.07.025.

Schmidt, M. W., Connolly, J. A. D., Günther, D., & Bogaerts, M. (2006). Element partitioning: the role of melt structure and composition. Science, 312(5780), 1646-1650. doi.org/10.1126/science.1126690

Shea, T., Hammer, J. E., Hellebrand, E., Mourey, A. J., Costa, F., First, E. C., ... & Melnik, O. (2019). Phosphorus and aluminum zoning in olivine: contrasting behaviour of two nominally incompatible trace elements. Contributions to Mineralogy and Petrology, 174(10), 1-24. doi.org/10.1007/s00410-019-1618-y

Shea, T., Lynn, K. J., & Garcia, M. O. (2015). Cracking the olivine zoning code: Distinguishing between crystal growth and diffusion. Geology, 43(10), 935-938. doi.org/10.1130/G37082.1

Snyder, D. A., & Carmichael, I. S. (1992). Olivine-liquid equilibria and the chemical activities of FeO, NiO, Fe2O3, and MgO in natural basic melts. Geochimica et Cosmochimica Acta, 56(1), 303-318. doi.org/10.1016/0016-7037(92)90135-6

Sossi, P. A., & O'Neill, H. S. C. (2016). Liquidus temperatures of komatiites and the effect of cooling rate on element partitioning between olivine and komatiitic melt. Contributions to Mineralogy and Petrology, 171(5), 49. doi.org/10.1007/s00410-016-1260-x

Sun, C., & Liang, Y. (2013). The importance of crystal chemistry on REE partitioning between mantle minerals (garnet, clinopyroxene, orthopyroxene, and olivine) and basaltic melts. Chemical Geology, 358, 23-36. doi.org/10.1016/j.chemgeo.2013.08.045

Sutton, S. R., Jones, K. W., Gordon, B., Rivers, M. L., Bajt, S., & Smith, J. V. (1993). Reduced chromium in olivine grains from lunar basalt 15555: X-ray absorption near edge structure (XANES). Geochimica et Cosmochimica Acta, 57(2), 461-468. doi.org/10.1016/0016-7037(93)90444-2

Taura, H., Yurimoto, H., Kurita, K., & Sueno, S. (1998). Pressure dependence on partition coefficients for trace elements between olivine and the coexisting melts. Physics and Chemistry of Minerals, 25(7), 469-484. doi.org/10.1007/s002690050138

Ujike, O. (1982). Microprobe mineralogy of plagioclase, clinopyroxene and amphibole as records of cooling rate in the Shirotori—Hiketa dike swarm, northeastern Shikoku, Japan. Lithos, 15(4), 281-293. doi.org/10.1016/0024-4937(82)90019-6

Vetere, F., Iezzi, G., Behrens, H., Holtz, F., Ventura, G., Misiti, V., Cavallo, A., Mollo, S., & Marcel, D. (2015). Glass forming ability and crystallisation behaviour of sub-alkaline silicate melts. Earth-science reviews, 150, 25-44. doi.org/10.1016/j.earscirev.2015.07.001.

Wallace, P. J., Plank, T., Bodnar, R. J., Gaetani, G. A., & Shea, T. (2021). Olivine-hosted melt inclusions: a microscopic perspective on a complex magmatic world. Annual Review of Earth and Planetary Sciences, 49. doi.org/10.1146/annurev-earth-082420-060506.

Wang, Z., & Gaetani, G. A. (2008). Partitioning of Ni between olivine and siliceous eclogite partial melt: experimental constraints on the mantle source of Hawaiian basalts. Contributions to Mineralogy and Petrology, 156(5), 661-678. doi.org/10.1007/s00410-008-0308-y.

Watson, E. B., Cherniak, D. J., & Holycross, M. E. (2015). Diffusion of phosphorus in olivine and molten basalt. American Mineralogist, 100(10), 2053-2065. doi.org/10.2138/am-2015-5416

Welsch, B., Faure, F., Bachèlery, P., & Famin, V. (2009). Microcrysts record transient convection at Piton de la Fournaise volcano (La Réunion hotspot). Journal of Petrology, 50(12), 2287-2305. doi.org/10.1093/petrology/egp076

Welsch, B., Faure, F., Famin, V., Baronnet, A., & Bachèlery, P. (2013). Dendritic crystallization: A single process for all the textures of olivine in basalts?. Journal of Petrology, 54(3), 539-574. doi.org/10.1093/petrology/egs077

Welsch, B., Hammer, J., & Hellebrand, E. (2014). Phosphorus zoning reveals dendritic architecture of olivine. Geology, 42(10), 867-870. doi.org/10.1130/G3569 1.1

Yarker, C. A., Johnson, P. A., Wright, A. C., Wong, J., Greegor, R. B., Lytle, F. W., & Sinclair, R. N. (1986). Neutron diffraction and EXAFS evidence for TiO5 units in vitreous K2O· TiO2· 2SiO2. Journal of non-crystalline solids, 79(1-2), 117-136. doi.org/10.1016/0022-3093(86)90041-4

Zhukova, I., O’Neill, H., & Campbell, I. H. (2017). A subsidiary fast-diffusing substitution mechanism of Al in forsterite investigated using diffusion experiments under controlled thermodynamic conditions. Contributions to Mineralogy and Petrology, 172(7), 1-12. doi.org/10.1007/s00410-017-1365-x

Third Part

General conclusions & Perspectives

General Conclusions & Perspectives

Partitioning of element correspond to the distribution of element of interest between two constituent phases as a function of different thermodynamic and charge balance mechanisms. Major elements generally affect the chemical equilibrium of a system. On the other hand, trace elements do not influence the bulk reactions occurring in the system. But because of their sensitivity to thermodynamic conditions, they can be considered as passive tracers of chemical reactions. For this reason, the partitioning of major and trace elements between both olivine and melt phases is greatly studied by petrologists investigating terrestrial rocks. It is now well known that solidification processes are controlled by the cooling kinetics and that the mechanisms ruling the crystal growth directly impact the partitioning of elements. Therefore, knowing how the elements partition between two phases, may give important clues on the crystallization conditions.

In this thesis I explored (i) the partitioning of major, minor and trace elements between olivine and basaltic melt under disequilibrium crystallization conditions encountered by magmas in naturally solidifying settings, and (ii) the charge balance mechanisms and cation substitution reactions controlling the incorporation of these cations in the lattice site of rapidly growing olivine crystals. I conducted 1-atm experiments on natural basaltic composition (Hawaiian tholeiite) under different degrees of undercooling ($-\Delta T = 35$ an 85 °C) and cooling rates (CR = 4, 20, and 60 °C/h), in a relatively reduced environment (QFM-2), to avoid the crystallization of any other phases (oxides) than olivine in the charge. BSE photomicrographs collected from my samples exhibit strong morphological differences, showing equilibrium and disequilibrium olivine crystallization at low and high undercooling, respectively. These observations were verified by the determination of Fe-Mg exchange between olivine and melt (chapter 3), showing a constant equilibrium of the system at low undercooling, and a disequilibrium of the bulk system at high undercooling. However, at high $-\Delta T$, I observe two distinct equilibration stages between olivine core and FFM, and olivine rim with IM. Although a diffusive boundary layer develops in the melt surrounding olivine during its growth, Mg, Fe, Mn, and Ca (cations entering in the olivine octahedral site) are incorporated into the lattice site at near-equilibrium proportions because of the local equilibrium occurring at the olivine/melt interface. The quantitative analysis performed on my samples also allowed me to spot olivine zonation characterized by an increase of P, Ti, Al, and Cr as Si decreases, following the enrichment sequence P > Ti > Al > Cr (chapter 4). This observation suggests an incorporation of this minor/trace elements in the olivine tetrahedral site by substituting Si cations. A homovalent substitution [$^{T}Si^{4+}$] ↔ [$^{T}Ti^{4+}$] controls the incorporation of Ti, whereas [$^{M}Mg^{2+}$, $^{T}Si^{4+}$] ↔ [$^{M}Al^{3+}$, $^{T}Al^{3+}$], and [2 $^{T}Si^{4+}$] ↔ [$^{T}P^{5+}$, $^{T}Al^{3+}$] substitutions control the incorporation of Al and P. The incorporation of Cr in the octahedral site is consistent with the coupled substitution [$^{M}Mg^{2+}$, $^{T}Si^{4+}$] ↔ [$^{M}Cr^{3+}$, $^{T}Al^{3+}$]. Importantly, to maintain charge balance, the disequilibrium incorporation of minor cations into the olivine lattice is governed by the same substitution mechanisms that occur under equilibrium crystallization, which is consistent with the achievement of interface local equilibrium.

Results from my thesis open new perspectives for the investigation of trace elements under variable crystal growth rate conditions and the development of thermodynamic and geospeedometric models based on mineral compositional changes and cation exchanges at the crystal-melt interface.